# The effect of nourishments on dune erosion during a storm sequence

## Modelling dune erosion with XBeach at Egmond aan Zee

**J.B. van der Waal**

Utrecht University

Rijkswaterstaat
*Ministry of Infrastructure and Water Management*

Deltares

Cover photo: (Boskalis/Flying Focus)

# The effect of nourishments on dune erosion during a storm sequence

## Modelling dune erosion with XBeach at Egmond aan Zee

by

**Bart van der Waal**

in partial fulfilment of the requirements for the degree of

**Master of Science**
in Earth Sciences

Faculty of Geosciences
Department of Physical Geography
Utrecht University
9 February 2024

Supervisor: Dr. Timothy Price, Utrecht University
Second assessor: Dr. Ir. Bart Grasmeijer, Deltares

# Abstract

The Dutch coast is one of the most heavily nourished coasts in the world, with an average of 12 mln. $m^3$ of sand being added to the coast annually. This strategic coastline maintenance is necessary to ensure flood safety for the hinterland, by maintaining the nearly uninterrupted sandy beaches and, in particular, wind-blown dunes. Still, the effect of localized nourishment on beach-dune development and dune erosion during storms remains unclear. Besides feeding the coast, nourishment may act as a direct buffer against dune erosion during a storm. Moreover, sequences of storms during a single storm season may lead to different responses of the nourished beach-dune system, compared to a non-nourished stretch of coast.

The objective of this study is to provide insight into the effect of nourishments on dune erosion during a storm sequence, in particular the difference between a nourished and non-nourished stretch of coast (sub-aim 1) and the effect of nourishment designs (sub-aim 2). For this, the numerical model XBeach was used to simulate littoral hydrodynamic and morphodynamic responses during a storm sequence at Egmond aan Zee, the Netherlands. For this study, offshore data measured during a sequence of storms in early 2022 (with storms Corrie, Dudley, Eunice, and Franklin) were used as input for the model. Six measured bathymetries from 2020 - 2023, each spanning 6 km alongshore with a nourished and non-nourished section of the coast, were utilized to investigate the potential persistent effects of nourishments on dune erosion during the storm sequence (sub-aim 1). Additionally, different nourishment designs were added to the most recently acquired bathymetric data of October 2023 to investigate the effects of nourishment design on dune erosion (sub-aim 2). Configurations included the actual design of the 2023-2024 Bergen-Egmond shoreface nourishment, various beach nourishments, and the removal of the outer subtidal bar.

The results showed consistent decreased dune erosion during the storm sequence in the nourished site compared to the non-nourished site from 2020 - 2023, attributed to increased wave dissipation over the shallower and further onshore-positioned subtidal bars in the nourished site. Additionally, infragravity wave heights over the beach during the peaks of the storms were larger at the non-nourished site compared to the nourished site. Spatial variability (alongshore) of dune erosion strongly correlated with beach slope, whereas steeper beaches correlated with more dune erosion. Furthermore, a persistent erosional hotspot in the non-nourished site corresponded to the alongshore location of a deeper area (up to -6m) in the nearshore bathymetry, where short waves propagated further onshore before breaking. The addition of various shoreface nourishment designs resulted in limited impact on dune erosion rates during the storm sequence, suggesting that shoreface nourishment effects on dune erosion develop over timescales longer than that of a single storm season. Conversely, beach nourishment designs had a more direct impact on dune erosion since the entire beach and the height of the dune toe were raised. In conclusion, this study demonstrates that nourishment has a positive effect on coastal protection during a storm sequence. The findings contribute to encouraging nourishment in the context of coastal safety.

# Acknowledgements

This thesis was written as the final work to complete the Master's program in Earth Surface and Water (track: Coastal Dynamics & Fluvial Systems) at Utrecht University, carried out at the Department of Physical Geography in cooperation with Rijkswaterstaat and Deltares.

I would like to express my sincere gratitude to Timothy Price for the opportunity to graduate in the field of storms and dune erosion, guidance, and constructive feedback. I would also like to express my deepest appreciation to Anne de Beer for introducing XBeach and the weekly conversations we had about the model results. Furthermore, I could not have undertaken this journey without Merijn Niemeijer, another fellow student studying storm sequences. Thank you for sharing data, knowledge, and feedback on results. For additional information regarding modelling storm sequences at Egmond aan Zee, I would like to refer to his report. I would like to thank Bart Grasmeijer and Laura Brakenhoff for regular conversations and for finding the right people within the organizations. Finally, I want to thank my family and friends for their support.

*J.B. van der Waal*
*Utrecht, February 2024*

# Contents

# List of Figures

# List of Tables

# Nomenclature

### Abbreviations

| | |
|---|---|
| BKL | Basiskustlijn |
| JARKUS | JAaRlijkse KUStmeting; yearly coastal measurement |
| MKL | Momentane kustlijn |
| MSL | Mean Sea Level |
| NAP | Normaal Amsterdams Peil; is about equal to MSL |

### Symbols

| | |
|---|---|
| $\Delta t$ | Time interval [s] |
| $H_{m0,IG}$ | Spectral significant infragravity wave height [m] |
| $H_{m0,SS}$ | Spectral significant short wave height [m] |
| $H_{m0}$ | Spectral significant wave height [m] |
| $H_{rms}$ | Root mean squared wave height [m] |
| $H_{s,threshold}$ | Threshold wave condition [m] |
| $H_s$ | Significant wave height [m] |
| $S_{utot}$ | Sediment transport integrated over bed load and suspended and for all sediment grains in cross-shore direction [m$^2$/s] |
| $S_{vtot}$ | Sediment transport integrated over bed load and suspended and for all sediment grains in alongshore direction [m$^2$/s] |
| $T_{m02}$ | Spectral significant wave period [s] |
| $T_p$ | Peak period [s] |
| $t_r$ | Recovery time [s] |
| $u$ | Depth-averaged cross-shore velocity [m/s] |
| $v$ | Depth-averaged alongshore velocity [m/s] |
| $z_b$ | Bed level [m] |
| $z_s$ | Water level [m] |

# Chapter 1

# Introduction

## 1.1 Motivation

The Dutch coast is one of the most heavily nourished coasts in the world. For dynamic coastline maintenance, an average of 12 mln. $m^3$ of sand is added annually to the coastline of 432 km long (Brand et al., 2022). This is the result of the misbalance in the sediment budget of the coastal zone caused by sea level rise, soil subsidence, and a decreasing input of sediment from marine sources and rivers (Spek and Lodder, 2015; van der Meulen et al., 2007).

Nourishment efforts likely have to increase in the future due to accelerating sea level rise and storms (Brand et al., 2022; De Winter and Ruessink, 2017). Especially storms that occur in close temporal succession, called storm sequences, present a high risk for natural environments and human activities at the coast (Eichentopf et al., 2019). Unexpectedly significant beach-dune erosion can be generated by a storm within a sequence since the system does not have time to recover from a previous storm (Eichentopf et al., 2019; Sénéchal et al., 2017; Karunarathna et al., 2014). For example, the winter of 2013 and 2014 was a recent period of exceptional storm activity along the North-West Atlantic European coasts resulting in catastrophic erosion and damage that was reported along the European coast (Masselink et al., 2016).

Increasing interest in storm sequences is motivated by the growing awareness of the coastal risk induced by more frequent and/or intense storms as a result of climate change (Jenkins et al., 2023; De Winter and Ruessink, 2017; Feser et al., 2015; Bender et al., 2010). In particular, the Netherlands is considered an area sensitive to storms, because 40% of the country is below Mean Sea Level (MSL), with the lowest region reaching about 7 meters below MSL. In addition, the Netherlands is one of the world's most densely inhabited countries protected from flooding by nearly uninterrupted sandy beaches and, in particular, wind-blown dunes (Ritzema and van Loon-Steensma, 2018; De Winter and Ruessink, 2017).

Although many studies focused on the effects of storm sequences on beach-dune erosion around the world and how these storms within a sequence match with single storms (Eichentopf et al., 2019; Baldock et al., 2021; Sénéchal et al., 2017; Karunarathna et al., 2014; Splinter et al., 2014; Ferreira, 2005), the effect of single storms on beach-dune erosion in the Netherlands (de Winter et al., 2015; van Gent et al., 2008), nourishment behaviour (Brand et al., 2022; Huisman et al., 2019; Grunnet et al., 2004; Pinto et al., 2022), the feeding and wave breaking function of shoreface nourishment (van Geer, 2012; van der Spek et al., 2007; Quartel and Grasmeijer, 2007) and bar response to nourishment (Radermacher et al., 2018; Ruessink et al., 2012; Grunnet and Ruessink, 2005; De Keijzer, 2004) during different conditions and their effect on beach-dune erosion, as well as modelling the effect of nourishment on beach-dune erosion at the Dutch coast (Huisman et al., 2019; van Geer, 2012), the response of a nourished Dutch coast to storm sequences is still unclear.

Better insight into the morphodynamics of a nourished coast and storm sequences will be valuable in coastal monitoring, coastal management, and strategies. Besides feeding the coast, nourishment may act as a direct buffer against dune erosion during a storm. Moreover, sequences of storms during a single storm season may lead to different responses of the nourished beach-dune system, compared to a non-nourished stretch of coast. Furthermore, it is suggested that future research should be performed with storm sequences besides single storms to study dune erosion in different conditions (Eichentopf et al., 2019). For example, is unclear what a storm sequence means for coastal maintenance and safety of the Dutch coast. The design conditions for the dunes along the Dutch coast are currently based on individual extreme storm conditions with a specified return period (Bosboom and Stive, 2021; Vuik and van Balen, 2012), while less extreme storms that occur in close temporal succession might present a bigger risk for coastal safety.

## 1.2 Research objective

As mentioned before, the effect of nourishment on beach-dune development is studied extensively but in relation to single storm events, calling for further research to improve the knowledge of the complex morphodynamics of nourished coastal areas affected by storm sequences. This study aims to make the effect of nourishments on dune erosion during a storm sequence insightful. The numerical model XBeach is used to compute littoral hydrodynamics and morphodynamic response during a storm sequence. Bathymetric data from a partly nourished coast and offshore data of a storm sequence are used to look at the effects of nourishments on dune erosion. In addition, the effect of different nourishment designs on dune erosion during a storm sequence is being investigated.

## 1.3 Structure

This thesis report is built up as follows. Chapter 2 gives background information about coastal hydrodynamics and morphodynamics, dune erosion, storm sequences, beach vulnerability and coastline maintenance. Chapter 3 explains the methodology used. The study approach, study site, study data, XBeach, model input/output/validation and analysis are explained. Chapter 4 contains an overview and discussion of the results of the XBeach validation before running the final XBeach output. Chapter 5 contains an overview of the final results. Morphodynamic and hydrodynamic results are displayed. Chapter 6 the discussion of the results. Key findings, interpretations, limitations and recommendations are included. Chapter 7 gives the conclusion. Additional information can be found in appendices A to H.

# Chapter 2

# Background

This chapter gives background information which is necessary to understand the relevant processes for dune erosion and the interaction of waves with the nearshore morphology. It is however assumed that the reader already has some knowledge about important concepts in coastal processes. Coastal hydrodynamics like short waves and infragravity waves are briefly explained in Section 2.1. Section 2.2 gives an overview of the nearshore morphodynamics like beach states, bar migration, dune erosion and causes of alongshore variability in dune erosion. Section 2.3 explains the definition of the storm sequence, the consequences of a storm sequence, and how a storm sequence relates to a single storm. Finally, the Dutch policy on coastal maintenance and the various nourishment types are described in Section 2.4.

## 2.1 Coastal hydrodynamics

### 2.1.1 Short waves

Short waves are waves generated by wind on deep water and travel towards the shore. They can be actively created by the wind (known as sea waves) or can continue propagating after leaving their initial generation area (known as swell waves). Typical short-wave frequencies are between 0.04 and 1 Hz (Bosboom and Stive, 2021; Bertin et al., 2018). Short incident waves are the primary source of energy input to the beach. In deep water, the waves have a sinusoidal shape. When the waves propagate to the coast and enter shallow water, wave transformation takes place because of interaction with the seabed through processes such as refraction, shoaling, bottom friction and wave-breaking (Bosboom and Stive, 2021; van der Zanden, 2016).

When the water depth becomes less than about half the wavelength, the waves start to be affected by the bottom and slow down. The celerity and wavelength decrease and wave height increases as the total energy flux remains constant. This translates into asymmetry about the horizontal axis, with short-period crests and longer-period troughs (shoaling zone; Figure 2.1). This type of asymmetry is called skewness. As waves propagate further, the surface form increases in asymmetry about the vertical axis. This form, also called wave asymmetry, has a steep front face and a gentle rear face (saw-tooth-shaped). The steepness of the wavefront increases with increasing asymmetry, eventually leading to wave breaking (breaking/surf zone; Figure 2.1). Usually, wave breaking occurs when the wave height is greater than 1/7 of the wavelength or 3/4 of the water depth (Bosboom and Stive, 2021; Schrijvershof et al., 2019; van der Zanden, 2016). Wave breaking can happen in different ways like plunging, spilling, surging and collapsing, depending on wave and bed profile characteristics. The breaking wave develops into a roller which continuously propagates shoreward along the inner surf zone while dissipating energy (inner surf zone; Figure 2.1). When the roller reaches the shore, it runs up on the beach while decelerating due to fraction and gravitational forces. The region of beach run-up/run-down is called the swash zone (swash zone; Figure 2.1)(Bosboom and Stive, 2021; van der Zanden, 2016). In the swash zone, all the big waves have been broken and the water motion is dominated by infragravity waves (Bertin et al., 2018).

The velocities of the wave can be split into time-averaged (net current), orbital and turbulent components. The net currents are generally offshore directed in the lower half of the water column (also termed undertow) because they compensate the onshore mass flux (Stokes drift) above the wave through the level. In the breaker zone, the onshore mass flux in the roller is larger than the mass flux associated with the Stokes drift for non-breaking waves. In addition, wave height reduction results in a horizontal momentum flux gradient that drives towards the beach causing a pressure gradient (set-up/set-down). The increase of mass flux and the positive pressure gradient leads to an increase of the undertow in the breaker zone. The orbital velocities vary in magnitude and direction during the wave cycle. Skewed waves have higher orbital velocities below the crest than below the through. Asymmetric waves exceed the acceleration during the zero-up crossing during the zero-down crossing of the wave. This is also called orbital velocity skewness and asymmetry and it leads to a higher bed shear stress during the crest phase than during the trough phase. Turbulent velocities can be generated by a moving fluid's internal shear or by friction with an external object. Bed friction and rollers are the primary turbulence sources in the wave-breaking zone (Bosboom and Stive, 2021; Schrijvershof et al., 2019; van der Zanden, 2016).

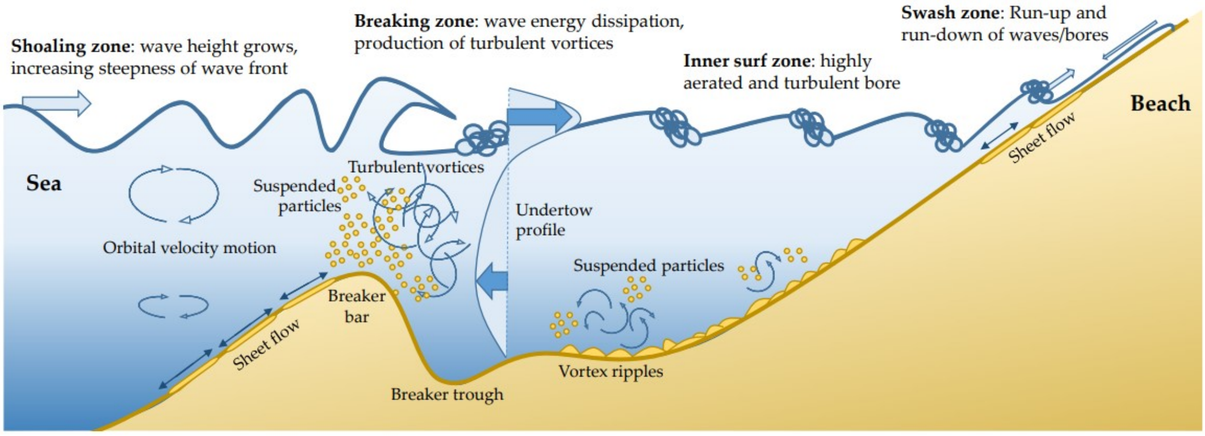

**Figure 2.1:** Conceptual drawing of cross-shore hydrodynamic and sediment processes in the near-shore region (van der Zanden, 2016).

### 2.1.2 Infragravity waves

The concept of wave radiation stresses and wave-induced forces described in the previous section did not include temporal variations created by individual waves or wave groups. An important kind of wave to consider is the infragravity wave since its presence influences nearshore processes (Roelvink et al., 2009). Infragravity waves are indirectly formed by the wind because they receive their energy from the sea and well waves (short waves). Typical infragravity wave frequencies are between 0.004 and 0.04 Hz (Bertin et al., 2018). The formation of infragravity waves can be distinguished by three mechanisms. The first mechanism is that the larger short wave group transports more momentum than the smaller waves, leading to a water level lowering under the larger waves and increasing water level under the smaller waves (Figure 2.2). This induces a variation of the mean water level at a group scale. The variation of the mean water level over the length of a wave group can be seen as a 'bound infragravity wave' and is 180 degrees out of phase (Bosboom and Stive, 2021; Aucan and Ardhuin, 2013). Linear dependency is observed between infragravity and short wave height (Oh et al., 2023). The second mechanism is related to the moving breakpoint of the short wave group when the waves approach the shore. The largest short waves break further offshore than the smaller short waves. This results in a time-variation of the radiation stress in the surf zone. This is balanced by a time-varying wave setup and creates energy at the infragravity frequencies. The created difference in water level is a 'free infragravity wave' (Bertin et al., 2018; Symonds et al., 1982). The third mechanism is the merging of bores (breaking wavefront, resembling a hydraulic jump) inside the surf zone, leading to a nonlinear process that increases the wave period. This process contributes to energy transfer from short wave frequencies to infragravity wave frequencies (Bertin et al., 2018). The mechanisms vary with beach slope. The bound infragravity and bore mechanism is strongest on gently sloping beaches (1:30), and the free infragravity mechanism dominates on steep sloping beaches (1:10) (Bertin et al., 2018; de Bakker et al., 2016).

The infragravity waves propagate as follows. The bound infragravity waves generated offshore grow steadily while moving onshore. In the surf zone, where the short waves are breaking, the bound group structure disappears, and the infragravity waves propagate ashore as free waves (Bertin et al., 2018; Ruessink, 1998). Close to the shore, the infragravity waves dissipate their energy by transferring their energy back to higher frequencies and bottom friction. Infragravity waves are generally reflected at the beach face and travel offshore as leaky waves or edge waves. The offshore movement of free infragravity waves and the interference with incoming infragravity waves can result in a series of nodes and anti-nodes (standing waves) (Bertin et al., 2018). Bar presence may cause infragravity waves to become trapped, refracting from one to the other side of the bar (Bryan et al., 1998).

The importance of reflection versus dissipation varies with the slope of the beach. On gentle slopes, infragravity waves are relatively large compared to short waves causing higher harmonics and steepening of the infragravity waves, leading to breaking and energy losses (Bertin et al., 2018; de Bakker et al., 2016). Conversely, on steep slopes, where infragravity waves are smaller, interaction with the short-wave spectrum peak occurs during energy loss, spreading the energy over a wider frequency range. However, less energy is extracted from the infragravity band compared to gentler slopes. Energy is spread to a large range of higher (short-wave) frequencies, but overall less energy is removed from the infragravity band than on more gentle slopes (Bertin et al., 2018; de Bakker et al., 2016).

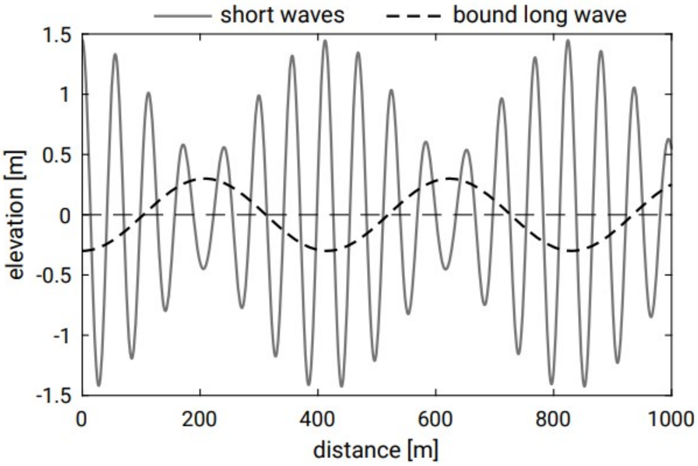

**Figure 2.2:** A bound long wave (infragravity wave), perfectly out of phase with the short wave group (Bosboom and Stive, 2021).

## 2.2 Nearshore morphodynamics

### 2.2.1 Beach states

In this study, the focus is on the nearshore zone consisting of the surf zone, the beach and the first dune row. Wave energy dissipation is dominant in the nearshore zone and the profile is therefore highly dynamic (Bosboom and Stive, 2021; Schrijvershof et al., 2019).

Parts of the nearshore zone are the beach and the intertidal zone. In the intertidal zone, strong three-dimensional morphology is observed like ridge-runnel structures. The impact of this three-dimensional morphology on nearshore zone behaviour is limited (Bosboom and Stive, 2021). Surf zone morphological structures have a larger impact on nearshore zone behaviour. One, two or sometimes more bars (subtidal bars) are present while in the intertidal zone, a bar may also be present (intertidal bars). The bars are important as they determine the locations of energy dissipation due to wave breaking and thus dictate the morphological response (Bosboom and Stive, 2021; Castelle et al., 2015).

The nearshore zone profile and plan form varies around the world. Wright and Short distinguish six various morphodynamic regimes, also called beach states, ranked from the highest state, dissipative, to the lowest state, reflective. A reflective beach has a steep and narrow coastal zone with a berm and a narrow surf zone without bars. Collapsing or surging breakers are common on reflective beaches. The corresponding waves have low steepness. Dissipative beaches, at the other end of the beach states, have a wide and flat coastal zone with one or multiple layer bars with dunes backing a wide beach. A dissipative beach is the result of high-energy waves breaking far offshore. The four intermediate beach states are strongly three-dimensional. Rip currents and channels play an important role in intermediate beach morphologies. Beaches can move through the series of beach states, depending on wave conditions and grain size of the beaches (Castelle and Masselink, 2023; Bosboom and Stive, 2021; Wright and Short, 1984).

### 2.2.2 Bar migration

Along the Dutch coast, there is a sequence of several bars and troughs in the cross-direction (Brand et al., 2022). The bars show a cyclic behaviour. Bars generally and on average move offshore under more energetic conditions and onshore during less energetic conditions and skewed waves. At timescales from months to decades, sandbars are found to exhibit a net offshore migration (NOM) (Bosboom and Stive, 2021; Radermacher et al., 2018). The bars form in the intertidal zone, after which the bars move offshore and grow in size until a maximum around the initiation of the surf zone, after which the bars gradually decrease in size and amplitude and finally disappear at the end of the active shoreface profile (Bosboom and Stive, 2021; Radermacher et al., 2018). The cycle varies between 4 to 5 years on the South Holland coast and around 15 years on the North Holland coast. This difference depends on the shoreface slope and bar sizes. The bars have a positive effect on wave breaking which leads to differences in shoreline response (Bosboom and Stive, 2021; Castelle et al., 2015). The bar cycle can be interrupted by nourishments (Figure 2.11). The nearshore zone cross-shore profile responds differently to seasonal conditions, leading to a seasonal behaviour and profile. During the milder summer wave conditions, the winter offshore bars migrate onshore. Hence, in summer the beach has a high profile. In addition, a relatively calm period can be interrupted by a storm event causing the summer-winter behaviour (Bosboom and Stive, 2021; Radermacher et al., 2018). Energetic wave conditions tend the submerged bars to be straight and align the bars more parallel to the coastline. Less energetic wave conditions can break up bars close to the shore into smaller bars with crescentic shapes Almar et al. (2010).

### 2.2.3 Dune erosion

Dune erosion takes place when a dune is under wave attack, mainly by notching, avalanching and slumping processes (Sherwood et al., 2021; Masselink and Heteren, 2014). The sediments are transported in cross-shore and alongshore directions, dependent on the result of oblique incoming waves or wave height gradients along the shore (Bosboom and Stive, 2021; Sherwood et al., 2021). Figure 2.3 provides a framework with the most important physical processes and their morphodynamic response across the shoreface, beach and backshore during storm events. In the swash regime, incident and infragravity waves run up the beach but do not reach the dune toe. Beach profiles can either erode or accrete during swash conditions and surf-zone bars migrate onshore or offshore. This depends on the balance between onshore transport by the asymmetry in wave-orbital velocity or acceleration of skewed waves and offshore transport by rip currents or undertow. In general, a few breaking waves mean onshore transport and many breaking waves mean offshore transport(Bosboom and Stive, 2021; van der Zanden, 2016). In the collision regime, swash consists of incident and infragravity waves striking the dune face. The maximum water level exceeds the dune toe but is not higher than the dune crest. Run-up collides with the dune releasing volumes of sand onto the beach, where it can be transported alongshore or offshore. This can lead to steep dune scarps. The infragravity waves contribute to the run-up on (especially gently sloping) beaches which can lead to overwash and flooding and therefore contribute to beach and dune erosion (Bertin et al., 2018; Roelvink et al., 2009). Infragravity waves become most energetic during storms resulting in offshore sediment transport. This is mainly the reason why beaches erode during storms (Bertin et al., 2018). In the overwash regime, the waves overtop the dune or berm. Sand is transported landward and not to the seaward side. In the inundation regime, the most extreme regime, the beach and dunes are completely and continually under water (Sherwood et al., 2021; Masselink and Heteren, 2014).

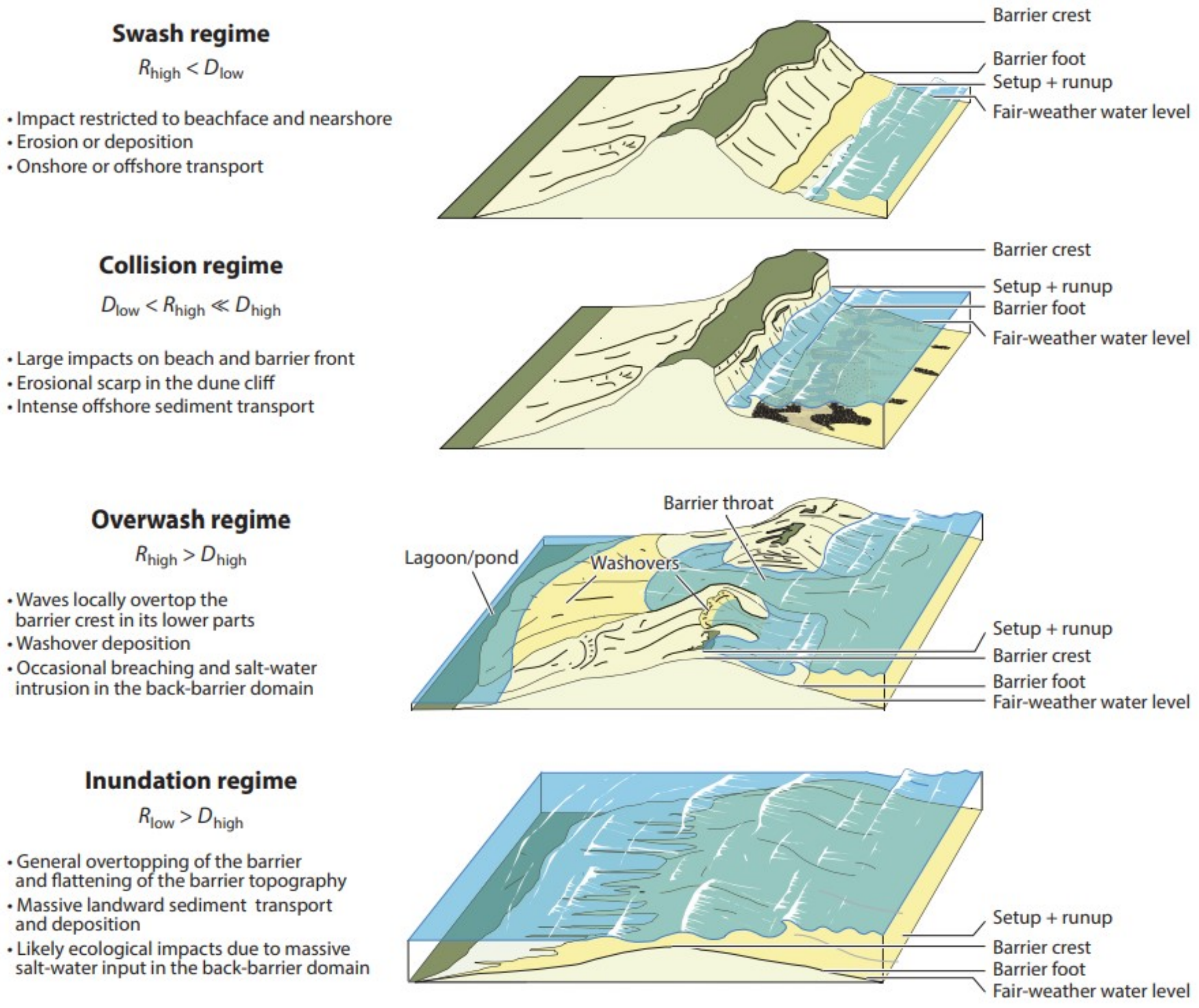

**Figure 2.3:** The Sallenger (2000) storm-impact scale. $D_{high}$ denotes the height of the dune crest, $D_{low}$ denotes the height of the dune toe, $R_{high}$ denotes the highest action of the waves (tide + surge + setup + runup), and $R_{low}$ denotes the lowest action of the waves (tide + surge + setup) (Sherwood et al., 2021).

For the Dutch coast, dune erosion takes place during storm surges when the mean water level increases and waves reach the dune face (Figure 2.4)(Bosboom and Stive, 2021). The swash and collision regimes are the most relevant for the Dutch coast (Figure 2.3). The dune-eroded sand is transported in offshore direction by a strong undertow due to breaking waves. Further seaward the flow decreases causing the sediment to settle forming a new coastal profile that fits the storm surge conditions. This newly developed foreshore increases the efficiency in dissipating energy from the incoming waves and consequently dune erosion rates decrease as the storm progresses (Bosboom and Stive, 2021; de Winter et al., 2015).

The Dutch government guarantees a safety level against flooding by law, depending on the economic value of a region. This means that flood defences in the West should resist a storm

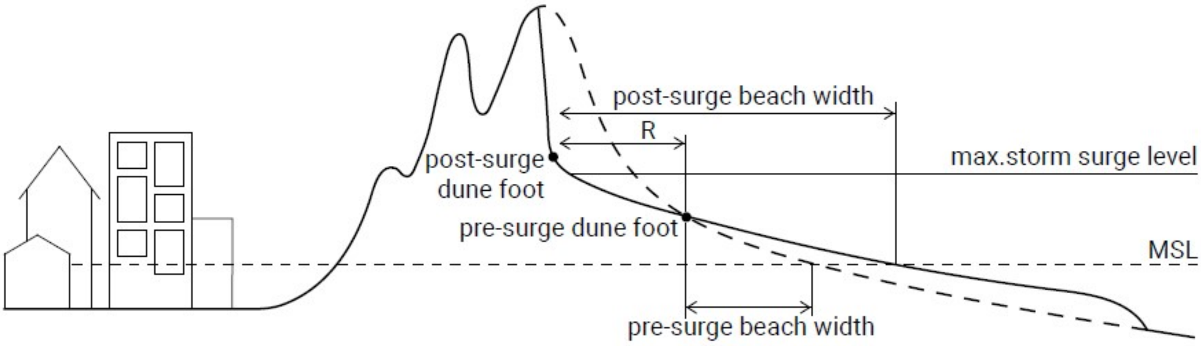

**Figure 2.4:** Typical storm surge dune erosion (Bosboom and Stive, 2021).

surge level with a frequency of exceedance of 1/10.000 year. Erosion rates of 80m to 100m of dune retreat occur during these storm conditions (offshore water level of approximately 5m to 6m above NAP and severe wave conditions, wave heights $H_s$ = 6m to 9m and peak period $T_p$ = 12s to 18s) (Bosboom and Stive, 2021; Vuik and van Balen, 2012). Figure 2.5 shows dune retreat rates for lower storm conditions as well. Knowledge of extreme storm conditions with a low probability is required to establish this relationship between dune retreat and exceedance frequency. The joint probability of extreme surge height, surge duration and wave conditions has to be determined (Bosboom and Stive, 2021; Galiatsatou and Prinos, 2016).

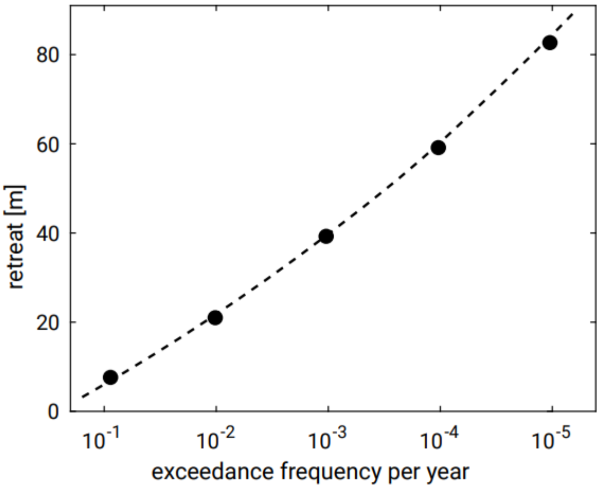

**Figure 2.5:** Dune retreat as a function of different storm design conditions (frequency of exceedance) (Bosboom and Stive, 2021).

### Alongshore variation

The potential dune erosion is often conceptualized through a comparison of the maximum water level relative to the height of the foredune toe (Figure 2.3). While this relationship between water levels and dune face geometry plays first-order control, alongshore differences are shown to be important for driving the temporal and spatial variability of dune erosion (Conlin et al., 2023). Beach and dune morphology exert an important role in dune erosion. Studies have found evidence for the relationship between beach slope/width and dune erosion. Steep beach slopes contribute to the potential for dune erosion (Cohn et al., 2021). In addition, there is a strong inverse relationship between beach width and dune erosion (Itzkin et al., 2021). Furthermore, beach slope/width relates to the height of the dune toe which influences dune erosion; dune erosion decreases with increasing dune toe height (Conlin et al., 2023). In addition, there is strong evidence that dunes are less impacted by storms when situated on dissipative flat beaches than on reflective steep beaches because dissipative beaches cause wave dissipation and limit wave run-up (Masselink and Heteren, 2014). Dune erosion also depends on the (pre-storm) dune geometry. de Winter et al. (2015) found that dune erosion is steered by the steepness of the dune front. Finally, grain sizes, beach and dune vegetation like embryo dunes and marram grass influence dune erosion (Conlin et al., 2023). Nearshore morphology also exerts control on dune erosion, for example, the location of bars (Figure 2.6). The outer bar acts as a filter for the incoming waves field (morphological template) which causes less dune erosion behind these shallow areas (Castelle et al., 2015). At multiple-sandbar sites, waves may break repeatedly and reform in the wider surf zone (Hanley et al., 2014). The behaviour of the inner bars is often influenced by wave-breaking patterns on the outer bars. During storms, the inner bar is rather flat and coupled to the outer bar with offshore-protruding inner-bar sections facing the outer-bar horn, with the notable absence of inner-bar rip channels (Castelle et al., 2015).

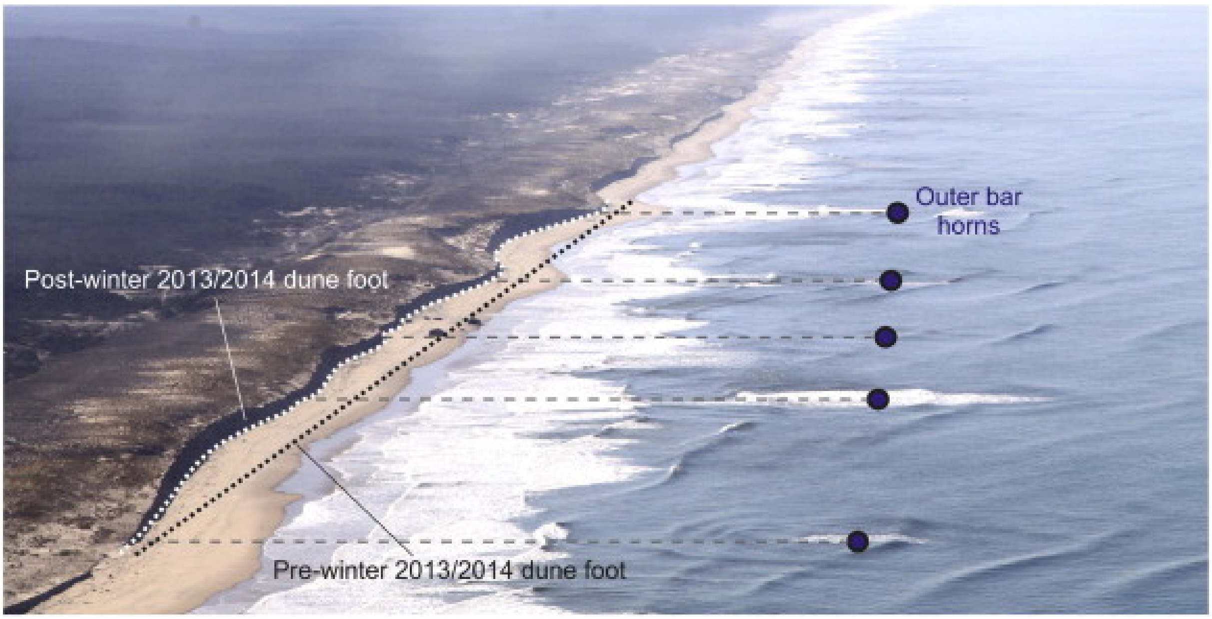

**Figure 2.6:** Megacusp horns co-located with the outer-bar horns that can be identified by (bubbles) wave breaking and/or diffraction patterns (Castelle et al., 2015).

## 2.3 Storm sequences and beach vulnerability

Storm sequences have been regarded to present a high risk for coastal systems. A storm that occurs within a sequence may lead to severe beach erosion because the beach does not have time to recover from a previous event before the next storm arrives (Eichentopf et al., 2019; Sénéchal et al., 2017; Karunarathna et al., 2014). The beach and dune profile is recovered by natural processes but the recovery process takes much longer (especially for the dune profile) than storm erosion (Baldock et al., 2021). This makes the dune system vulnerable to storm sequences (Karunarathna et al., 2014).

Storm sequences are defined as follows (Figure 2.7): Firstly, the threshold wave condition of a storm (usually a wave height ($H_{s,threshold}$) is determined and waves above the threshold are storm waves. Secondly, the maximum time interval between storms is less than the recovery time ($t_r$). For example, the first three storms in Figure 1 form a storm sequence because the time interval ($\Delta t$) between the storms is less than the recovery time under the given wave conditions (Eichentopf et al., 2019). The recovery depends on how slowly or rapidly a beach can recover after the storm. Beach recovery can be quantified by the most common parameters: (1) the recovery of previously eroded sediment volumes; (2) the change to a pre-defined beach state; (3) the recovery of the shoreline position (Eichentopf et al., 2019; Baldock et al., 2021). The definition of storms and storm sequences and the recovery of beaches is very site-specific. The definition depends on the method, wave records and beach characteristics (Eichentopf et al., 2019).

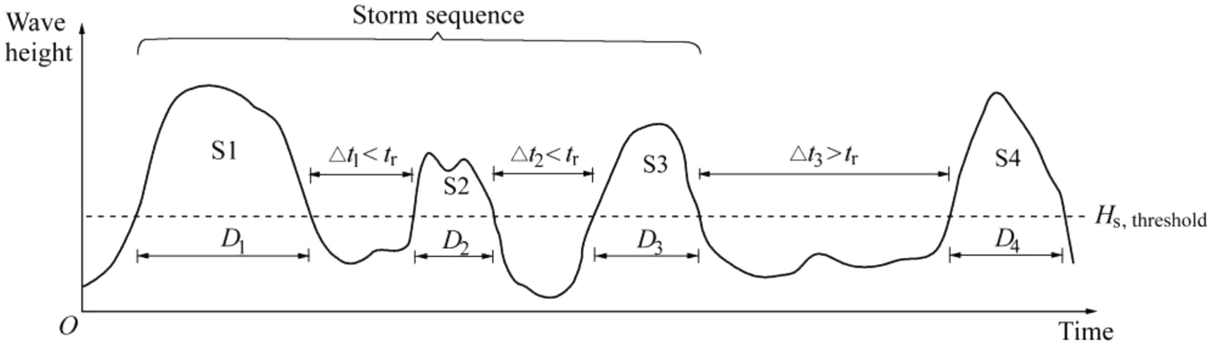

**Figure 2.7:** Qualitative definition of a storm sequence and important parameters (Eichentopf et al., 2019).

Storm sequences, rather than individual events, control the largest erosive events (Sénéchal et al., 2017). In addition to a single storm with a considerably longer return period, it appears that storm sequences with very short return periods cause the same magnitude of dune erosion (Ferreira, 2005). Karunarathna et al. (2014) investigated this and compared simulated erosion volumes induced by single storms and by storm clusters (Figure 2.8). From the figure can be observed that erosion volumes from average two- and three-storm clusters match those from single storms with return periods of two years or more. Similarly, erosion volumes from maximum two- and three-storm clusters equate to those from single storms lasting ten years or more. This highlights that beach erosion caused by storm clusters is comparable to that from a single, less frequent storm. In addition, Baldock et al. (2021) found also that individual storms can generate the same magnitude of dune erosion as storm sequences, but there is a much higher probability that extreme dune erosion occurs from a clustered event.

During storms and storm sequences, different factors have the potential to influence the vulnerability of beaches. Factors that are specifically relevant to the effects of storm sequences on beaches are the number of storms in a sequence, the chronology of the storm, the time interval between storms in a storm sequence, incident wave condition of storms, beach state and the availability of sediment within the system for the ability of a beach to erode or recover (Eichentopf et al., 2019).

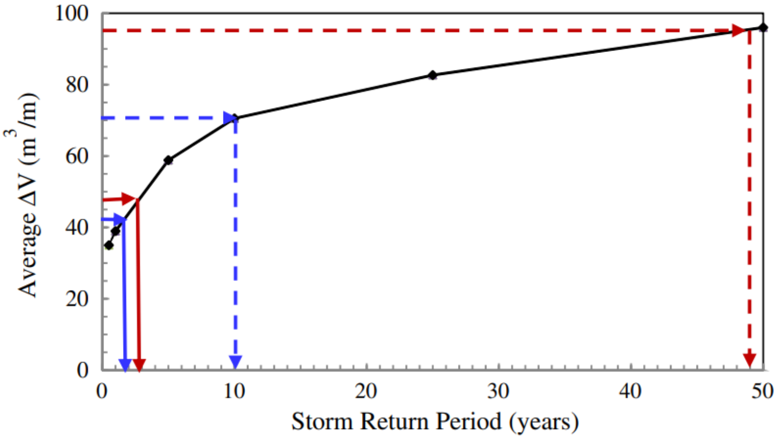

**Figure 2.8:** Beach volume change against storm return period (black line with squares — single storms; blue solid line: average 2-storm group; blue dotted line: maximum 2-storm group; red solid line: average 3-storm group; red broken line: maximum 3-storm group) (Karunarathna et al., 2014).

## 2.4 Coastline maintenance

Over the years, there has been a great political and social focus on the coastal safety of the Netherlands. After all, a storm surge in the North Sea can have disastrous consequences for the inhabitants of the low-lying country (De Winter and Ruessink, 2017). After the realization of the Deltawerken (1986/1997/2010) and the Zwakke Schakelprojecten (2015), the chances of flooding have been greatly reduced. Since 1990, sand nourishment has played an important role in maintaining coastal safety, i.e. in maintaining the sandy buffer zone in and in front of the dunes and in protecting the hinterland (van Geer, 2012). An average of 12 mln. $m^3$ is annually added to the 432 km coastline for dynamic preservation, making the Dutch coast one of the most heavily nourished coasts globally (Brand et al., 2022).

### 2.4.1 Coastal management

In 1990 the Dutch government decided to pro-actively preserve the coastline with nourishment to counter coastal erosion (Ministerie van Verkeer en Waterstaat, 1990). The Basiskustlijn (BKL) was determined as a reference coastline based on the coastline position in 1990 and the trend in changes in the coastline position between 1980 and 1990 (Ministerie van Verkeer en Waterstaat, 1990; Brand et al., 2022).

To determine the current position of the coastline, the Momentane KustLijn-position (MKL, i.e. current coastline) is used as a proxy. Each year the topography of 200-250 m spaced JARKUS-transects (raai) is measured to determine the MKL-position. The MKL, which is measured in meters in relation to a reference line, is the weighted average of the volume between the dune toe and the low water line and the same height below the low water line (Figure 2.9) (Brand et al., 2022). The MKL is assessed in relation to the BKL-position to determine if nourishment is necessary to maintain the coastline position (Rijkswaterstaat, 2021).

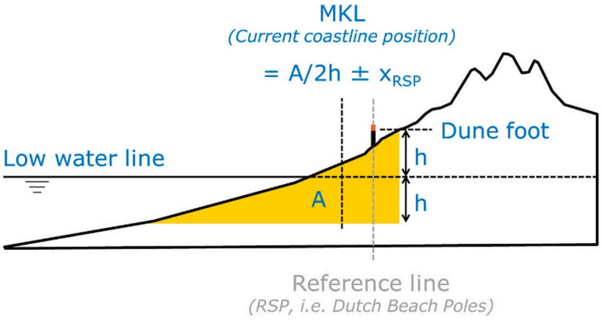

**Figure 2.9:** Determination of the MKL (current coastline position) from the sand volume in the MKL-zone (yellow)(Brand et al., 2022).

### 2.4.2 Nourishment types

The most common types of nourishment in the Netherlands can roughly be divided into three different categories, namely beach and dune, shoreface and localized mega nourishments (Stive et al., 2013)(Figure 2.10). Their differences and effects will be explained in the following paragraphs.

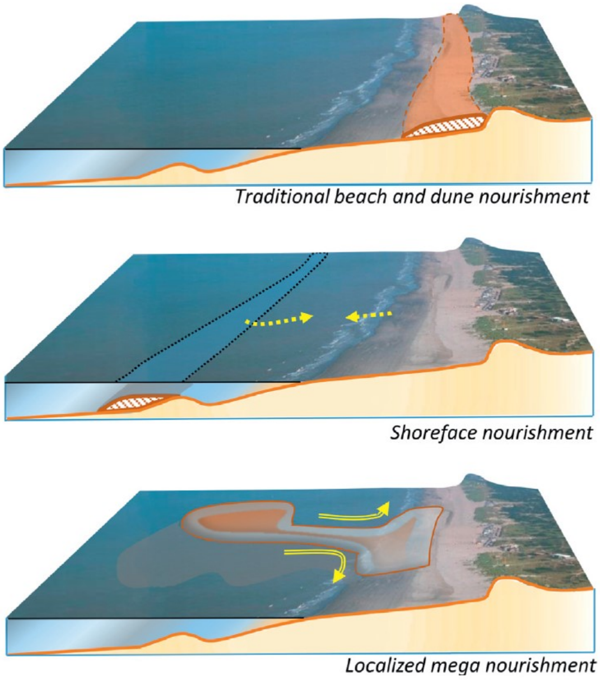

**Figure 2.10:** Different types of nourishments in the Netherlands (Stive et al., 2013).

#### Beach nourishment

Beach nourishments are the first type of nourishment carried out. Beach nourishments are usually placed and distributed as high as possible on the beach, between the dune toe (NAP +3m) and low water (NAP -1m), to use as a buffer layer or continuous source of sand depending on the location (Brand et al., 2022; Vermaas et al., 2021). The slope of the beach nourishment is as similar as possible to the natural beach profile usually chosen around 1:30. The average volume of beach nourishment is 200 $m^3/m$, as a result of accommodation capacity and the design parameters of the Dutch beaches (Brand et al., 2022).

Beach nourishments place the sand directly in the MKL-zone (Figure 2.9). Soon after construction, the volume starts decreasing because the beach is expanded artificially and will develop towards the original shape and volume (equilibrium). A large part of it is transported seaward and deposited in the lower part of the MKL-zone before disappearing. The remaining part is transported to the dunes or alongshore (Brand et al., 2022; Vermaas et al., 2021; van Geer, 2012). In the first year of the construction the rate of erosion is the strongest, approximately 40-50% of the nourished volume erodes from the MKL-zone. After the first year, the erosion rate decreases gradually over time (Brand et al., 2022). The beach nourishment remains in place for intervals ranging from 4 to 5 years (van Geer, 2012).

Beach nourishment has a greater effect on improving short-term safety than shoreface nourishment because the sand is applied directly in the MKL-zone. However, a beach nourishment has usually higher costs than a shoreface nourishment (of the same volume) (Brand et al., 2022; van Geer, 2012).

### Shoreface nourishment

Shoreface nourishment has been carried out since the early nineties (Brand et al., 2022). In the Netherlands, shoreface nourishment is often placed against a bar, generally around NAP -5m.(Brand et al., 2022; Huisman et al., 2019; van Geer, 2012). The shoreface nourishment has a positive effect on coastal protection. First, it positively influences the sediment budget of the beach (van der Spek et al., 2007). Second, the shallow depth caused by the shoreface nourishment acts like a breaker bar. The waves break on the bar leaving less energy to erode the beach. Shoreface nourishments are interesting because they remain in place for a much longer period than beach nourishments (Huisman et al., 2019; van Geer, 2012; De Keijzer, 2004). The recurrence time of a shoreface nourishment is 5 to 10 years where in the first year of the construction the volume in the MKL-zone is increased by approximately 10% of the nourished volume and this will further increase to 20-30%. The average length of shoreface nourishment is on average 4 km and the volume is approximately 450 $m^3/m$. The total volume of shoreface nourishment is on average 1.6 mln. $m^3$ (Brand et al., 2022; van Geer, 2012).

The shoreline will be positively affected (extending seawards) when the shoreface nourishment is placed against the seaward side of the outer bar. If the shoreface nourishment is placed too far from the coast its effectiveness decreases but when the shoreface nourishment is placed too close to the beach, the formation of a trough landward of the nourishment will enhance erosion of the beach. Overall, no conclusion can be drawn at which depth shoreface nourishment is most effective (Brand et al., 2022).

Several studies have investigated the behaviour of shoreface nourishment but there is still discussion about how (good) shoreface nourishments work. Observations from studies conducted are listed below.

At Egmond aan Zee, nourishments have been carried out since 1992. The shoreface nourishments are quickly absorbed into the natural system and are no longer visible as disturbances within two years. The shoreface nourishments at Egmond aan Zee have caused bar dynamics to disappear. Cyclic migration of the bars took place until 1990. Since then, the bar has been almost stable (Mastbergen et al., 2017; Cohen and Brière, 2007; Spanhoff et al., 2004). In addition, Cohen and Brière (2007) found that the shoreface nourishment in 2004 caused a landward migration of the middle subtidal bar and the outer bar remained stable. Due to the strong coupling between the coastline and bar location, it is expected that the shoreface nourishment has a positive effect on the beach. For example, the shallower location of the inner bar may provide better protection against dune erosion during storms (Mastbergen et al., 2017; Cohen and Brière, 2007). van Duin et al. (2004) found that waves break at the shoreface nourishments, causing a calmer wave climate shoreward of the shoreface nourishment area. This resulted in the trapping of sand shoreward of the shoreface nourishment. In addition, onshore transport due to shoaling waves were observed. Quartel and Grasmeijer (2007) found that the shoreface nourishment at Egmond has mainly a protective influence on the beach and, to a lesser extent but still present, a nourishing influence.

The same is observed for the bar migration at Bergen and Noordwijk (Ruessink et al., 2012). The natural cycle of cross-shore bar migration has come to a (temporary) stop at nourished sites (Brand et al., 2022)(Figure 2.11).

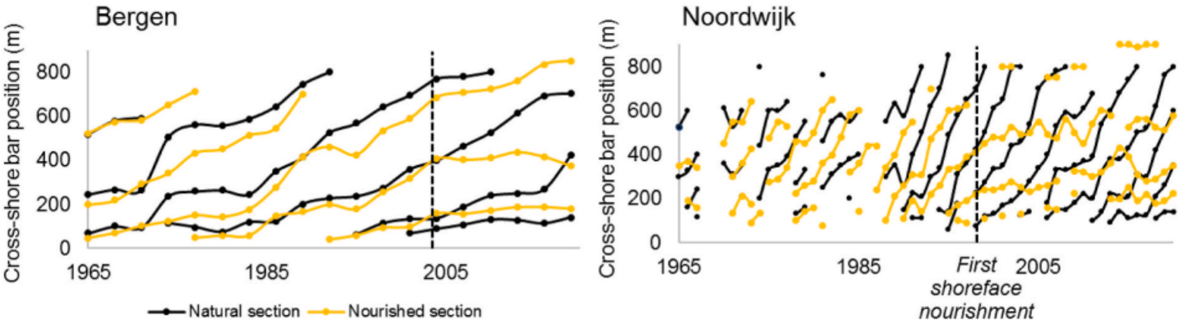

**Figure 2.11:** The influence of shoreface nourishments on bar migration for two locations: Bergen (Noord-Holland, transects 4425 in black and 3850 in yellow) and Noordwijk (Rijnland transects 7150 in black and 8200 in yellow)(Brand et al., 2022).

At Terschelling, shoreface nourishment in the trough between the middle and outer bar had a significant impact on the stability of the dynamic bar system. The bar behaviour had a 6-7 years postponement in bar development. The bar depth, height and width stabilised around the pre-nourishment values. Eventually, the bar migrational patterns resumed after 6-7 years. The shoreface nourishment was partially acting like a feeder berm; nourished sediment was distributed and transported upwards in the profile and along the shore towards the east of the coast (Grunnet and Ruessink, 2005).

At the Delfland coast, shoreface nourishment stimulates sandbar development at unbarred sections of the coast. In addition, the shoreface nourishment pushed the existing bars towards the coast resulting in onshore transport (Radermacher et al., 2018).

(Huisman et al., 2019) analyzed bathymetric data of 19 shoreface nourishments located on the Dutch coast to observe and model the shoreface nourishment behaviour. The shoreface nourishments are more persistent compared to beach nourishment with 65% on average volume still in the initial nourishment region after three years. This resulted in a long-term (3 - 30 years) cross-shore supply of sediment to the beach but with a small impact on the local shoreline shape. Considerable cross-shore profile change takes place at the shoreface nourishment while the impact on the coast is hard to distinguish. The losses of the nourishment region are mainly caused by cross-shore transport partly driven by water-level setup-driven currents (rip currents) and increased velocity asymmetry of the incoming waves (Figure 2.12). Energetic wave condition ($H_{mo} \geq 3$m) causes most erosion of the nourishment as milder waves are propagated without breaking over the nourishment.

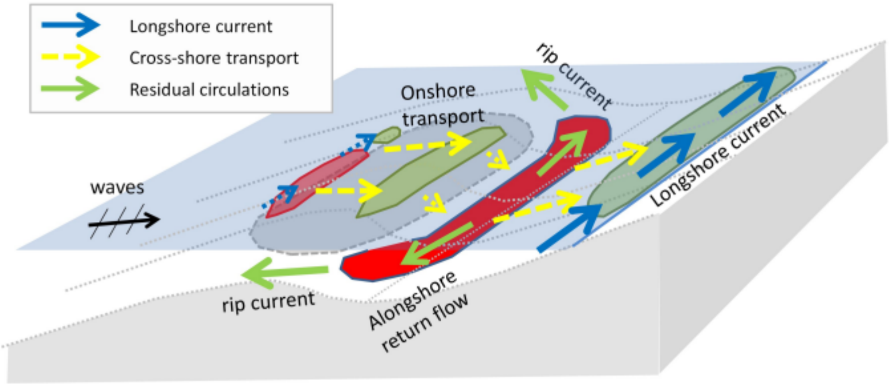

**Figure 2.12:** Sediment redistribution at shoreface nourishments. Red areas mean erosion of the bed, green areas sedimentation of the bed (Huisman et al., 2019).

### Localized mega nourishment

Localized mega nourishment is a recent innovation and not part of the regular coastline maintenance of the Dutch coast but they can become regular types when proven effective (Brand et al., 2022). Mega nourishment is intended to act as a long-term (decades) source of sediment for the adjacent coast by redistributing sand in cross and alongshore directions (Radermacher et al., 2018; Stive et al., 2013). Only a few have been executed, one of them being the Sand Engine. The Sand Engine was constructed in 2011 where 21.5 mln. $m^3$ of sand was added to the coast (Brand et al., 2022). The Sand Engine is expected, with a recurrence time of once every 20 years, to be more efficient and effective in the long term than beach and shoreface nourishments (Stive et al., 2013).

The Sand Engine surveys show volumetric losses of 10% of the added volume where 70% of these losses were found to be compensated by accretion on adjacent coastal sections and dunes, confirming the feeding property of the mega nourishment. The feeding property is related to incident wave power where months with high-energy waves result in more alongshore spreading and months with small wave heights result in cross-shore spreading of the nourished sediment (de Schipper et al., 2016).

## 2.5 Research gaps

The previous sections provide an overview of the current knowledge relevant to this study. Beach-dune erosion is studied extensively but in relation to single storm events, calling for further research to improve the knowledge of the complex morphodynamics of coastal areas affected by storm sequences. In addition, there is a lack of research on the buffering effect of nourishments on coastal protection during a storm sequence. Hence, the research question is as follows

***What is the effect of nourishments on dune erosion during a storm sequence?***

The main question is split up into the following sub-questions:

1. What is the difference between a nourished and adjacent non-nourished coast during a storm sequence?
    - How does morphology differ between the two areas?
    - How do dune erosion volumes differ?
    - How do dune erosion temporarily and spatially differ?
    - How do hydrodynamics like short wave and infragravity wave differ?
2. What is the protective effect of different nourishment designs on dune erosion during a storm sequence?
    - How does nourishment geometry (depth, cross-shore position, volume per m) affect dune erosion?
    - How do different nourishments affect hydrodynamics?

To answer these questions, a numerical model, various bathymetries of a partially nourished coast and offshore wave and tide data are used to investigate the differences between a nourished and adjacent non-nourished coast and to simulate the effect of nourishments and different nourishment designs on dune erosion during a storm sequence. A more detailed description of the methods used to answer the questions is provided in the next Chapter.

# Chapter 3

# Methodology

The previous chapters provided an introduction to the research, gave background information, and identified gaps in the literature upon which the research questions are based. This chapter describes the methodology used to answer the research questions. The study approach is described in Section 3.1. Sections 3.2 and 3.3 describe the study location and the data used, followed by Section 3.4 where the numerical model, the model input/output, and validation are described. Section 3.5 presents a scheme illustrating the various simulations. Finally, Section 3.6 describes how the model output is converted into usable results and how these results are analysed.

## 3.1 Study approach

The XBeach numerical model is used for the computation of nearshore hydrodynamics and the morphological response during a storm sequence, such as dune erosion. A detailed description of the numerical model is given in Section 3.4.

To get an answer to the first question, *'What is the difference between a nourished and adjacent non-nourished coast during a storm sequence?'*, bathymetric data from various dates of Egmond aan Zee (hereafter referred to as Egmond) were used (beach pole 37 - 42), separated at a nourished and non-nourished boundary (beach pole 39.5), to investigate the difference in morphology. In addition, different storm sequence simulations were done to investigate the hydrodynamic and morphological differences between these two sites. Furthermore, a simulation was conducted to assess the impact of removing the outer subtidal bar, which had been formed and maintained through shoreface nourishments in the past.

To get an answer to the second question, *'What is the protective effect of different nourishment designs during a storm sequence?'*, different nourishment designs were modelled and compared to the initial result without nourishment. To go into further detail, the nourishment design of 2023 - 2024 for Bergen/Egmond was implemented in the most recent survey, October 2023, where in addition other alternatives for this design were modelled. The modelled results with the nourishment designs were compared with the initial results (bathymetry 10/2023 vs bathymetry 10/2023 + nourishment).

The next Sections delve more into detail on Egmond, data, the numerical model, model settings, model input/output, simulation schedule, and analysis of the model output.

## 3.2 Study site

The Dutch coast is located on the southeastern edge of the North Sea basin and can be roughly divided into three sections. From north to south: the Wadden Sea, the Holland coast (Den Helder to Hoek van Holland) and the Delta area (south of Hoek van Holland). As mentioned before, this study focused on Egmond, located at the 120km long Holland coast (Figure 3.1a). The Holland coast is a closed sandy coast whose orientation shifts from NE-SW in the south to N-S in the north. The beaches are usually 300m long, with a slope between 1:35 and 1:60 and an average grain size between 250 and 350 $\mu$m. The morphology of the Holland coast is characterized by a dynamic sandbar system. The number of sandbars varies between 1 and 3 (Brand et al., 2022; Quartel and Grasmeijer, 2007).

The Egmond study site stretches from beach pole 37 - 42. Egmond serves as an interesting study site because of the nourishment history (Figure 3.3). The northern part (in this study: beach pole 37 to 39.5) is influenced by nourishments whereas the southern part is undisturbed (in this study: beach pole 39.5 - 42). Figure 3.1 shows this area and an example of a bathymetry where the blue dotted line is the boundary between the nourished and non-nourished site. Egmond is roughly north-south orientated and is primarily exposed to North Sea-generated sea waves. The annual mean offshore significant wave height $H_{m0}$ and period $T_{m02}$ are about 1.3 m and 4.5 s, respectively. The monthly mean $H_{m0}$ is significantly higher in winter than in the summer (1.8 vs 0.9 m). $H_{m0}$ can rise to above 7 m with storms moving in from the northwest. The tide is semi-diurnal with a neap and tidal range of approximately 1.4 and 1.8 m, respectively. Storm surges, particularly when the wind comes from the northwest to the north, can elevate the sea level by more than 1 m. However, southwesterly winds are the most common. The Egmond coast is characterized by 2 - 3 subtidal bars and an intertidal bar on a gently sloping intertidal (1:40) beach. The beach state is mainly dissipative. The profile steepens landward of the high-tide level and transitions into the steep (1:2.5) front face of the foredune at an elevation of around 3 m above NAP. The profile changes abruptly at a height of 14 to 17 meters above mean sea level, and it then slopes gradually upward to the foredune crest at a height of 20 to 25 meters above NAP. European marram grass is abundant throughout the foredune, particularly in the more gently sloping section of the foredune. The steep foredune slope is the result of earlier dune erosion occurrences due to rotational failure of the foredune. The alongshore variability in shape and height of the foredune is generally small. Embryo dunes can form after several years without dune erosion. Especially the southern site, between beach pole 40 and 42, is characterized by a pronounced embryo dune (Grasmeijer et al., 2023; Ruessink et al., 2019; Quartel and Grasmeijer, 2007).

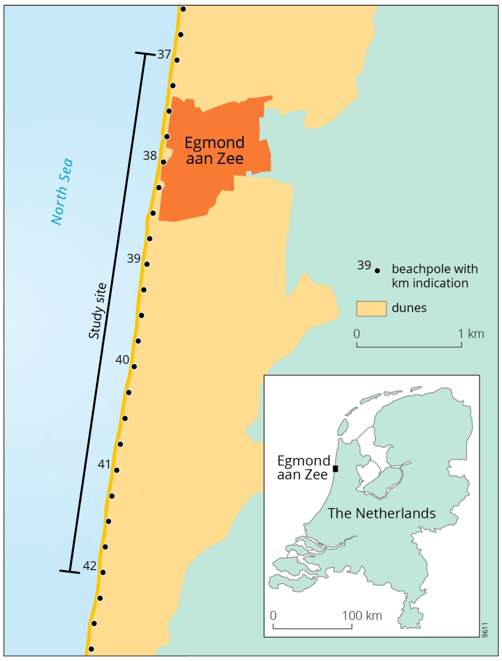

**(a)** Study site (Ruessink et al., 2019)

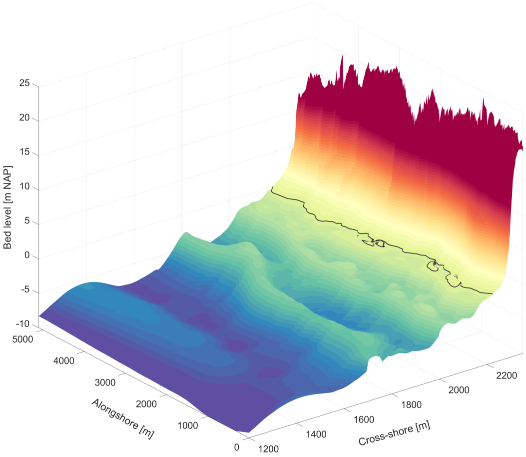

**(c)** 3D bathymetry

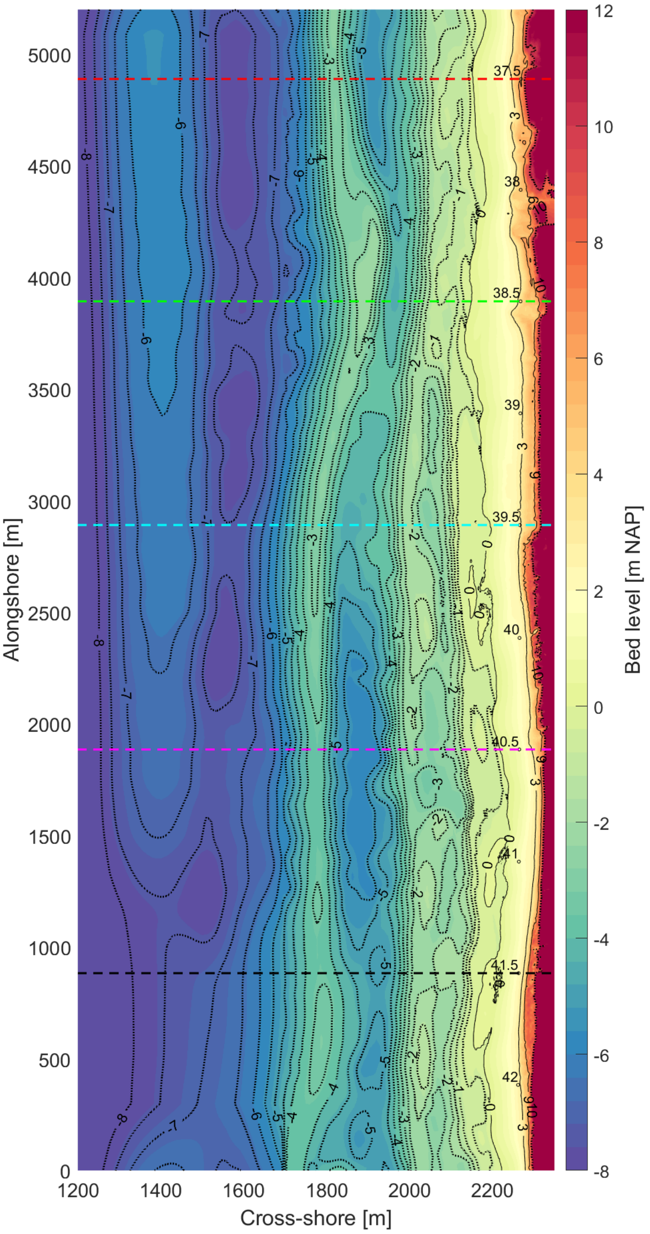

**(b)** Bathymetry from beach pole 37 - 42.5 in October 2023. The dashed lines are cross sections shown in Figure 3.2. The blue dashed line is the boundary between the nourished (north) and non-nourished (south) sites.

**Figure 3.1:** Study site and bathymetry. For Figure 3.1b and 3.1c, the origin of the grid is located at a southwestern point offshore. The grid is rotated with 8 degrees to get the x-axis oriented approximately perpendicular to the coastline.

Egmond has a high alongshore morphological variability (Figure 3.1b, 3.1c and 3.2). The subtidal sandbars (breaker bars) are located at x ≈ 1400m (outer subtidal bar), x ≈ 1800m (middle subtidal bar) and x ≈ 2000 (inner subtidal bar). The intertidal bar is located at x ≈ 2100m. These locations vary annually (Section 3.3). A clear distinction can be made between the nourished and non-nourished part of the study site. The outer subtidal bar is more present in the nourished site, due to shoreface nourishments in the past (Mastbergen et al., 2017). In addition, the middle subtidal bar in the nourished site is more shallow and closer to the shore

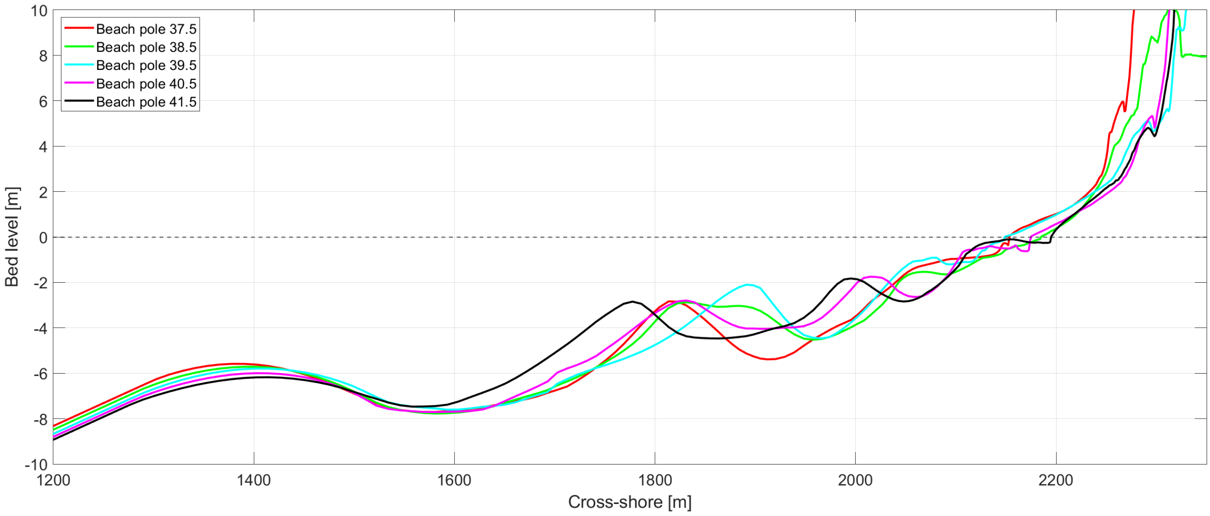

**Figure 3.2:** Transect for different beach poles at October 2023.

than in the non-nourished site. In the nourished site, this is coupled by a remarkably regular variety of depths and shallows in the inner subtidal bar, which is characteristic of a shallow bar interrupted by rip currents. Furthermore, between the middle and inner subtidal bar in the nourished site are some deeper areas (between x = 1850 and 2000m) which are smaller compared to the deeper area in the non-nourished site (between x = 1800 and 2000m).

Part of the village of Egmond lies directly by the sea. In the past, Egmond was located further seaward but that part of Egmond was swallowed up by the sea. Nowadays, a boulevard is constructed between beach pole 37.25 and 38 as a protection for Egmond and recreation. To protect this boulevard, the BKL has been extended further seaward than it was in 1990 causing an erosion 'hotspot' where nourishment is needed (Mastbergen et al., 2017). In addition to the boulevard, beach houses are placed annually between beach pole 37 and 39.5 (Kustviewer, 2024). Egmond has been extensively studied in recent years due to erosion 'hotspots' and the short lifetime duration of nourishments. Since 1992 nourishment has been carried out from beach pole 28 to 41 (Figure 3.3). These nourishments have influenced the natural bar dynamics. Cyclic migration of the bars took place until 1990. Since then, the bars have been almost stable. The coastline position and the bar system appear strongly linked. This is an important observation because shoreface nourishments strongly influence the bar system and therefore are expected to have a clear effect on the coastline (Mastbergen et al., 2017). The applied shoreface nourishment is quickly absorbed into the natural system. Within two years of nourishment, they are no longer visible as a disturbance (see shoreface nourishment behaviour in bathymetries in Appendix B; last shoreface nourishment was implemented in 2019). South of Egmond, the coast is almost stable and only limited maintenance efforts have been carried out. The bars still seems to exhibit natural (cyclic) dynamics in this coastal section (Mastbergen et al., 2017).

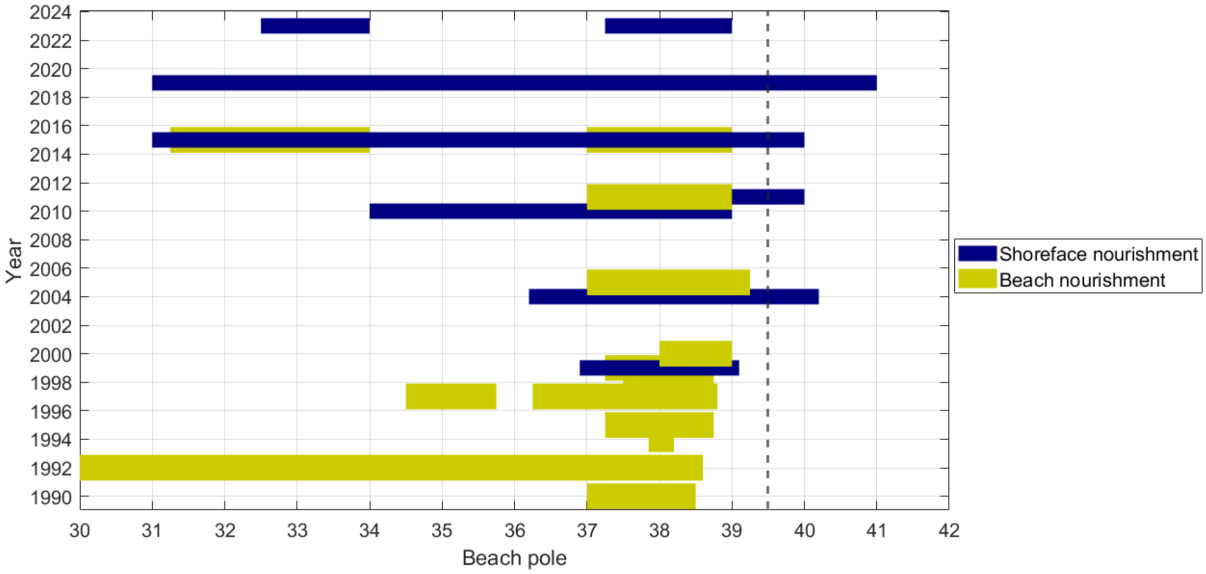

**Figure 3.3:** Nourishment history Egmond (data retrieved from Rijkswaterstaat). The vertical dashed line represents the division between the nourished (left) and non-nourished (right) sections.

## 3.3 Study data

This Section describes the bathymetric data that were used and what was observed from this data. Furthermore, the wave and tide data are also presented.

### 3.3.1 Bathymetric data

Since 2020, the bathymetry and topography between beach pole 37 and 43 at Egmond has been surveyed annually by Ruessink et al. (2019). The surveys carried out in March 2020, October 2020, March 2021, March 2022, October 2022 and October 2023 were used in this study. Only the surveys of these dates were used for this study, as the surveys conducted before 2020 cover an alongshore distance from beach pole 39 to 43 where a part of the nourished site is not included (Grasmeijer et al., 2023). The bathymetric data were collected by quad, survey wheel, jetski and UAV in cross-shore transects with a 50-meter alongshore spacing from the dune toe to approximately 700 meters from the beach. Every 250-meter spaced Jarkus transect was extended to about 1 kilometre from the beach (Grasmeijer et al., 2023; Ruessink et al., 2019).

#### Observations

Section 3.2 described mainly the observations from the Egmond bathymetry of October 2023. This paragraph presents also the observations from the different bathymetries used in this study.

The main observations from these bathymetric data were as follows: First of all, the height of the outer subtidal bar reduced over time. This was likely the result of cross-shore transport (Section 2.4.2). Second, the middle subtidal bar in the nourished site was more shallow and closer to the shore than in the non-nourished site. Additionally, the middle subtidal bar remained stable or migrated landwards in the nourished site. This was in line with the observation from Cohen and

Brière (2007). Moreover, the middle subtidal bar became straighter after March 2021, almost parallel to the coastline. This may have been due to the turbulent winter of 2021/2022 where energetic wave conditions straightened up the bar line. Third, there was a consistent presence of deeper areas in the nourished site (between x = 1850 and 2000m) and a deep area in the non-nourished site (between x = 1750 and 2000m) which reached up to NAP -6m. The deep area in the non-nourished site was moving slowly southward. The deeper areas in the nourished site were almost stable. Furthermore, the location of the waterline and bar system seemed linked. The waterline was located more seaward in the nourished site and more landward in the non-nourished site (contour line NAP 0m). Especially between beach pole 38.5 and 40 the beach was relatively wide (Figure 3.4a). The lower part of the foredune, between the contour lines of NAP +3 and +6m, was narrower in the non-nourished site (Figure 3.4b). This related to the morphology of the foredune, which was characterized by a pronounced embryo dune in the non-nourished site, while this embryo dune was absent in the nourished site.

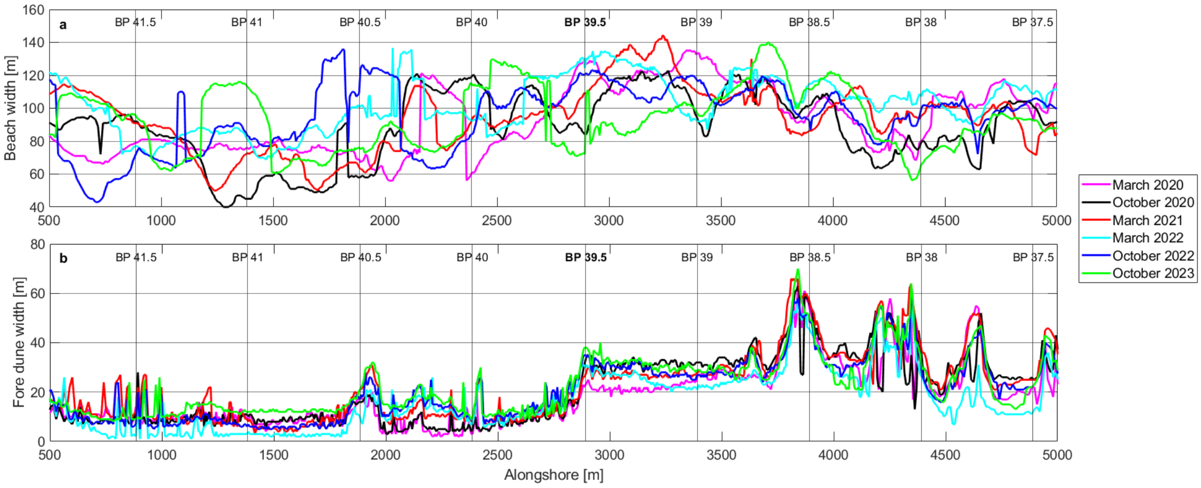

**Figure 3.4:** a - The alongshore beach width (NAP +0 - 3m) and b - fore dune width (NAP +3 - 6m) of Egmond during the different bathymetric dates.

Appendix D showed the difference in bed level between the bathymetries. The main observations from these difference maps were as follows: the difference in bed level between March 2020 and October 2020 showed some erosion and accretion of the beach and mainly accretion of the dune area. The difference in bed level between March 2020 and October 2020 showed some erosion of the dune and beach. The biggest bed level difference was noticed between March 2021 and March 2022 because of the turbulent winter of 2021/2022. Dune erosion occurred in the north, between beach pole 37.5 and 38.5, and a relatively big hotspot was visible in the south, between beach pole 40.5 and 41.5. In addition, the beach also showed erosion. The difference in bed level between March 2022 and October 2022 showed mainly the accretion of the dune and beach area. The difference in bed level between October 2022 and October 2023 showed a relatively high magnitude of accretion of the foredune. The higher beach area also showed accretion whereas the lower beach area showed erosion. Seasonal effects were noticeable with more erosion in winter periods.

### 3.3.2 Wave and tide data

The water level data were measured at the 'IJmuiden buitenhaven' tidal station located 20 km south of Egmond and the wave data were measured by the 'IJmuiden munitiestortplaats' wave buoy, located about 40 km west-southwest of Egmond in a water depth of 25 m. The water data were retrieved via an open Rijkswaterstaat data source, named Waterinfo.rws.nl. The spectral significant wave period $T_{m02}$ were converted into the peak period $T_p$ as $T_p = T_{m02}$ x 1.33 (Ruessink et al., 2019).

## 3.4 XBeach

XBeach is a numerical model used to compute littoral hydrodynamics and morphodynamic response during storm events, such as dune erosion, overwash and breaching. XBeach includes the hydrodynamic processes of short wave transformation (refraction, shoaling and breaking), long wave (infragravity wave) transformation (generation, propagation and dissipation), wave-induced setup and unsteady currents, as well as overwash and inundation (Figure 3.5). The morphodynamic processes include bed load and suspended sediment transport, dune face avalanching, bed update and breaching (Roelvink et al., 2015).

Various simulations were run on XBeach 1D and 2DH to provide answers to the research questions. This section will describe the model settings, input, output and validation. For a full description of the model formulation, see Roelvink et al. (2015).

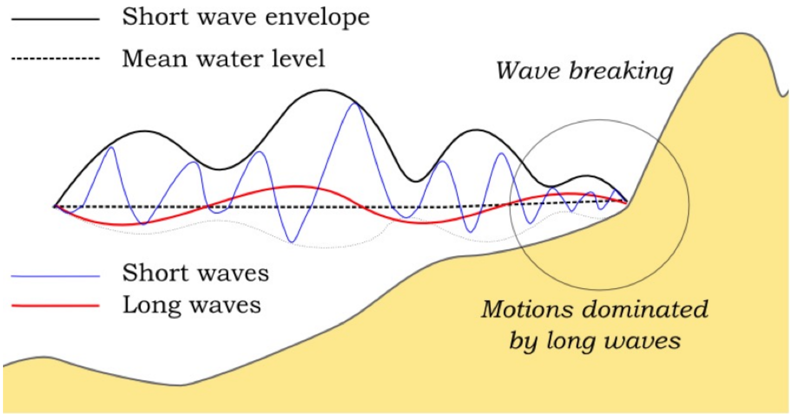

**Figure 3.5:** Relevant wave processes (Roelvink et al., 2015).

### 3.4.1 General

A directory structure is needed to execute XBeach. It consists of the file *params.txt* and the parameter files that will be read by the *params.txt* file. The *params.txt* file is essential since it provides various adjustable settings and parameters. If everything is set correctly XBeach will start computing and give output per specified timestep in a netcdf file named 'xboutput.nc'.

To make a simulation with a JONSWAP spectrum (like this study) the following parameters are essential (Roelvink et al., 2015):

- Grid files with values for x and y (*x.grd* and *y.grd*);

- Bathymetry file that matches with the grid (*bed.dep*);
- JONSWAP file which contain the wave input (*jonswap.txt*);
- Tide file which contain the tide input (*tide.txt*).

This study uses the settings of the BOI-version of XBeach. The settings of this BOI-version of XBeach have been partially validated by field data from Egmond. The hydrodynamics and morphodynamics were validated through field measurements at Egmond (from beach pole 39.5 to 42) during a winter storm in January 2019. The overall conclusion of this validation is that the (1D) XBeach model is sufficiently well capable of simulating nearshore hydrodynamics and morphodynamics (dune erosion) (Coumou et al., 2022). See Appendix A for the model settings and Roelvink et al. (2015) for a description of the settings.

### 3.4.2 Model input

**Bathymetry and grid**

The bathymetric data described in Subsection 3.3.1 is interpolated in a BOI-guidelines established grid (Grasmeijer et al., 2023). This grid is coarser offshore which reduces the simulation time. The size of the domain of this grid is 2405 meters in the x-direction and 4480 in the y-direction. The cell size varies between a minimum size of 5 and a maximum of 10 meters in the y-direction and a minimum size of 1 and a maximum of 22.26 meters in the x-direction. For this study, the cell size in the y-direction was multiplied by 1.2, while maintaining the same number of grid cells, to include the northern site of Egmond since the BOI-version focused more southward (Coumou et al., 2022). The size of the domain of this enlarged grid is 2405 meters in the x-direction and 5376 in the y-direction. The cell size has a minimum size of 6 and a maximum of 12 meters in the y-direction and a minimum size of 1 and a maximum of 22.26 meters in the x-direction.

Cyclic boundary conditions were used, which treat two lateral boundary regions as if they are physically connected. Waves, flow and sediment transport that exist in the domain at one side will be transported toward to other side. It is important to make the two grid rows of bathymetric data on the lateral boundaries identical to the ones on the other side. The advantage of cyclic boundary conditions is that there are no shadow zones (Roelvink et al., 2015). In this study, the model output at the lateral boundaries was ignored because this output is not accurate due to the cyclic boundaries (focus is between y = 500 and 5000m).

**Storm sequence**

For this study, a storm sequence that happened in early 2022 was chosen. Storm Corrie (29 to 31 of January) and Dudley, Eunice and Franklin (18 to 21 of February) brought elevated water levels in several coastal sectors along the Dutch coast (Figure 3.6). For this study, the wave data measured during these four storms are used to make a simulated storm sequence (Subsection 3.3.2). The threshold wave condition ($H_{s,threshold}$) of the sequence was defined as 3 meters so the waves above the threshold are the storm waves (grey boxes in Figure 3.6). The data measured in this grey area was used as the storm data. The storm data was joined together naturally to create a simulation of a storm sequence (Figure 3.7). This was also the input data for XBeach (*jonswap.txt* and *tide.txt*). Storm Corrie records the highest values with a peak wave height of roughly 7m and water level of 2.6m. During this peak, the wave direction was mainly W-NW. After the storm Corrie, Eunice and Franklin recorded wave heights of 6.3m and 5.2m and water levels of 1.8m and 2.1m during the peak. The wave direction is mainly S-W.

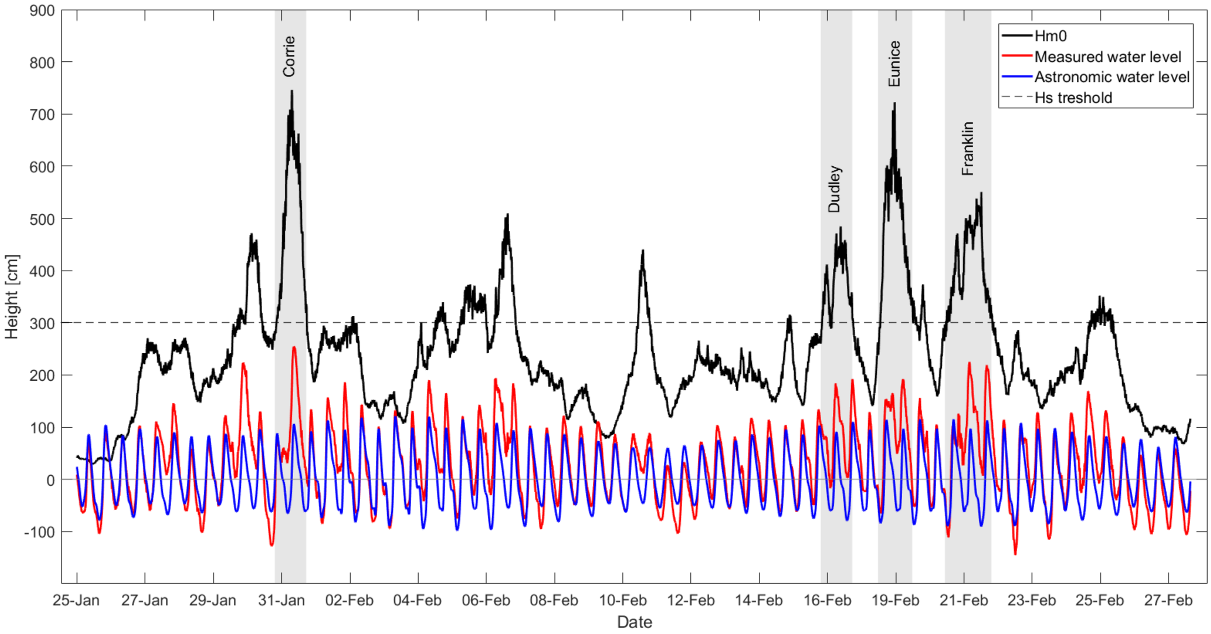

**Figure 3.6:** Measured and astronomic water level and wave data during storm sequence 2022. The dotted line is the threshold wave condition and the grey boxes present the storm waves.

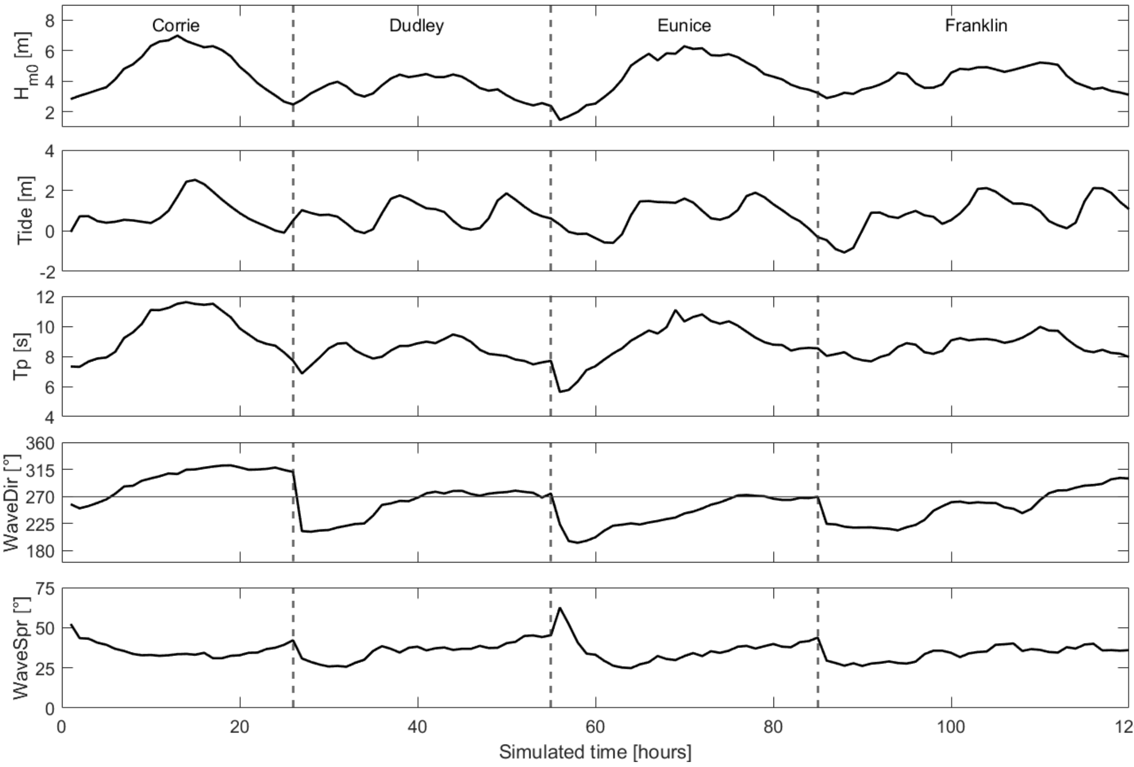

**Figure 3.7:** Simulated storm sequence.

### 3.4.3 Model ouput

The bed level ($z_b$) output was saved every 0.5 hours and the water level ($z_s$), rms-wave height $H_{rms}$, velocities ($u$ and $v$), and sediment transport rates ($S_{utot}$ and $S_{vtot}$) were saved as model output every hour. The spectral significant wave height of the short waves ($H_{m0,SS}$) was calculated as $\sqrt{2} * H_{rms}$ and the spectral significant wave height of the infragravity wave ($H_{m0,IG}$) was calculated as $8 * \sqrt{z_s var}$. These output and calculations were used to make the 2D figures like bed level difference and hydrodynamic plots.

Fixed points were located at the cross-shore location of the beach poles on NAP +0 and 3m to look more into detail at the hydrodynamics at the beach. In addition, two cross-shore fixed points were located in the nourished site and two in the non-nourished site to look in detail at the cross-shore wave evolution of the short and infragravity wave height. At the location of the fixed points, the water level ($z_s$), bed level ($z_b$), and rms-wave height ($H_{rms}$) were saved as model output every second. The fixed points model output was post-processed into consecutive bursts of 15 minutes. Only the bursts in which the sensor was continuously submerged were considered to calculate mean water levels and significant wave heights in the short ($H_{m0,SS}$) and infragravity ($H_{m0,IG}$) wave frequency bands. $H_{m0}$ of the short waves was calculated as $\sqrt{2}*H_{rms}$ and root-mean-square-averaged over 15-min blocks. $H_{m0}$ of the infragravity waves for the fixed points were determined from the spectral integration of the detrended water level signal ($z_s$) in the 0.005 - 0.05 Hz domain for 15-min blocks. The water level height was calculated as the mean of $z_s$ of the 15-min blocks. Furthermore, to look more in detail at the water level, also the result of $z_s$ per second were observed.

### 3.4.4 XBeach validation

The previous section described how the XBeach model was set up and which data was used. This section describes the validation runs that were done before simulating the final XBeach output. The results of these validations are shown in Chapter 4.

First, the XBeach model results with a normal grid size were compared with the XBeach model results with a coarser grid size to examine the differences (section 3.4.2). This was achieved by executing the simulated storm sequence on the October 2022 bathymetry for both normal and coarser grid sizes. This is done because the grid size may influence the processes of XBeach and therefore the final output. Second, the XBeach model was validated by comparing the results with observed data. This validation was conducted by running the simulated storm sequence with the March 2021 bathymetry and comparing the outcomes with the observed difference between March 2021 and March 2022, as the simulated storm sequence occurred during this period (Figure 3.6). The validation process involved two methods. The first method was the continuous method, where the simulated storm sequence was run without stopping the simulation between storms (Figure 3.7). The second method was the cumulative method, running the storms separately and summing up the differences. Third, the effect of a non-erodible layer in XBeach was investigated. This was prompted by the XBeach model exhibiting an unrealistic bar shift during a storm sequence. The investigation into the effect of a non-erodible layer involved three 1D simulations at different beach poles namely 38.5, 39.5 and 41.

## 3.5 Simulation scheme

The previous Section gives a general description of the numerical model XBeach, the model input/output and the validation of the model output. This section gives an overview of the different simulations that were done with XBeach to answer the research question. The same storm sequence was used for each simulation (Section 3.4.2), only the bathymetries differ (Section 3.3.1). To answer the first sub-question, simulations with the six bathymetries from the various dates were done. In addition, one simulation with an adjustment to the bathymetry of March 2021 was performed (Table 3.1). The adjustment involved the removal of the outer subtidal bar to assess the impact on wave breaking (Figure 3.8). The result of simulation seven gives insight into the effect of the outer bar which covers sub-questions one and two.

**Table 3.1:** Simulation overview first question.

| Nr. | Bathymetry |
|---|---|
| 1 | March 2020 |
| 2 | October 2020 |
| 3 | March 2021 |
| 4 | March 2022 |
| 5 | October 2022 |
| 6 | October 2023 |
| 7 | March 2021 - outer subtidal bar removed |

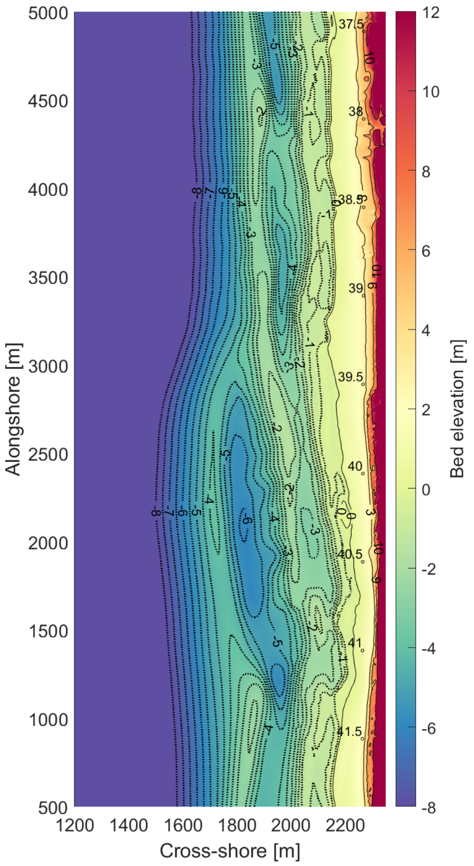

**Figure 3.8:** Bathymetry March 2021 without outer subtidal bar.

To answer the second sub-question, seven simulations with the bathymetry of October 2023 with a nourishment design were performed (Table 3.2). See Appendix E for a map and cross-section of the nourishment designs. Simulation numbers 8 to 11 present shoreface nourishment at different depths and with different volumes. Simulation number 8 is the Bergen/Egmond design which was implemented in 2023/2024. Simulations 12 and 13 present beach nourishment with different volumes. Simulation number 14 is shoreface nourishment also carried out in the southern part of Egmond.

**Table 3.2:** Simulation overview second sub-question.

| **Nr.** | **Bathymetry** | **Bed level [m NAP]** | **Volume [m$^3$/m]** | **Location [BP]** | **Slope [m/m]** |
|---|---|---|---|---|---|
| 8 | October 2023 | -5.5 | 375 | 37.25 - 39.0 | 1:20 |
| 9 | October 2023 | -5.5 | 750 | 37.25 - 39.0 | 1:20 |
| 10 | October 2023 | -3 | 375 | 37.25 - 39.0 | 1:20 |
| 11 | October 2023 | -3 | 750 | 37.25 - 39.0 | 1:20 |
| 12 | October 2023 | 0-3 | 100 | 37.25 - 39.0 | 1:30 |
| 13 | October 2023 | 0-3 | 200 | 37.25 - 39.0 | 1:30 |
| 14 | October 2023 | -5.5 | 375 | 37.0 - 42.0 | 1:20 |

## 3.6 Model output analysis

In the previous section, an overview of the different XBeach simulations was provided. This section described how the XBeach output of the simulations was converted to obtain useful results, and how these results were analyzed to address the research questions.

For the first question, morphological changes were studied by quantifying bed level differences for the various bathymetries. Dune evolution was the focus of the analysis, while bar and beach evolution were excluded as XBeach did not predict this well (Chapter 4). Bed level differences were obtained by subtracting the initial bed level from the bed level at the end of the simulation ($z_{bstorm}$ - $z_{b0}$). Additionally, a more detailed analysis was done by calculating the alongshore dune erosion volume. The dune erosion volume [m$^3$/m] was calculated as the area between the pre-and post-storm profile above the dune toe (Figure 3.9).

By investigating alongshore dune erosion, differences between the nourished and non-nourished sites of Egmond became clear. The average dune erosion volume for the nourished and non-nourished sites was determined by calculating the mean of the alongshore dune erosion volume north and south of beach pole 39.5.

Hydrodynamics were studied to look at the drivers of the morphological changes. The hydrodynamics were studied by looking at the water level ($z_s$), short waves ($H_{m0,SS}$), and infragravity waves ($H_{m0,IG}$) in 2D and on fixed points. The 2D plots were utilized to provide an overview of the hydrodynamics during peak storms. Peak storms were defined as the timesteps characterized by maximum dune erosion. Scatter plots were conducted for the infragravity wave height measured at fixed points on NAP 0m in the nourished site against the non-nourished site. The nourished site category consisted of four fixed points north of beach pole 39.5, while the non-

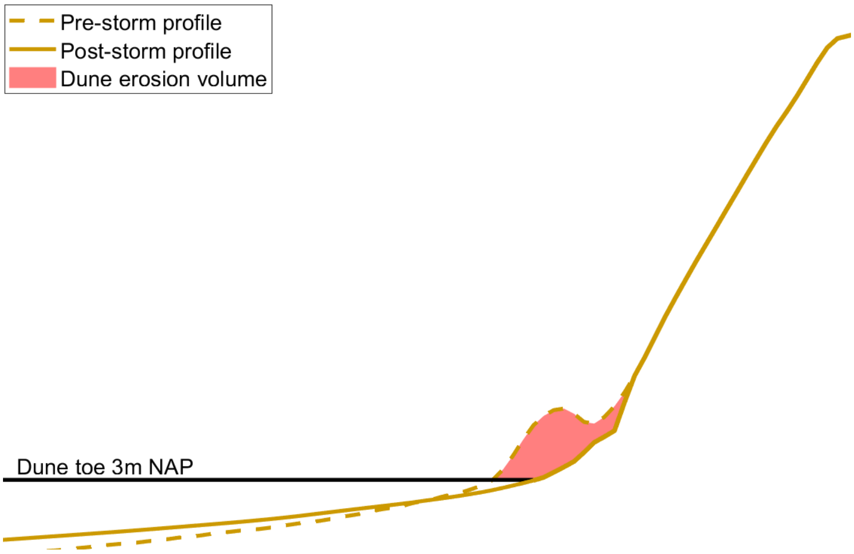

**Figure 3.9:** Schematic dune profile with the definition of the dune erosion volume.

nourished category consisted of four fixed points south of beach pole 39.5. Linear regression was added to the scatter plots to predict which site had a larger infragravity wave height.

To examine other drivers for morphological changes, the relationship between alongshore morphological variability and alongshore dune erosion was investigated, conforming to Pearson's correlation coefficient (r). The correlation between dune erosion volume and the slope of the surf zone (NAP -4.5 - 0m), inner surf zone (NAP -1.5 - 0m), beach (NAP +0 - 3m), and foredune (NAP +3 - 6m) of the initial bed was determined (Figure 3.10). The slope was calculated as the difference in bed level divided by the width of the zone converted to degrees. This method attempted to find a relationship between the deeper areas in the (inner) surf zone and the erosion hotspots. When the deeper areas are closer to the shore, the slope of the (inner) surf zone will increase. The same applies to the beach and foredune. When the beach and foredune width decreased, the slope increased, which might cause dune erosion. This method was used in previous studies like Cohn et al. (2021).

The correlation coefficient ranges from -1 to +1. The strength of the correlation coefficient was categorized as follows. If the value of the correlation coefficient is close to -+1, then it indicates a strong relationship. If the value of the correlation coefficient is between -+0.5 and -+0.8, it suggests a moderate relationship. If the value of the correlation coefficient is less than -+0.5, it suggests a weak relationship.

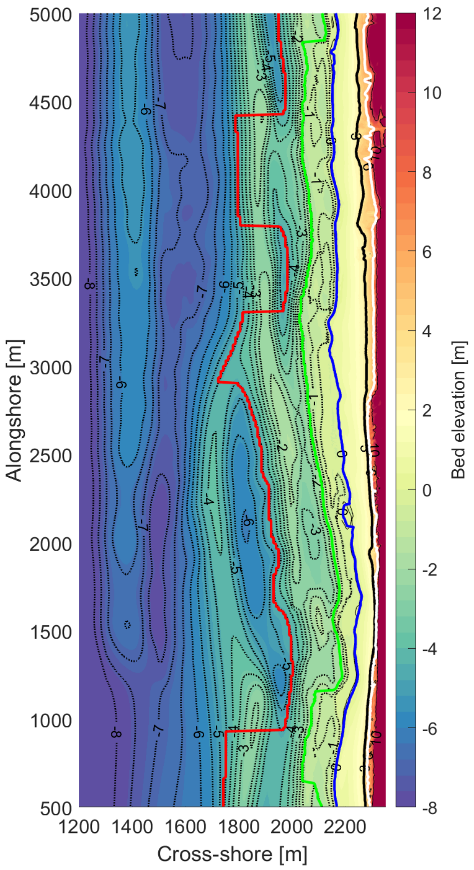

**Figure 3.10:** Bathymetry March 2021 with location surf zone (red to blue line), inner surf zone (green to blue line), beach (blue to black line) and dune (black to white line).

The effect of the outer subtidal bar (created and maintained by nourishments) on dune erosion was investigated by simulating the bathymetry of March 2021 without an outer subtidal bar (Figure 3.8). This simulation was compared to the simulation with the bathymetry of March 2021 with the outer subtidal bar (Figure B.1c), including an examination of dune erosion volume and hydrodynamics.

For the second question, the dune erosion volume of the nourishment design was calculated in the same way as the first question. The dune erosion volume of the nourishment designs (Section E) was compared with the dune erosion volume of the bathymetry without the designs (bathymetry 10/2023). In addition, some 2D hydrodynamic maps are analysed to get an overview of the effects of nourishment.

In essence, this study does not seek exact magnitudes but trends that explain the difference between the nourished and non-nourished sites of Egmond.

# Chapter 4

# XBeach validation

This chapter provides insight into the steps taken to better understand the XBeach model and the validation runs that were done before simulating the final XBeach output. This chapter shows how (1) the grid applied to the study site compares to the BOI-guidelines established grid (section 3.4.2), (2) how the modelled results relate to observed results, and (3) the effect of different non-erodible layers in XBeach. Per section, it is explained why each step is taken.

## 4.1 Coarsening alongshore grid resolution

The differences between a bathymetry in the normal grid and a coarser grid which is alongshore extended are shown in Figure 4.1. As explained in Section 3.4.2, the coarser grid includes more alongshore kilometres which is visible in the Figure (see y-axis).

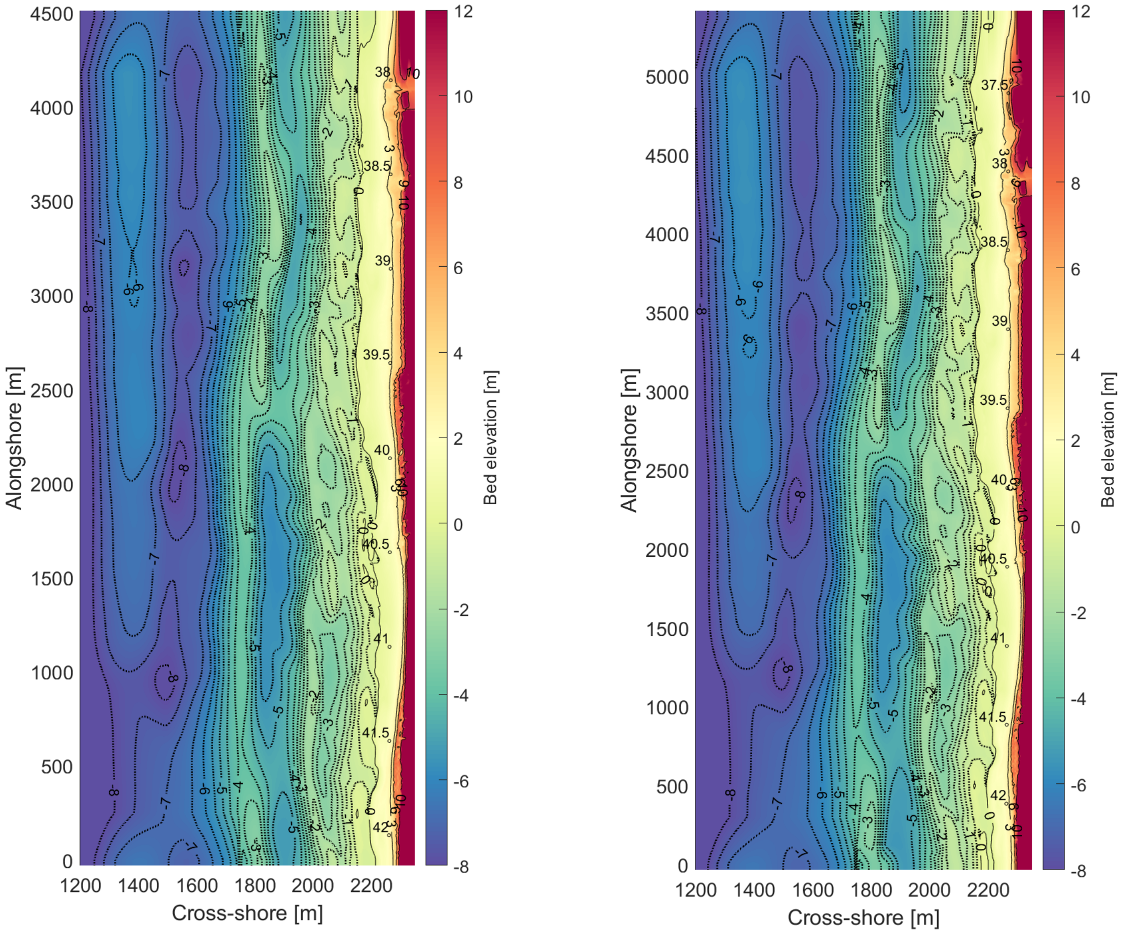

**(a)** Normal grid

**(b)** Coarser grid

**Figure 4.1:** Bathymetry October 2022.

The bed level differences modelled by XBeach with the normal and coarser grid are shown in Figure 4.2. The two figures are aligned next to each other on beach pole locations for a good comparison of the differences. Visually there are no big differences. The locations of erosion and deposition are the same.

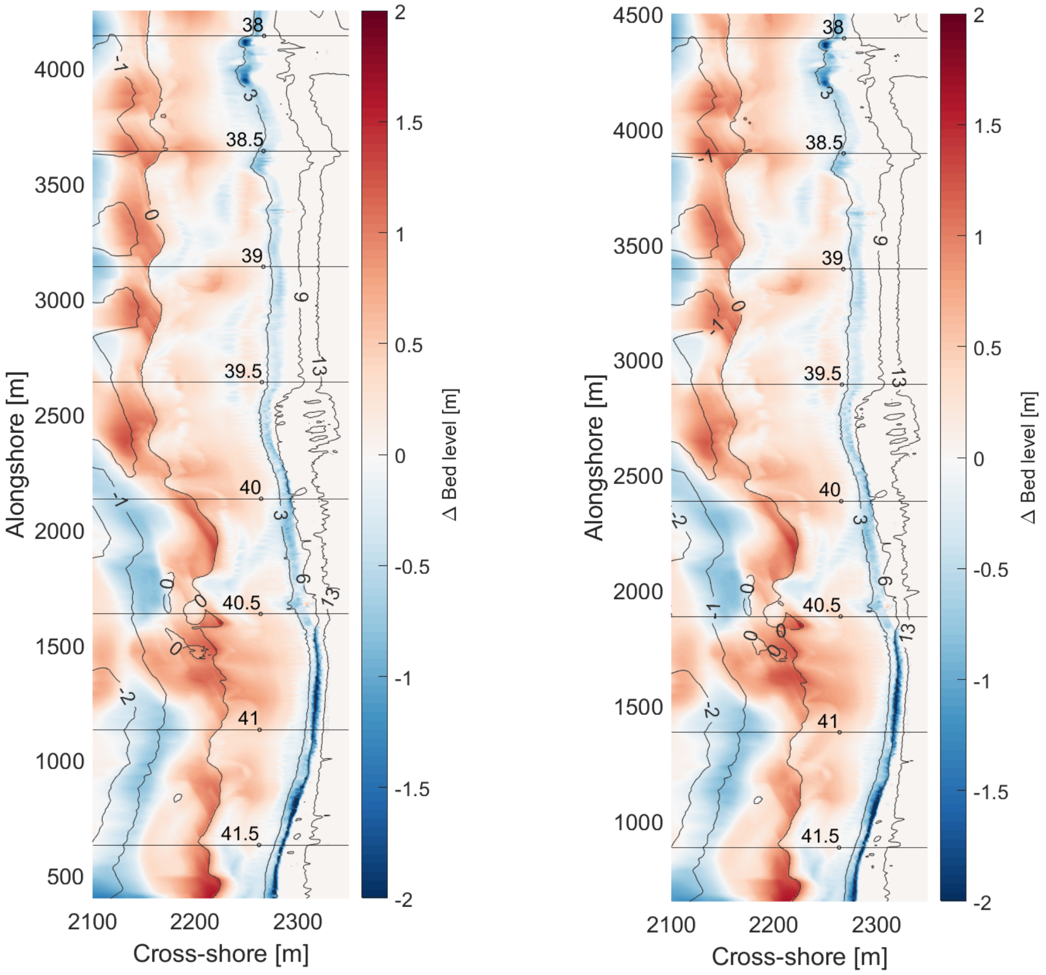

**(a)** Normal grid

**(b)** Coarser grid

**Figure 4.2:** Bed level difference.

Figure 4.3 shows the alongshore dune erosion volume for both grids. The two lines show the same pattern where there are minor differences. Around x = 3500 to 4000, a difference can be seen in the amount of dune erosion. The simulation with the coarser grid predicts less dune erosion than the normal grid. It was still decided to continue with the larger grid since (1) it gives an overall nice result compared to the normal grid and (2) for this study there is interest in the differences in trend between a nourished and non-nourished site in terms of erosion and not for specific erosion numbers.

## 4.2 Observed vs modelled

Figure 4.4 shows the differences between the observed and modelled bed level changes. Figure 4.4a shows the bed level differences between March 2021 and March 2022 (observed), Figure 4.4b shows modelled bed level differences with the bathymetry of March 2021 and the simulated

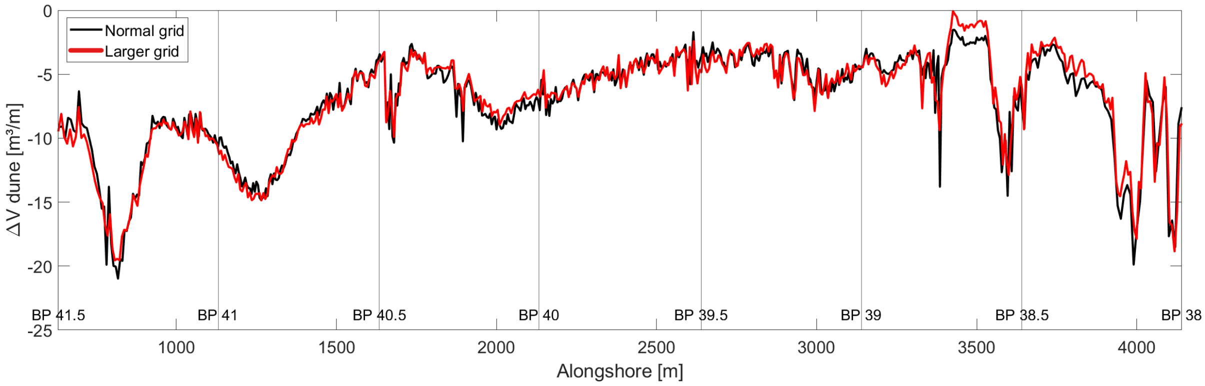

**Figure 4.3:** Alongshore dune erosion volume for the normal grid and larger grid.

storm sequence. For this simulation, the entire sequence is simulated continuously, as depicted in Figure 3.7. Figure 4.4c also shows modelled bed level differences with the bathymetry of March 2021 and the simulated storm sequence, but for this simulation, the storms in the sequence were simulated separately after which the differences in bed level were summed; the cumulative method. For the modelled differences between each storm, see Figure 4.5 and 4.6 and for cross sections of the observed vs modelled data Appendix F.

Visually, it can be noted that the location of dune erosion matched reasonably well. The location of the dune erosion hotspot in the south is well-modelled. The model does not properly predict the bed level differences between the bars and the beach. During the sequence, the bars are mainly flattened out and pushed onshore. This does not match the observed data where the bars are mainly going offshore (Figure F.1). In addition, bars migrate offshore by a storm event (Bosboom and Stive, 2021). This modelled bar movement pushed the intertidal bar on the beach causing a lot of deposition on the beach (Figure 4.4). This does not match the observed data. The bed level differences are more pronounced in the cumulative method because the bed level changes are summed.

The alongshore volume change of the dune and beach is plotted in Figure 4.7. The beach volume change is defined as the volume between the pre-and post-storm profile between NAP +0 - 3m. As mentioned before, the location of the dune erosion hotspot in the south is well-modelled (Figure 4.7a). Overall, the model predicts less alongshore dune volume changes. This can be explained because the difference in the observed data is over one year, so there is an accretion of the beach and dune in the calm summer months and in the north, the movement of sand takes place for various economic activities on the Egmond boulevard. JARKUS data was measured just after the storm so this does not add to the validation. For the alongshore beach volume changes, the modelled data does not fit the observed data. As mentioned before, this can be explained by the onshore bar movement.

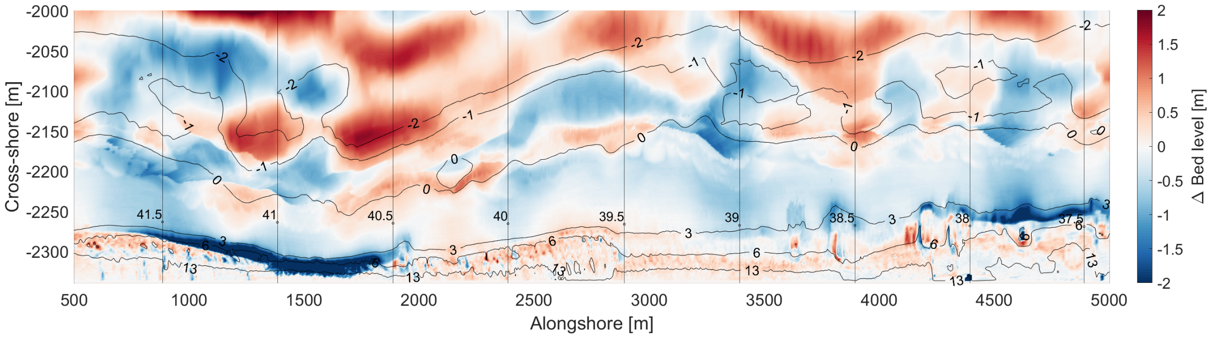

**(a)** Observed: the difference between March 2021 and March 2022.

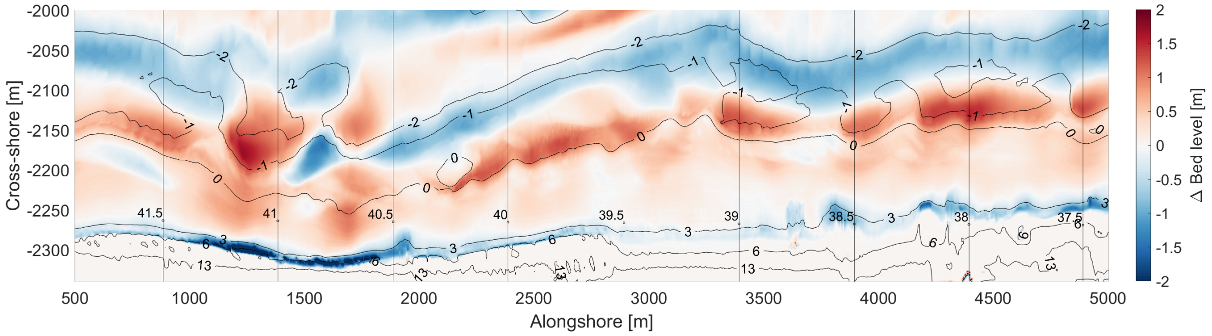

**(b)** Modelled result: run with bathymetry March 2021 and simulated storm sequence continuing.

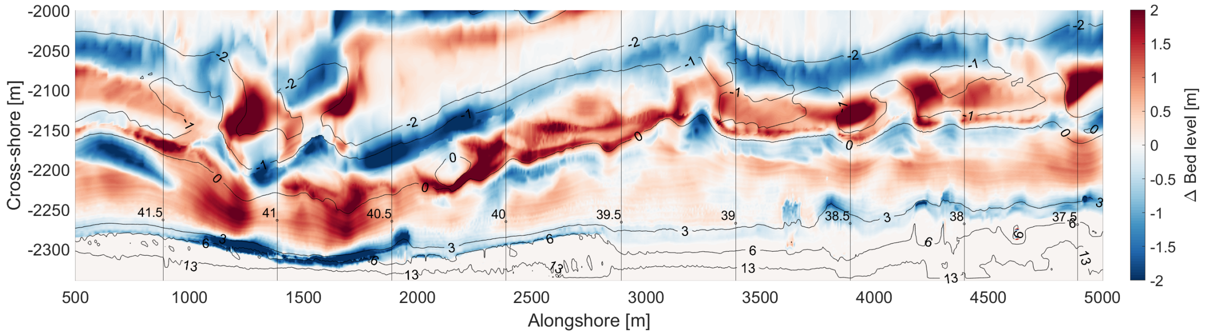

**(c)** Modelled result: run with bathymetry March 2021 and simulated storm sequence cumulative.

**Figure 4.4:** Bed level difference; observed vs modelled.

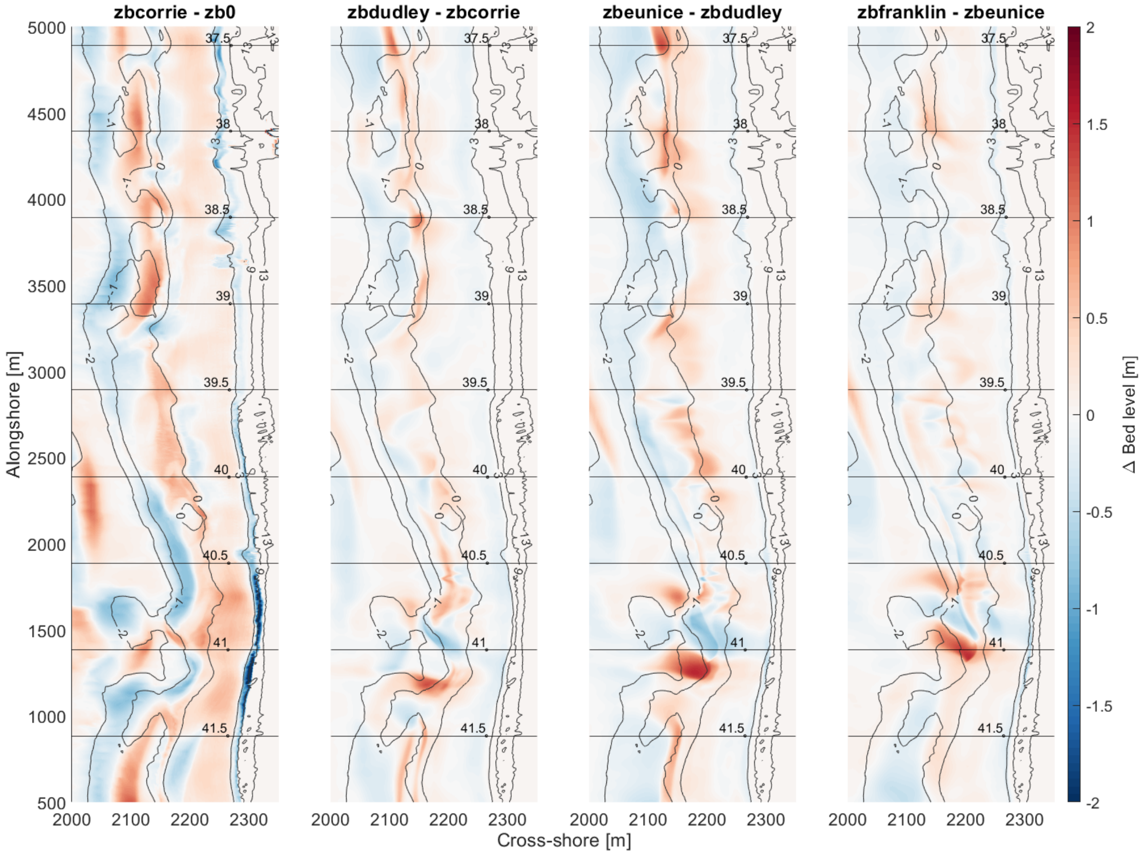

**Figure 4.5:** Differences between the storms for storm sequence continuing 4.4b.

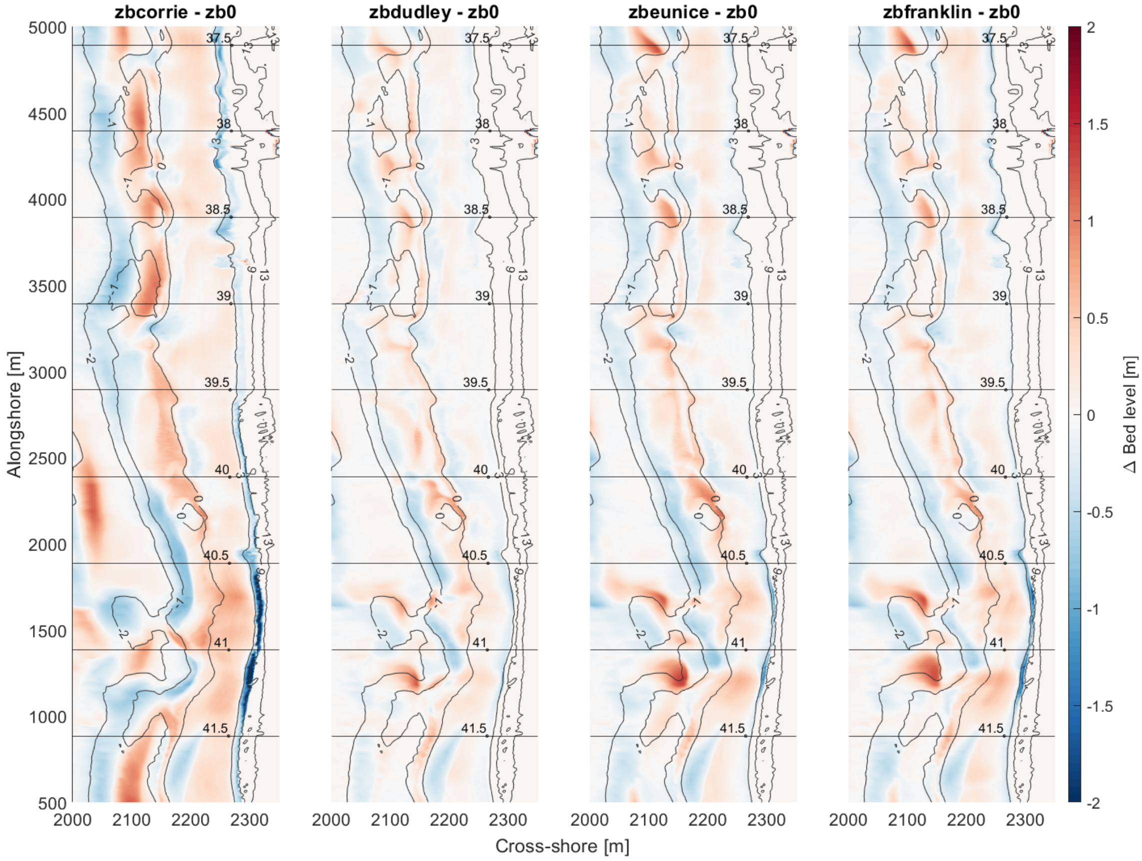

**Figure 4.6:** Differences between the storms for storm sequence cumulative 4.4c.

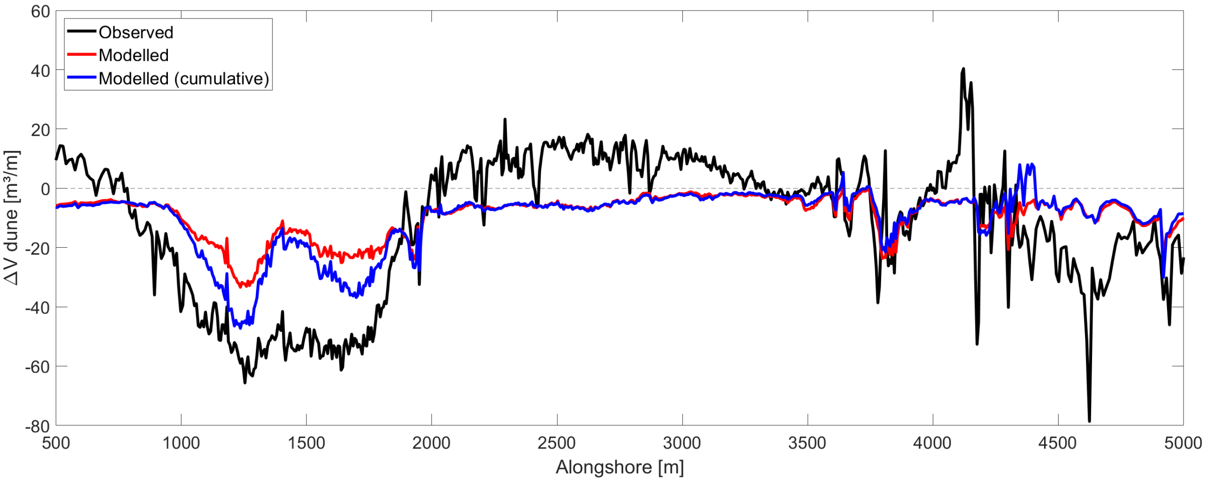

**(a)** Dune

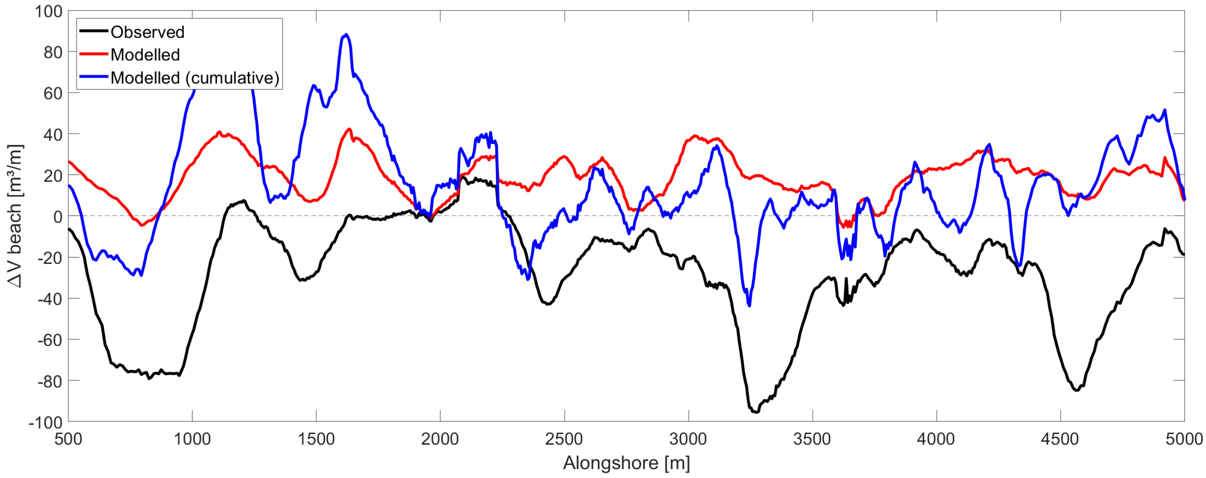

**(b)** Beach

**Figure 4.7:** Alongshore volume change; observed vs modelled.

## 4.3 Non-erodible layer

XBeach has a feature to locally fix the bed also called a non-erodible layer (*ne-layer*). This feature fixes the bed in such a way that no morphological changes happen in this area. This is a way to prevent the bars from shifting during the sequence. To investigate the effect of a non-erodible layer on improving the modelling of beach and dune evolution during the sequence, three 1D simulations were performed with cross-sections of the March 2021 bathymetry at beach poles 38.5, 39.5, and 41. This section highlights the results at beach pole 39.5. Appendix G highlights the results from beach posts 38.5 and 41.

Figure 4.8a, G.1a and G.2a show the initial bed level, the bed level at the end of the simulation of a dynamic bed, and the bed level at the end of a simulation for different elevations below which a non-erodible layer is applied. Several things can be observed. First, bars below a certain non-erodible layer height are fixed but just above this height there is a jump/scour in bed level. Second, the dune change shows small differences for the different non-erodible levels. Third, the beach change shows a large difference for the different non-erodible levels. This has to do with whether the bar is pushed on the beach or not due to the height of the non-erodible layer.

Figure 4.8b, G.1b and G.2b shows the average volume change for dune and beach. The maximum elevation of the non-erodible layer has little effect on the volume change of the dune but an important observation is that when the outer subtidal bar is fixed, less dune erosion occurs than when the bed is dynamic. Thus, the outer subtidal bar (created and maintained by shoreface nourishments) affects the amount of dune erosion. Storm Corrie has the greatest effect on dune volume change. Despite the maximum height of the non-erodible layers, the model continues to move sand to the beach. Where the non-erodible layer in this method is defined on an elevation level, for the final XBeach output the non-erodible layer will be fixed based on x (cross-shore location).

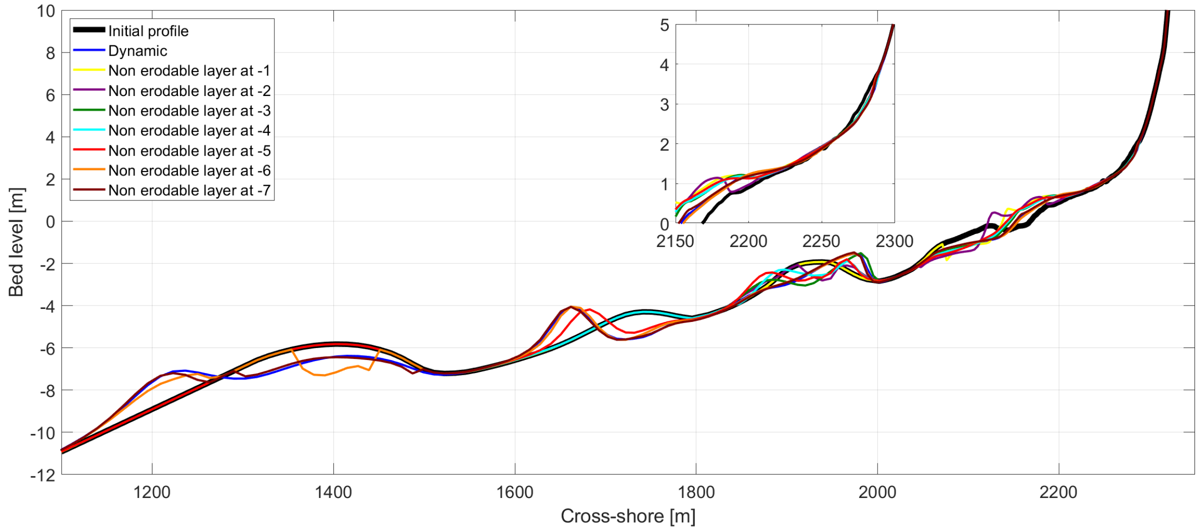

**(a)** Run with a cross-section at beach pole 39.5 of the bathymetry of March 2021 and simulated sequence 3.7.

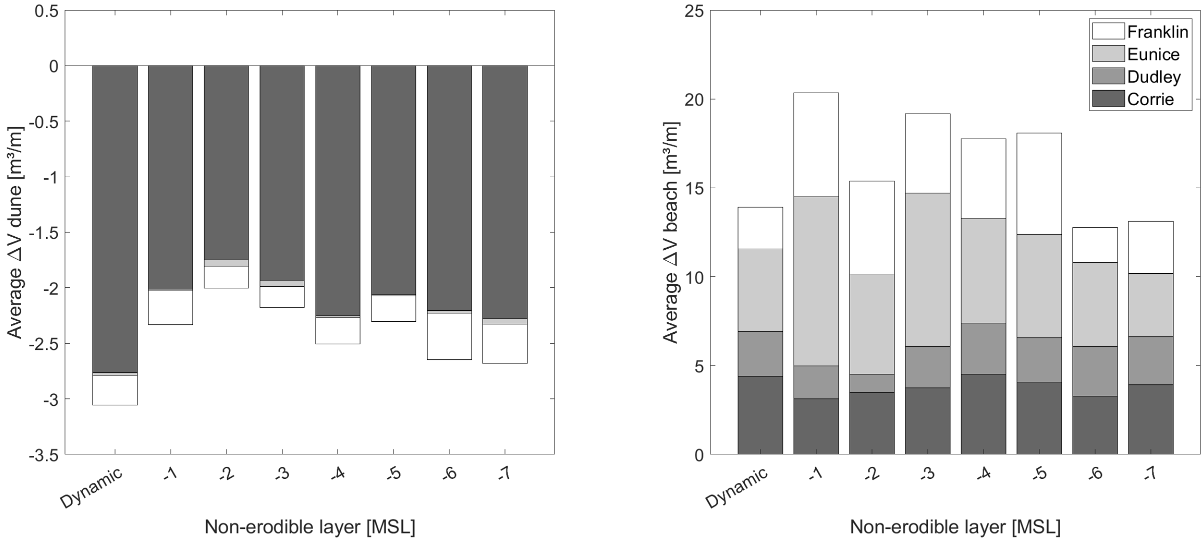

**(b)** Dune and beach volume change for the simulation with different levels of non-erodible layers.

**Figure 4.8:** Results 1D run beach at pole 39.5.

## 4.4 Conclusions on validation

First, this study only focuses on dune evolution and not on bar and beach evolution because XBeach models the dune erosion rates with sufficient confidence, as opposed to the bar and beach evolution. Second, the coarser grid, which includes the northern site of Egmond gives overall good results allowing us to continue simulating with this grid. Third, due to better comparison with observed data, the cumulative method was selected as the preferred approach for simulating a storm sequence. This method reduced simulation time, as storms could be run simultaneously, and their outcomes could be summed up. Fourth, The non-edible layer method prevents bars from moving and has an overall minimal impact on dune erosion but an important observation is that fixing the outer subtidal bar results in a reduction of dune erosion. For the final XBeach output, the outer subtidal bar is fixed (everything seaward of $\approx$ 1600m) since XBeach flattened out the bars and predicted onshore bar movement. In addition, this study is interested in the effect of the outer subtidal bar at Egmond since it is created by nourishments and the 1D runs show that it affects the amount of dune erosion. Where the non-erodible layer in the XBeach validation is defined on an elevation level, for the final XBeach output the non-erodible layer is fixed based on x (cross-shore location).

# Chapter 5

# Results

This chapter presents the main XBeach results. Section 5.1 highlights the XBeach results using the bathymetry data from March 2021, focusing on the analysis of dune erosion and its driving factors, as well as the description of hydrodynamics in 2D and on fixed points. Section 5.2 summarizes the XBeach results obtained from the various bathymetries, showing temporal and spatial variability in dune erosion, factors contributing to this variability, differences in erosion between nourished and non-nourished sites, and variations in storm impacts. In addition, differences in infragravity wave height for the fixed points in the nourished and non-nourished sites are shown. Section 5.3 examines the impact of the outer subtidal bar on dune erosion for March 2021, comparing the results with and without the outer subtidal bar and analysing the effect. Finally, Section 5.4 presents the XBeach results about different nourishment designs, discussing their influence on dune erosion and hydrodynamics.

## 5.1 March 2021

This section highlights the XBeach results from March 2021, focusing on dune erosion, hydrodynamics, and the drivers of dune erosion. March 2021 was selected to highlight because it represents the bathymetry before the occurrence of the actual storm sequence.

### 5.1.1 Dune erosion

In Figure 5.1, the first subplot shows the initial bathymetry and the other four subplots show the differences in bed level per storm (*zbstorm* - *zb0*) for the bathymetry of March 2021. The first subplot shows the entire bathymetry, and the other four subplots are zoomed in on the beach and dune area. The results for all bathymetric data from various dates are displayed in Appendix H.

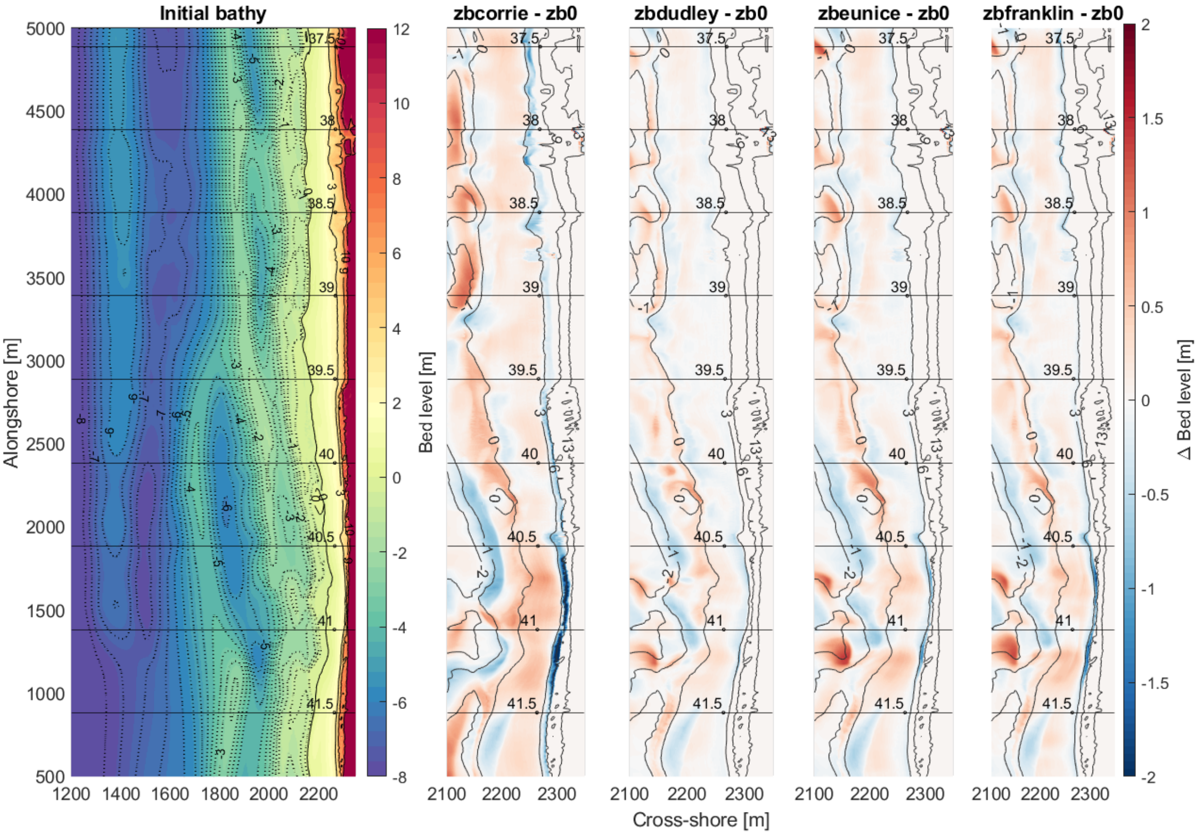

**Figure 5.1:** Initial bathymetry and modelled bed level difference per storm for March 2021. The horizontal lines present the beach poles.

From the bed level difference subplots in Figure 5.1 can be noticed that there is alongshore variation in dune erosion. A hotspot can be observed in the non-nourished site, between beach pole 40.5 and 41.5, and some smaller hotspots in the nourished site. In addition, there is also variation in the degree of dune erosion per storm. Storm Corrie has the biggest impact on dune erosion with an average volume change of 11m$^3$/m for the non-nourished site and 5m$^3$/m for the nourished site. Storm Franklin shows an average volume change of 2.8m$^3$/m for the non-nourished site and 0.6m$^3$/m for the nourished site, storm Eunice shows an average volume change of 1.3m$^3$/m for the non-nourished site and 0.15m$^3$/m for the nourished site and Dudley is negligible (Figure 5.2).

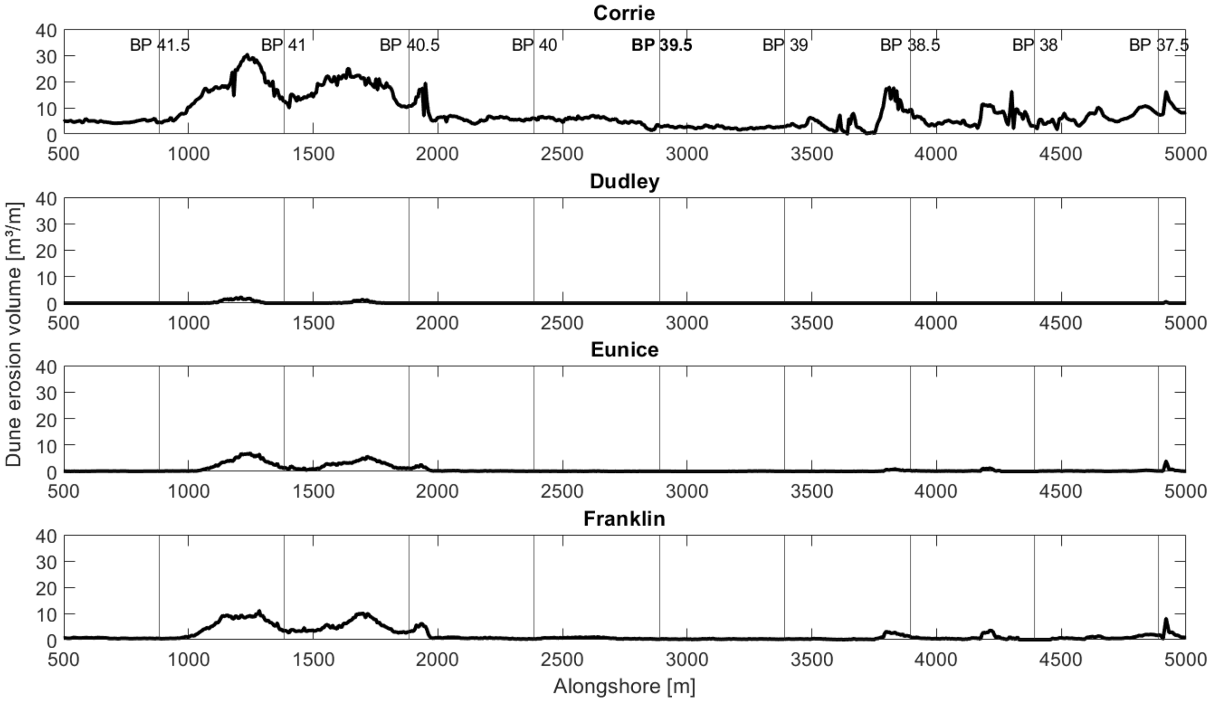

**Figure 5.2:** Alongshore dune erosion volume per storm. The vertical lines present the beach poles.

Figure 5.3 shows how the alongshore variation in dune erosion relates to the alongshore variation in the slope of the surf zone, inner surf zone, beach and dune. Several things are observed: The slope of the surf zone and inner surf zone shows a weak correlation with dune erosion. The slope of the surf zone increases when there is a deeper area in front of the shoreline. Although, this shows no causal relationship with the erosion hotspots. The inner surf zone slope shows a higher correlation, almost moderate. When the inner surf zone slope is shifted to the left, there might be a better correlation, especially for the hotspot in the non-nourished site. This lag might be a result of oblique incoming waves, which cause a shift in the erosion hotspot location. The beach slope shows a strong correlation with dune erosion. As the beach slope increases, the amount of dune erosion also increases which also indicates that when beach width decreases, dune erosion increases. Fore dune slope shows a moderate correlation with dune erosion.

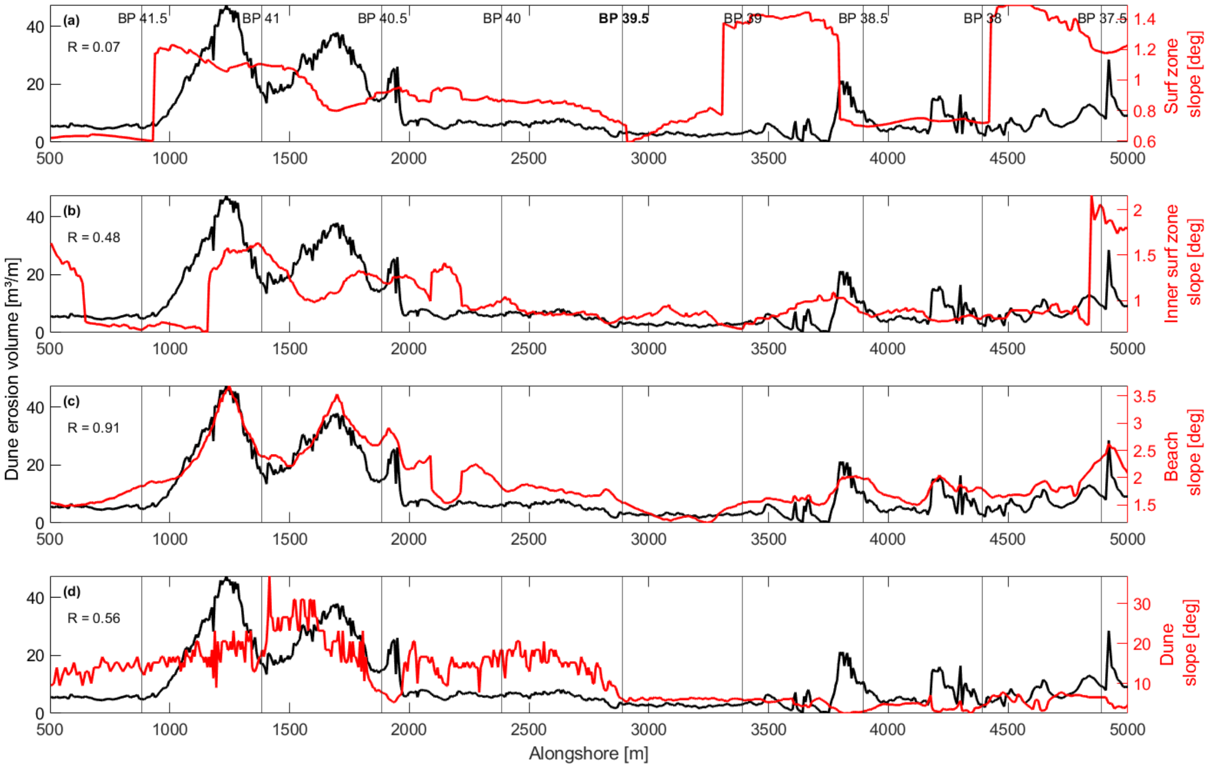

**Figure 5.3:** Dune erosion vs (a) surf zone slope; (b) inner surf zone slope; (c) beach slope; (d) dune slope. The R in the top left corner presents the correlation coefficient between the two lines.

### 5.1.2 Hydrodynamics

Figure 5.4 shows an overview of the short wave height at the peak of the storms. The short wave height decreases when the waves travel to the shore, indicating breaking waves. The wave height is roughly 3.5m offshore and 1.5 - 2m in the inner surf zone. The short waves are breaking continuously at the subtidal bars. The short waves are breaking more offshore in the nourished site (between x = 1400 and 1600) than in the non-nourished site because of the pronounced presence of the outer subtidal bar in the nourished site. In addition, the non-nourished site exhibits differences in wave breaking due to the deeper area (between x = 1750 and 2000m), compared to the deeper areas in the nourished site (between x = 1800 and 2000m). The deeper area in the non-nourished site is located in front of the erosion hotspot between beach pole 40.5 and 41.5 (Figure 5.1). The larger depth in the non-nourished site compared to the deeper areas in the nourished site causes short waves to break further landward. Differences between storms can be noted. The short wave height is highest during the peak of storm Corrie and lowest during storm Dudley.

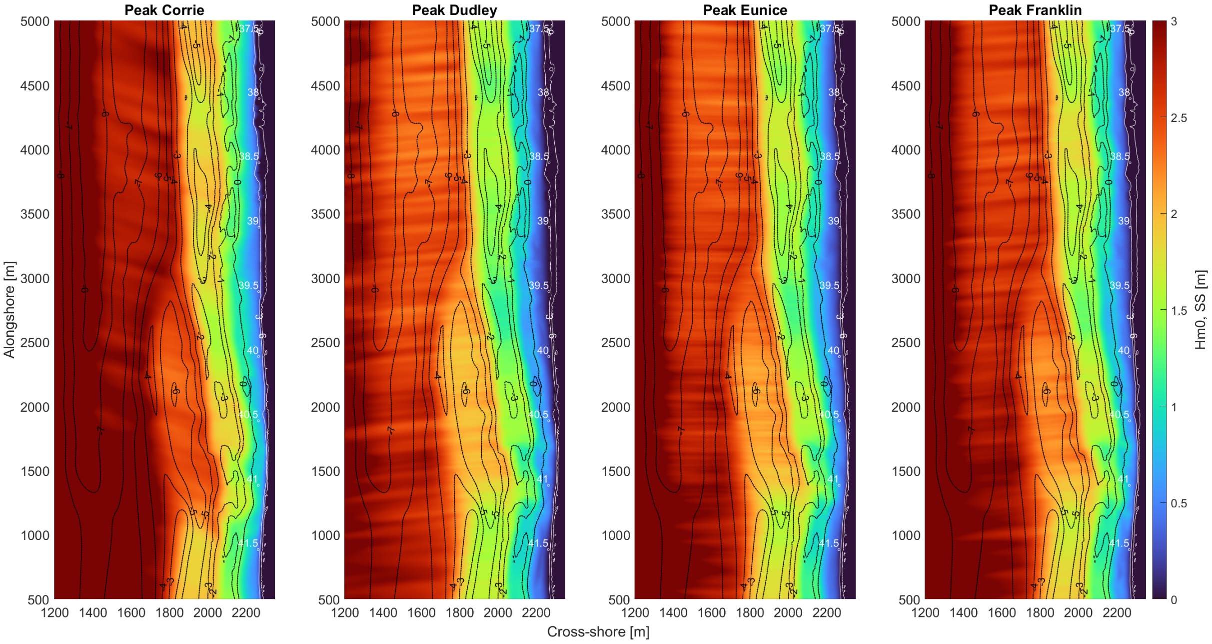

**Figure 5.4:** Short wave height at the peak of the storms.

Figure 5.5 shows an overview of the infragravity wave height at the peak of the storms. The infragravity wave height increases at the beach, varying alongshore. During the peak of storm Corrie, the infragravity wave height reaches roughly 1m and during the peak of the other storms, the infragravity wave height reaches roughly 0.5 - 0.8m at some locations. Sediment transport is most present in the north and in the hotspot in the south (black arrows). During the peak of storm Corrie the sediment is transported southwards and during the peak of the other storms, the sediment is transported in different directions, primarily northwards.

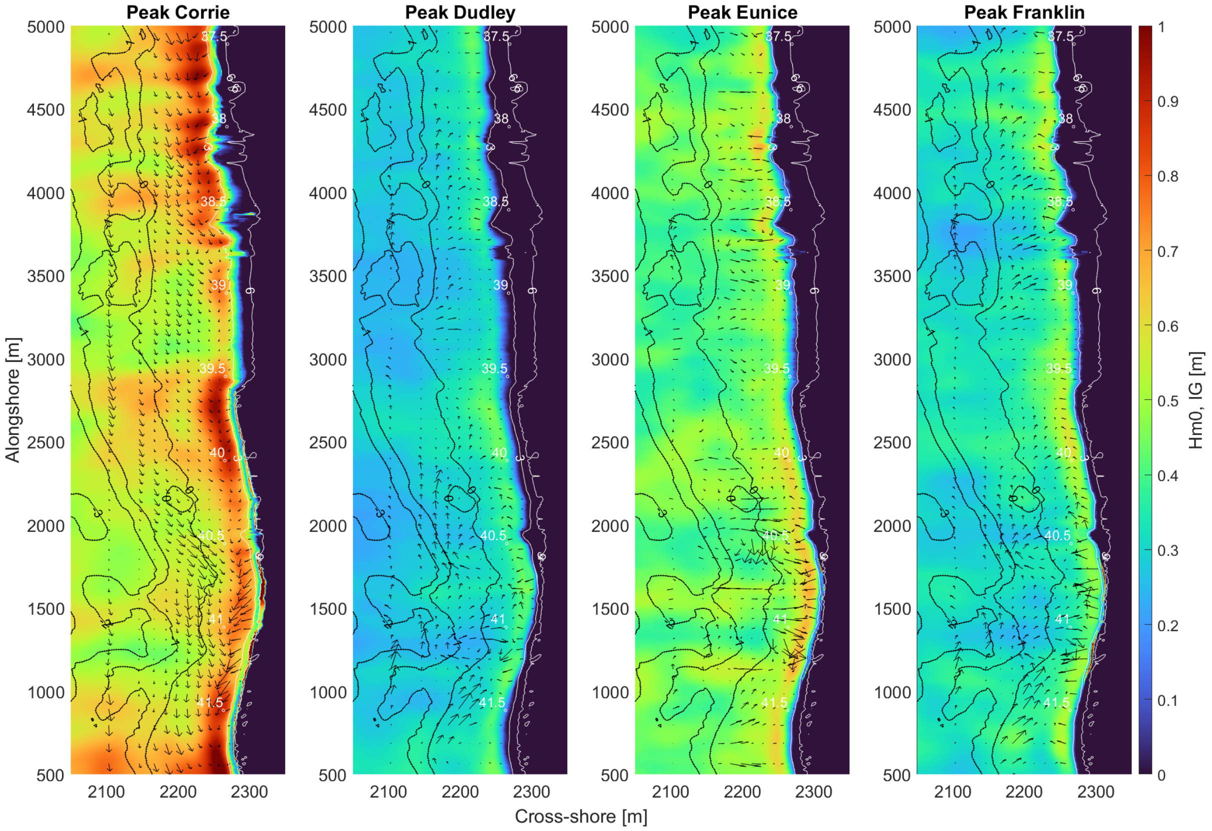

**Figure 5.5:** Infragravity wave height at the peak of the storms. The black arrows indicate the sediment transport.

Figure 5.6 shows the water level height at the fixed points. The seaward located points show water level height which reaches up to roughly 3 - 4m NAP during storm Corrie and 2 - 3m NAP during the other storms. Landward points run dry at low water elevations, revealing only the peak water levels during Corrie. The results include only 15-minute bursts when the point was continuously submerged, leading to these dry gaps. To avoid these gaps, the model output per second is also observed. This shows that the landward located points reach water level heights up to 4.8m NAP during storm Corrie, 3.5m NAP during storm Eunice and Franklin and the water level during Dudley is not noticeable. Some alongshore variation is noticed for the measured water level at the landward location. The points south of beach pole 39.5 (non-nourished site), remain submerged for a longer duration than the northern points.

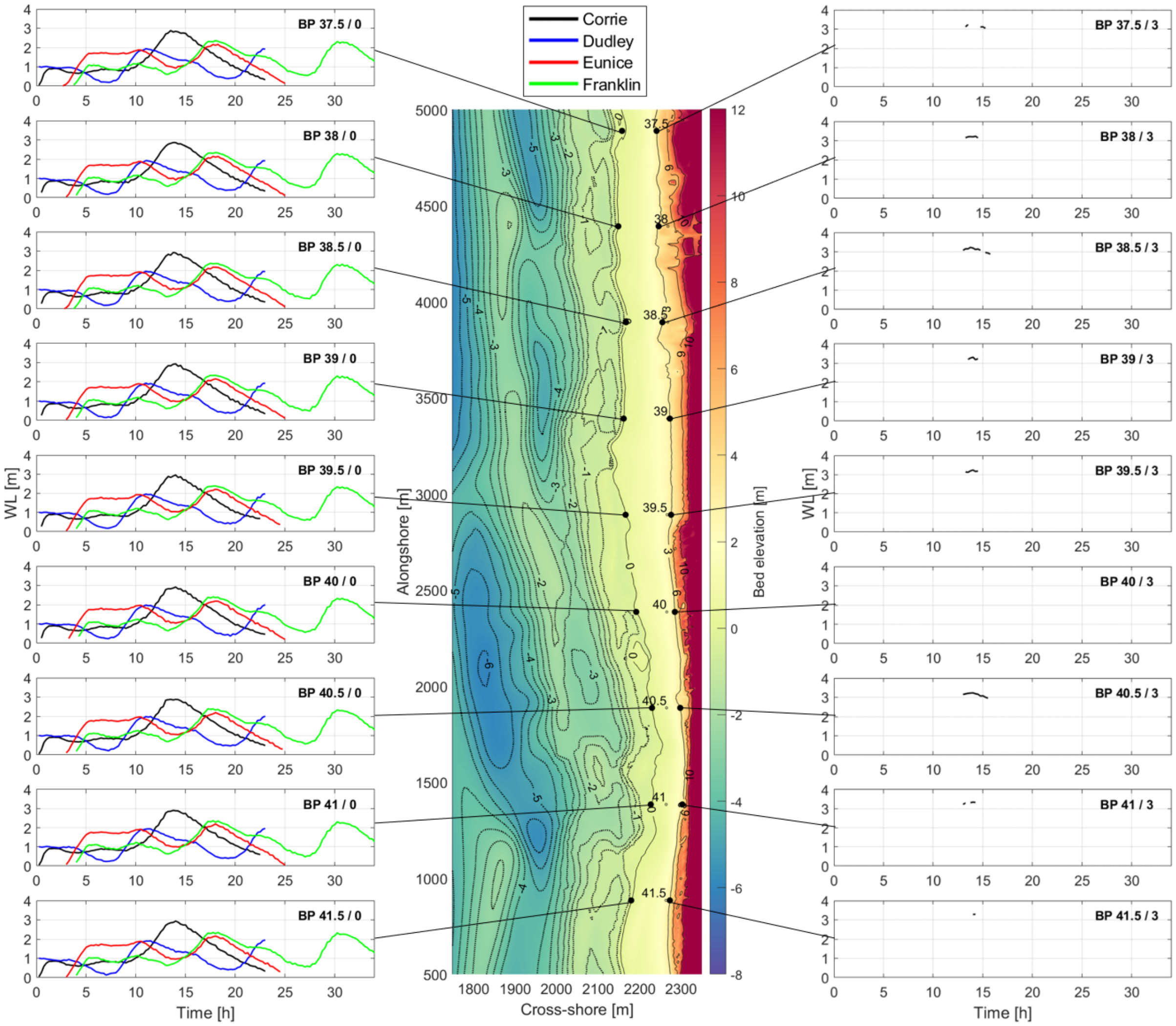

**Figure 5.6:** Water level height at the fixed points. The plot in the middle shows the location of the points and the surrounding subplots follow the order from North to South (top to bottom) and seaward to landward (left to right).

Figure 5.7 shows the short wave height at the fixed points. The seaward located points show short wave heights up to 1.5m during peak Corrie and roughly 1m during the other storms, whereas the wave heights at the landward located points do not exceed 0.5m or are not observable. This means that the short wave is dissipating at the beach. The short wave height is in both cases the highest during storm Corrie. For the seaward located points, the short wave height is higher at the northern beach poles, especially during storm Corrie. For the landward located points, the short wave is more pronounced at beach pole 38.5 and 40.5.

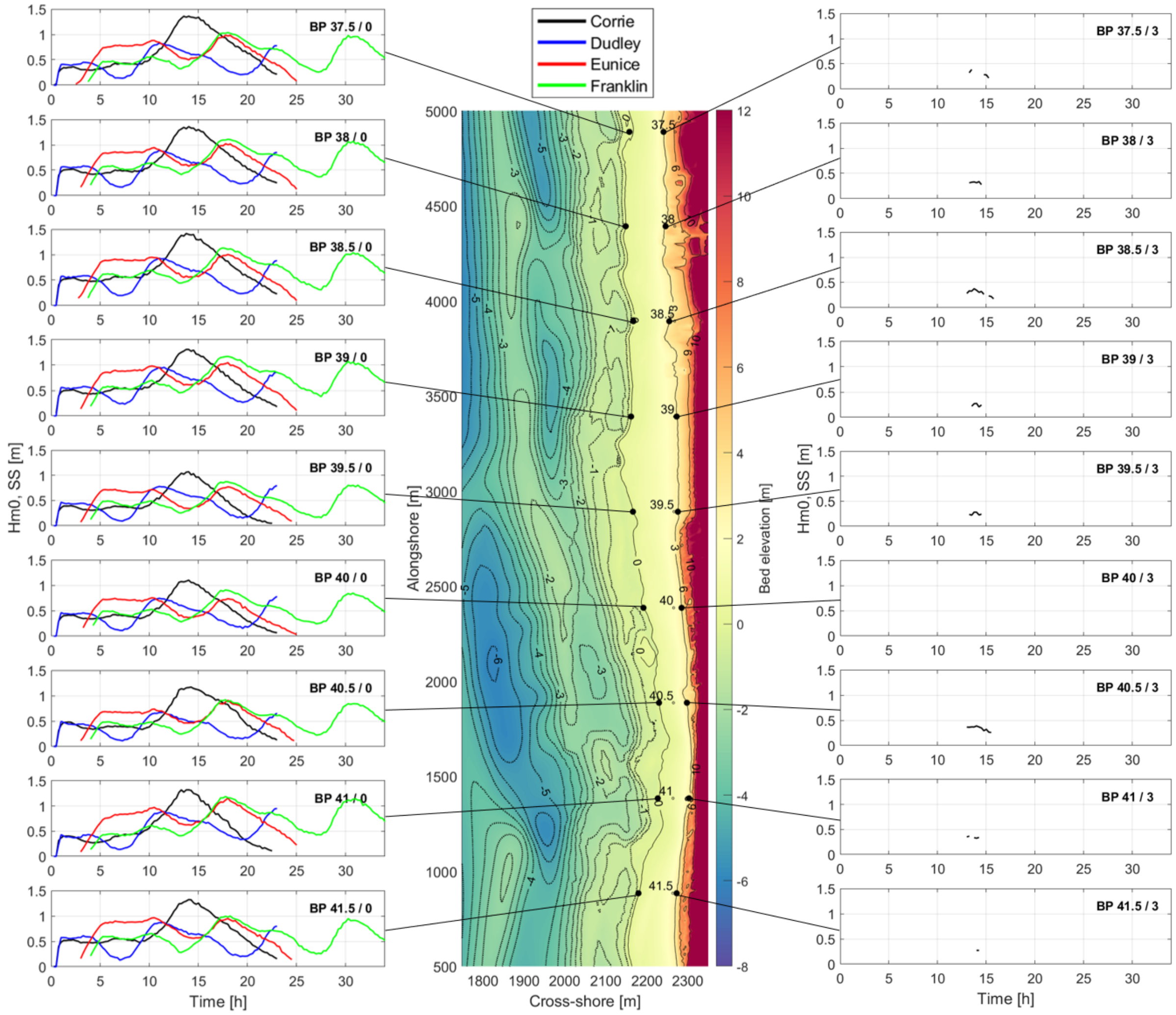

**Figure 5.7:** Short wave height at the fixed points. The plot in the middle shows the location of the points and the surrounding subplots follow the order from North to South (top to bottom) and seaward to landward (left to right).

Figure 5.8 shows the infragravity wave height at the fixed points. The seaward located points show infragravity wave heights in order of 0.5 - 1m during storm Corrie and 0.25 - 0.5m during the other storms. The landward located points show also infragravity wave heights in order of 0.5 - 1 during storm Corrie, while the infragravity wave height during the other storm is not noticeable. The height of the infragravity wave varies per beach pole. At the beach pole level where erosion takes place (Figure 5.1), there is an increased infragravity wave height. In addition, while the infragravity wave height at seaward points shows lower levels than the short wave height, at landward points, it exhibits higher levels than the short wave height (Figure 5.7). This is because, on gently sloping beaches like Egmond, infragravity waves are relatively large compared to short waves, leading to higher harmonics and wave steepening.

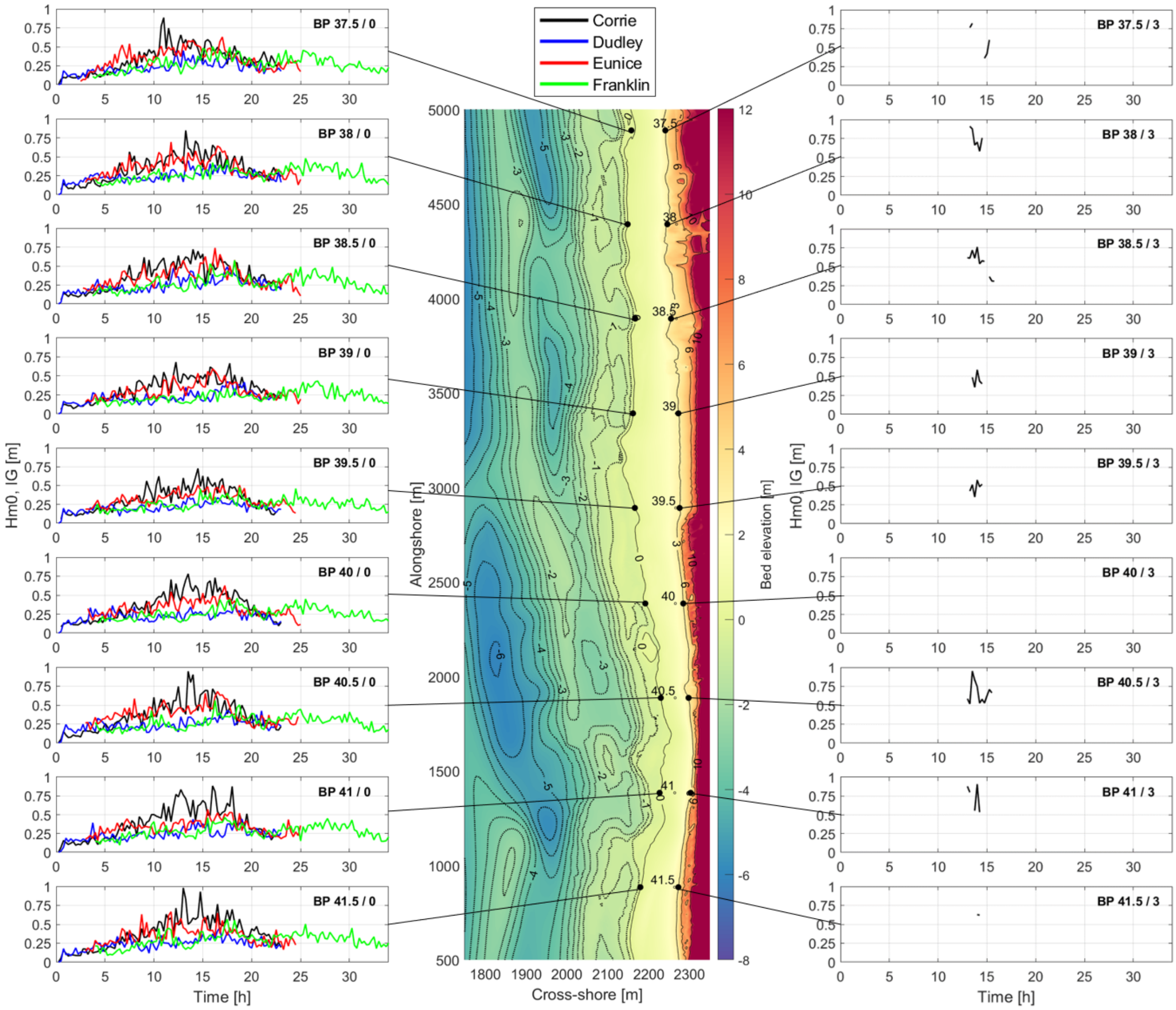

**Figure 5.8:** Infragravity wave height at the fixed points. The plot in the middle shows the location of the points and the surrounding subplots follow the order from North to South (top to bottom) and seaward to landward (left to right).

Figure 5.9 shows the cross-shore wave evolution of the short and infragravity wave height at four alongshore located fixed points during the peak of the storm. From the left subplots can be noticed that the short wave height is decreasing when moving onshore; breaking repeatedly on the subtidal bars. The short wave height in the nourished site (purple and yellow lines) is lower offshore than the short wave height in the non-nourished site (blue and orange lines) because of the outer subtidal bar. The waves in the non-nourished site are breaking earlier in the cross-shore direction due to the presence of the middle subtidal bar but remain for a longer duration compared to the wave height in the nourished site due to the presence of the deeper area in the non-nourished site and the location of the shoreline of the nourished site which is extended more seawards compared to the non-nourished shoreline. The short wave height shows the same pattern and level during the different storms. Only Corrie shows higher elevations.

From the right subplots can be noticed that the infragravity wave height increases when the wave reaches shallow water. This is caused by a transfer of energy from the shorter-period waves to the longer-period infragravity waves when waves break. Overall can be noticed that the infragravity wave height shows the highest values in the non-nourished site. The infragravity wave height reaches roughly 1m at the beach on the most southern point and 0.5 - 0.7m at the other points during storm Corrie. The infragravity wave height at the most northern points and the second south point reaches roughly 0.75m. As previously mentioned, infragravity wave heights exceed those of short waves in the beach zone.

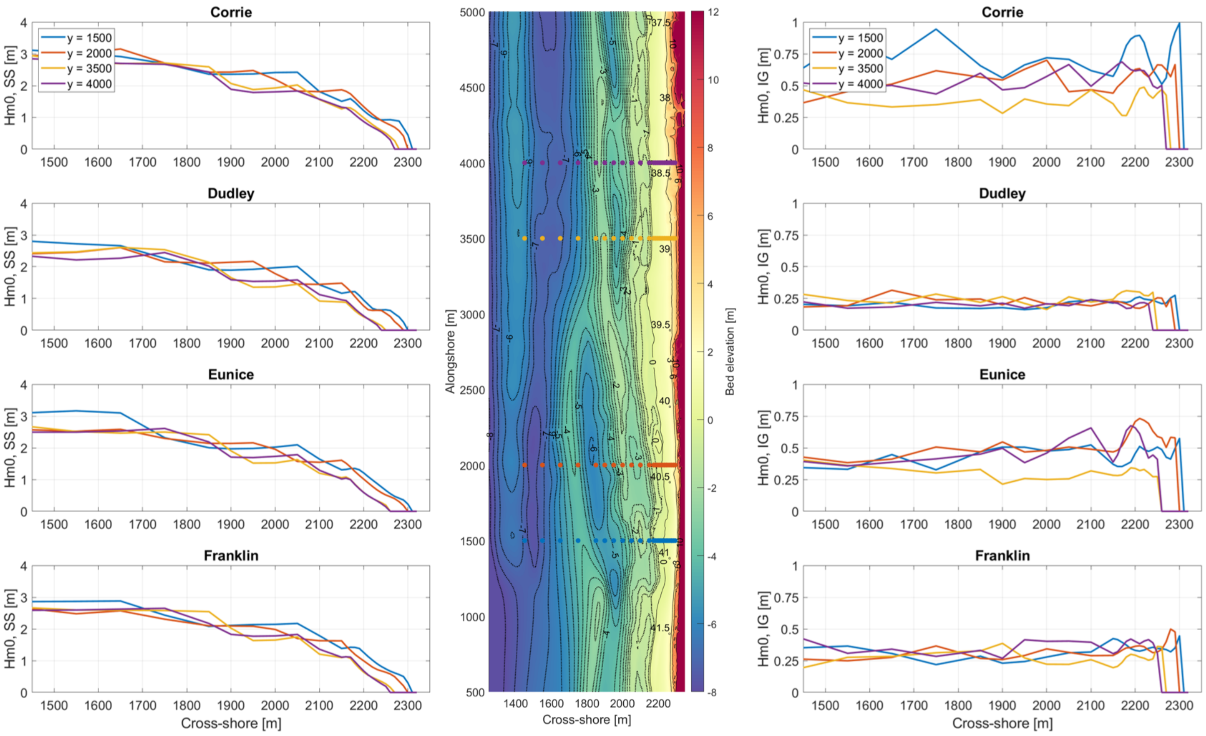

**Figure 5.9:** Cross-shore wave evolution during peak storms. The plot in the middle shows the location of the points and the surrounding subplots show the short wave and infragravity wave height evolution per storm in cross-shore direction at four different alongshore locations. The surrounding subplots follow the order from North to South (top to bottom) and seaward to landward (left to right).

## 5.2 Comparing dates and sites

The previous section highlights only the XBeach result of the March 2021 bathymetry. This section summarizes XBeach results for the six bathymetries. Alongshore variation in dune erosion, nourished and non-nourished site differences and differences by storm are shown. Furthermore, differences in infragravity wave height on the nourished and non-nourished sites are discussed.

### 5.2.1 Dune erosion

Figure 5.10 shows the alongshore dune erosion volume per bathymetry date. Several things are observed: XBeach predicts dune erosion mainly south of beach pole 39.5 (non-nourished site). Here the amount varies from date to date (see also the Figures in Appendix H). The location of dune erosion in the nourished site is about the same; the erosion hotspots around beach pole 38 and 38.5. The location of dune erosion in the non-nourished site differs per date. XBeach predicts dune erosion between beach pole 40.5 and 41.5 every date (erosion hotspot). Only for March 2020, there is also a lot of erosion northwards of this hotspot and for March 2022 southwards of this hotspot. Between beach pole 39.75 and 38.75, there is hardly any erosion.

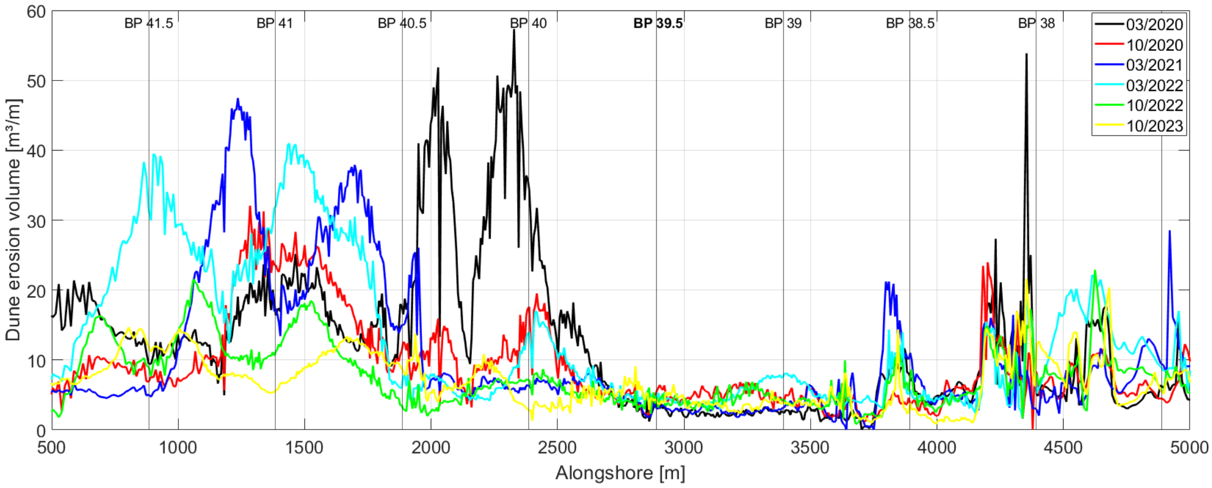

**Figure 5.10:** Alongshore dune erosion volume per bathymetry date.

Figure 5.11 shows the average dune erosion volume for the various bathymetric dates for the nourished and non-nourished site. XBeach predicts more dune erosion for the non-nourished site than for the nourished site across all dates. The dune erosion volume ranges from about 7.8 to 18.5m$^3$/m for the non-nourished site and 5.0 to 7.2m$^3$/m for the nourished site. March 2020 shows the largest magnitude of average dune erosion volume for the non-nourished site and March 2022 for the nourished site. It is important to note that the average dune erosion volume for the non-nourished site is almost half for October 2022 and 2023 compared to the other dates. This will be discussed further in Chapter 6.

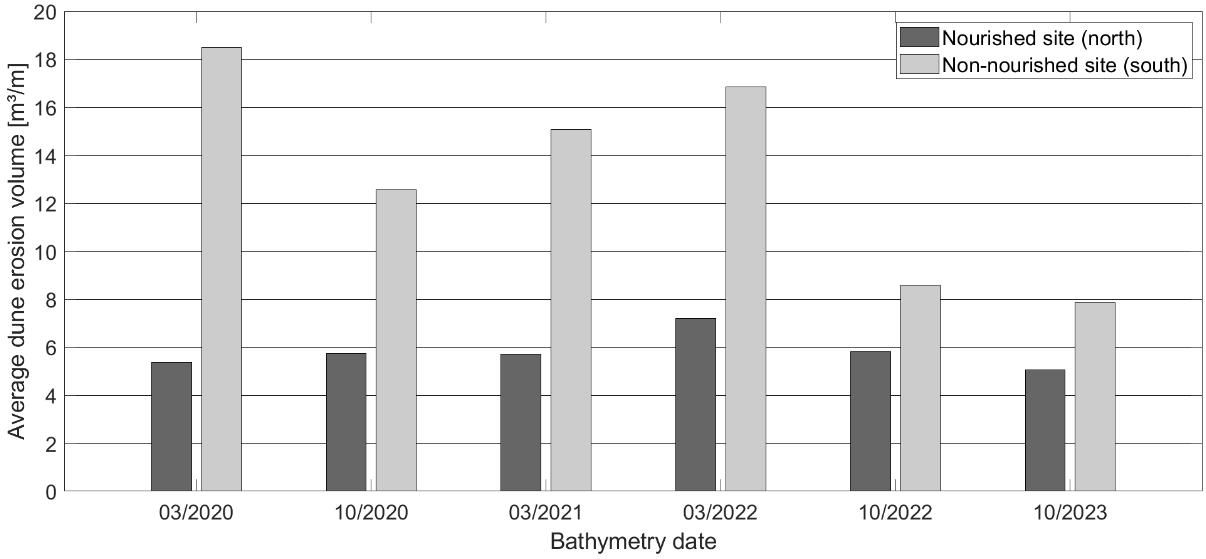

**Figure 5.11:** Average dune erosion volume for the nourished and non-nourished site per bathymetry date.

Figure 5.12 shows the differences between the nourished and non-nourished site of Egmond per storm. Storm Corrie has the biggest impact on dune erosion volume followed by Franklin, Eunice and Dudley across all bathymetry dates.

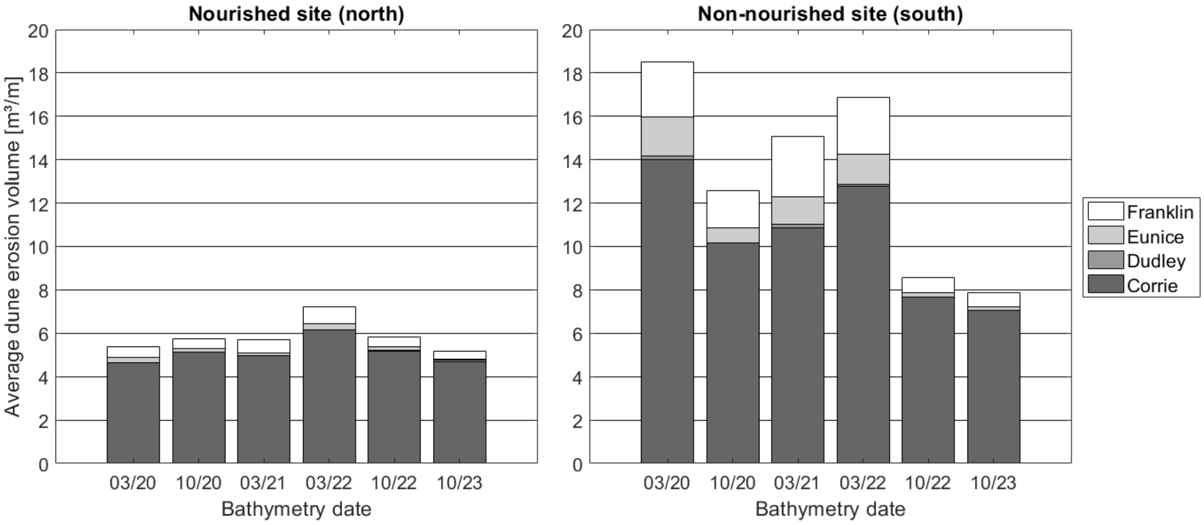

**Figure 5.12:** Average dune erosion volume for the nourished and non-nourished site per bathymetry date and storm.

Table 5.1 presents the correlations between alongshore dune erosion volume and surf zone, inner surf zone, beach, and dune slope for the different bathymetry dates. Overall, October 2022 and 2023 exhibit the lowest scores in almost all correlations. The correlation between surf zone slope and dune erosion appears weak for every date except October 2023. Furthermore, the correlation between surf zone slope and dune erosion remains consistently weak across all dates. Beach slope and dune erosion demonstrate a strong correlation for March 2020, March 2021 and March 2022, with a moderate correlation observed for October 2020, October 2022 and 2023. Dune slope and dune erosion exhibit a strong correlation for March 2020 and 2022, a moderate correlation for October 2020, March 2021 and October 2022 and a weak correlation for March 2023.

**Table 5.1:** Correlation coefficient between alongshore dune erosion and slope of different zones.

| **Bathymetry** | **Surf zone Slope** | **Inner surf zone Slope** | **Beach Slope** | **Dune slope** |
|---|---|---|---|---|
| March 2020 | 0 | 0.13 | 0.84 | 0.83 |
| October 2020 | 0.20 | 0.27 | 0.78 | 0.51 |
| March 2021 | 0.07 | 0.48 | 0.91 | 0.56 |
| March 2022 | -0.33 | -0.16 | 0.83 | 0.88 |
| October 2022 | -0.18 | 0.05 | 0.59 | 0.60 |
| October 2023 | 0.53 | 0.07 | 0.69 | 0.29 |

### 5.2.2 Infragravity wave height

Figure 5.13 shows scatter plots of the infragravity wave height modelled at the fixed points on NAP 0m, north (nourished) and south (non-nourished) of beach pole 39.5 (See location fixed points in Figure 5.8, this varies per bathymetry). It has been noted that with increasing infragravity wave height, the magnitude of these waves tends to be higher at points in the non-nourished site compared to points in the nourished site during each storm and date. This is an important fact as infragravity wave height influences dune erosion.

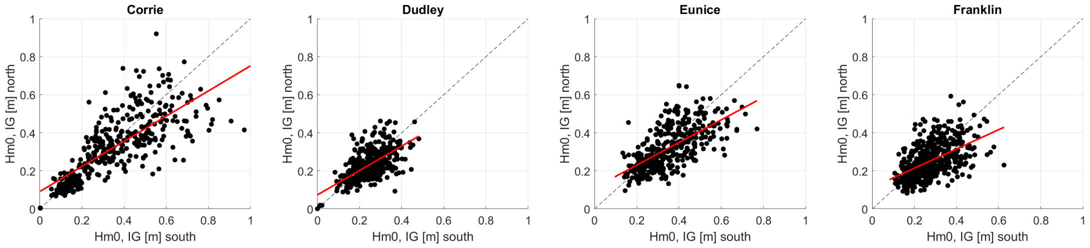

**(a)** March 2020

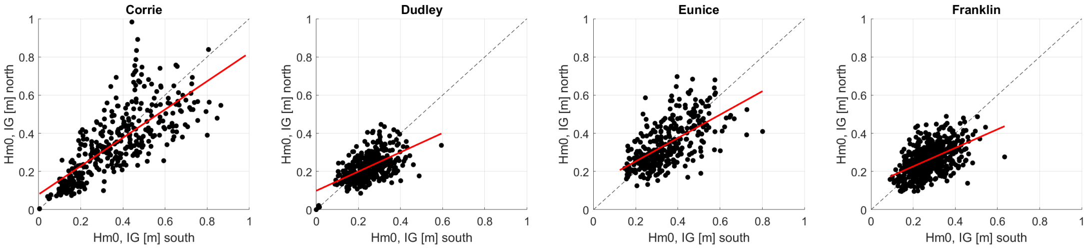

**(b)** October 2020

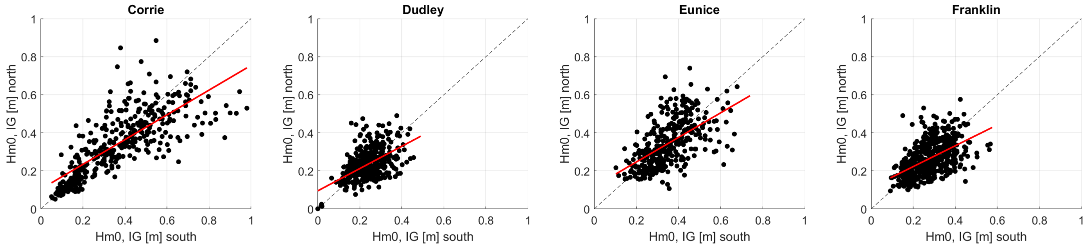

**(c)** March 2021

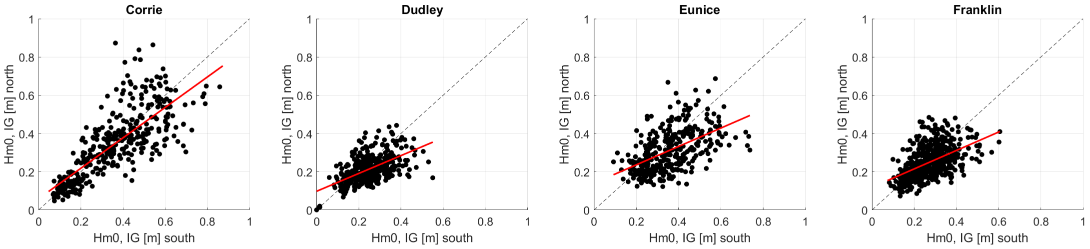

**(d)** March 2022

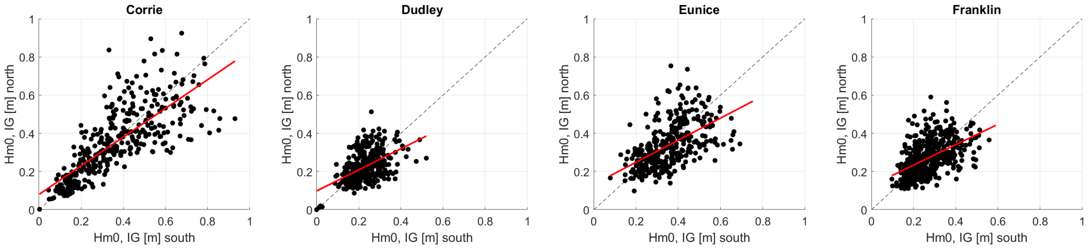

**(e)** October 2022

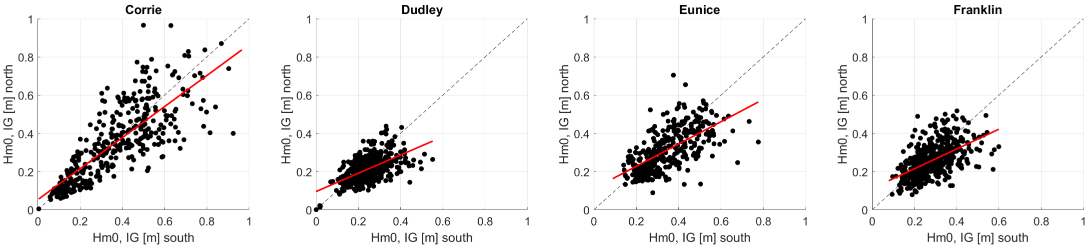

**(f)** October 2023

**Figure 5.13:** Scatter plot of infragravity wave height ($H_{m0,IG}$) modelled at the fixed points, located at NAP 0m, north and south of beach pole 39.5. The dashed line indicates a perfect 1:1 relationship; the solid red line represents the linear regression fit.

## 5.3 March 2021 without outer subtidal bar

The previous two sections describe the XBeach results for March 2021 and give a summary of the results for all the bathymetry dates. A distinction has been made between the nourished and non-nourished site of Egmond. Before moving on to the section with the nourishment designs, the results are presented with the simulations from March 2021 where the outer subtidal bar is removed to assess the effect of the bar on dune erosion. See Figure 3.8 for the bathymetry of March 2021 without outer subtidal bar.

### 5.3.1 Dune erosion

Figure 5.14 shows the average dune erosion volume for the nourished and non-nourished site with the bathymetry of March 2021 with and without the outer subtidal bar. The average dune erosion volume for the result with the outer subtidal bar is roughly 5.7m$^3$/m for the nourished site and 15m$^3$/m for the non-nourished site. The average dune erosion volume for the result without the outer subtidal bar is roughly 6.7m$^3$/m for the nourished site and 15.9m$^3$/m for the non-nourished site. Dune erosion is in both cases more pronounced for the bathymetry without the outer subtidal bar indicating the effect of the outer subtidal bar.

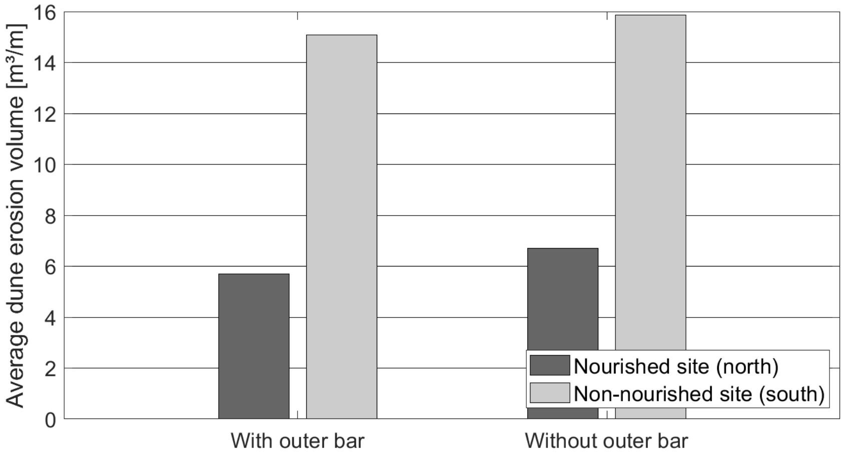

**Figure 5.14:** Average dune erosion volume for a nourished and non-nourished site for bathymetry March 2021 with and without outer subtidal bar.

### 5.3.2 Hydrodynamics

Figure 5.15 shows an overview of the short wave height at the peak of the storms when the outer subtidal bar is removed. Compared to the height of the short waves in the presence of the outer subtidal bar (Figure 5.4), their breaking point is less offshore due to the absence of the outer subtidal bar. The short wave height shows the same evolution as the short wave height with the presence of an outer subtidal bar; the short wave height decreases when the waves travel to the shore but the breakpoint is more offshore in the non-nourished site than the nourished site due to middle subtidal bar. The short wave height shows an increase of 10 to 20 cm around the NAP -4m contour line in the deeper areas at the nourished site (between x = 1850 and 2000m) and deeper area in the non-nourished site (between x = 1700 and 1900m) and up to 10cm on the beach in the absence of an outer subtidal bar (Figure 5.16). This could be attributed to the larger incoming waves, which extend the duration of high waves. On the other hand, the short wave height shows a decrease of up to 10cm in the deep area in the south (between x = 1750 and 2000m) in the absence of an outer subtidal bar. The reduction in short wave height in deeper parts can be attributed to larger waves reaching the bottom faster, thereby transforming and breaking. These disparities in short-wave heights are particularly noticeable during storms such as Corrie, Eunice, and Franklin.

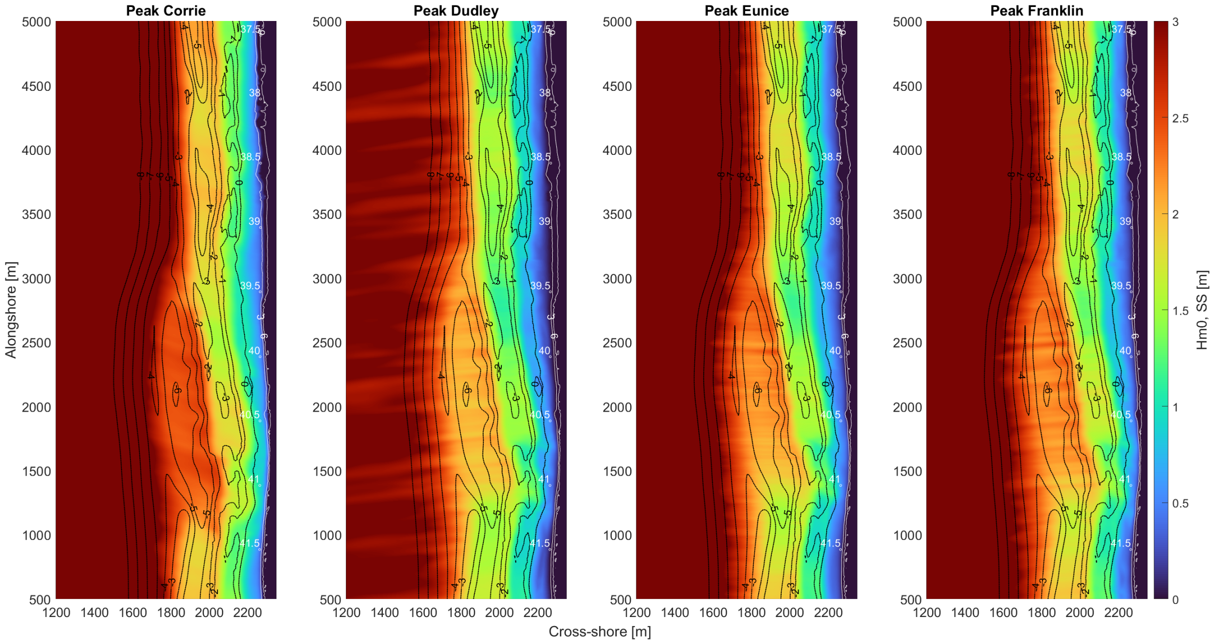

**Figure 5.15:** Short wave height at the peak of the storms for March 2021 without outer subtidal bar.

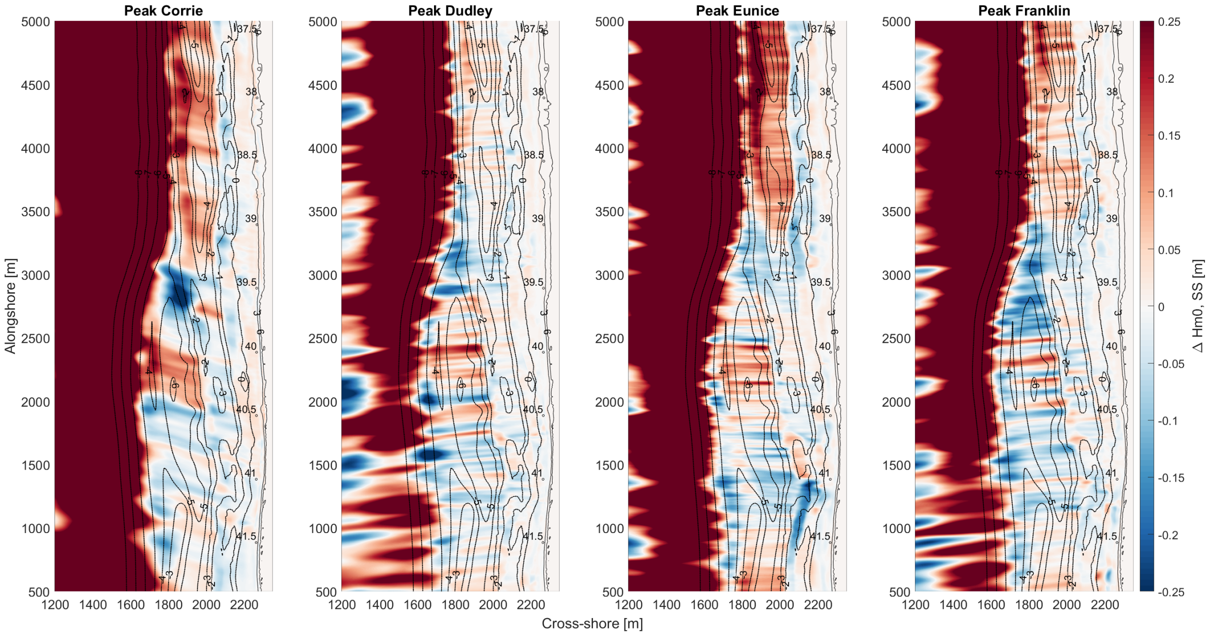

**Figure 5.16:** Difference in short wave height at the peak of the storms for March 2021 without outer subtidal bar (Figure 5.4 - Figure 5.15).

Figure 5.17 shows an overview of the infragravity wave height at the peak of the storms in the absence of an outer subtidal bar. The infragravity wave height experiences an increase of up to 15 cm at the erosion hotspots in the absence of an outer subtidal bar, compared to a situation where the outer subtidal bar is present (Figure 5.18). This might be attributed to the increase in short wave height when the outer subtidal bar is removed (Figure 5.16). The differences in infragravity wave height between the results with vs without outer subtidal bar are most present during storm Corrie, Eunice and Franklin.

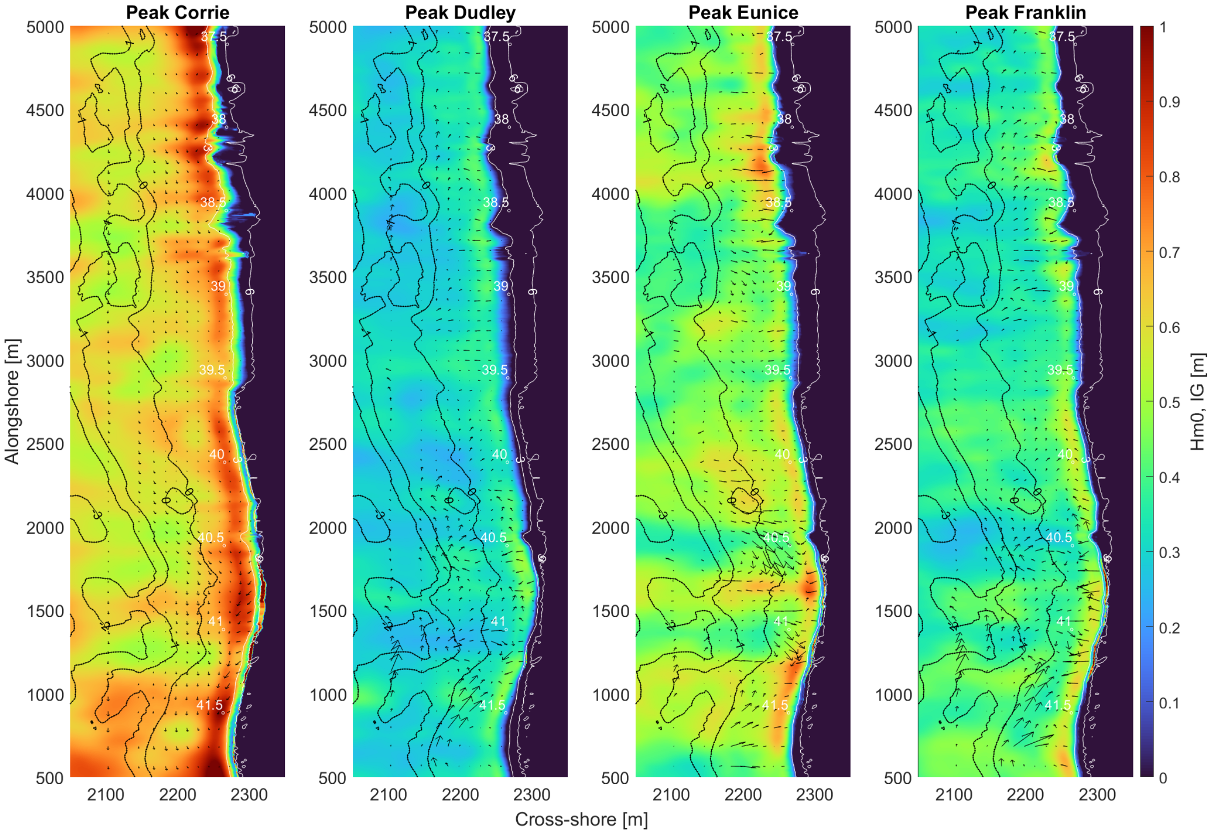

**Figure 5.17:** Infragravity wave height at the peak of the storms for March 2021 without outer subtidal bar.

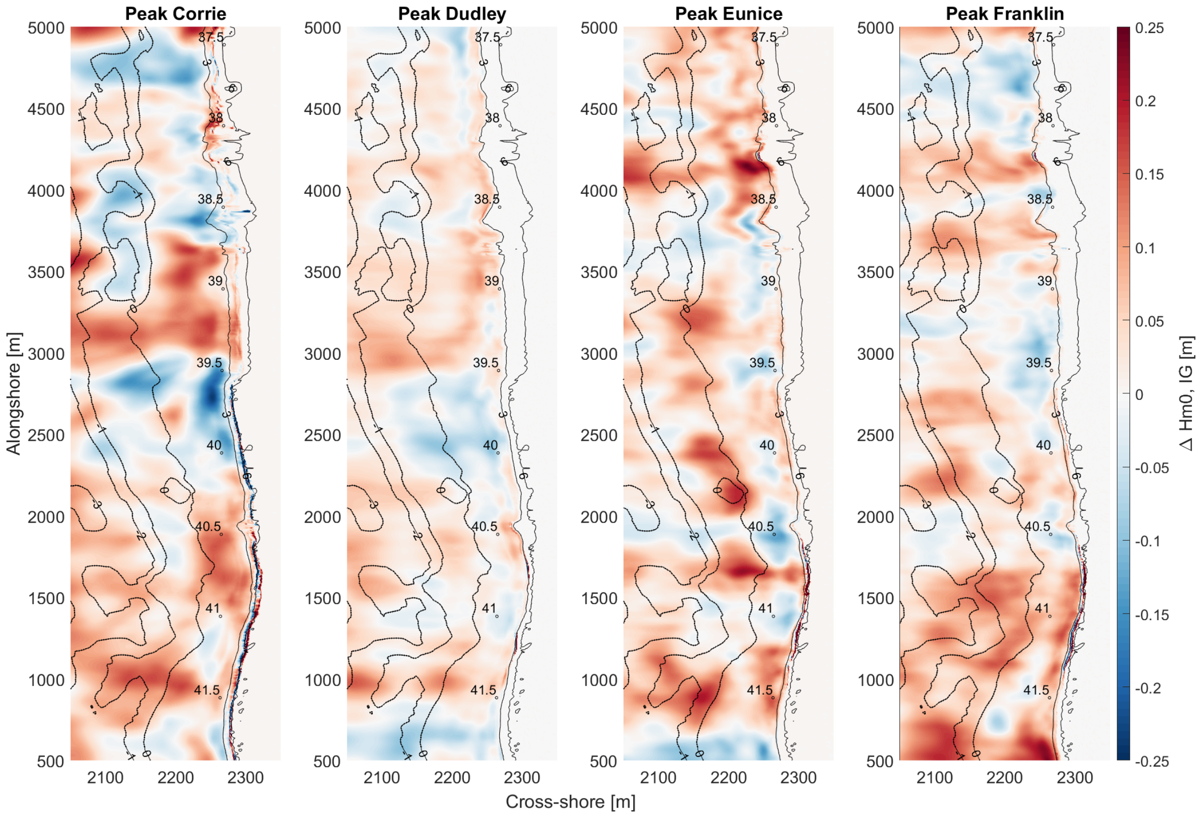

**Figure 5.18:** Difference in infragravity wave height at the peak of the storms for March 2021 without outer subtidal bar (Figure 5.5 - Figure 5.17).

## 5.4 Comparing nourishment designs

This section presents the XBeach results for the nourishment designs, illustrating dune erosion volumes and hydrodynamics. The result shed light on the impact of these designs on dune erosion and nearshore hydrodynamics.

### 5.4.1 Dune erosion

Figure 5.19 shows the average dune erosion volume per nourishment design for the northern and southern site of Egmond. The initial bars show the result with the bathymetry of October 2023. The bars right of the initial bars are the result of the bathymetry of October 2023 with the specific nourishment design, described on the x-axis. See for an overview of the nourishment designs Table 3.2 and impressions Appendix E. What stands out is that the shoreface nourishments which are implemented in the northern site have almost no effect on the amount of dune erosion in this site. When the shoreface nourishment is extended to the south (north and south design), it has a small effect on the amount of dune erosion to the north and the south; it increases for the northern site and decreases for the southern site. Beach nourishment has the greatest effect on dune erosion. The amount of dune erosion in the northern site becomes even negative. This means that the model predicts accretion of the dune in this site (NAP +3 - 6m). This is caused by the model pushing the top of the beach nourishment landward, adding volume to the foredune (Figure 5.20).

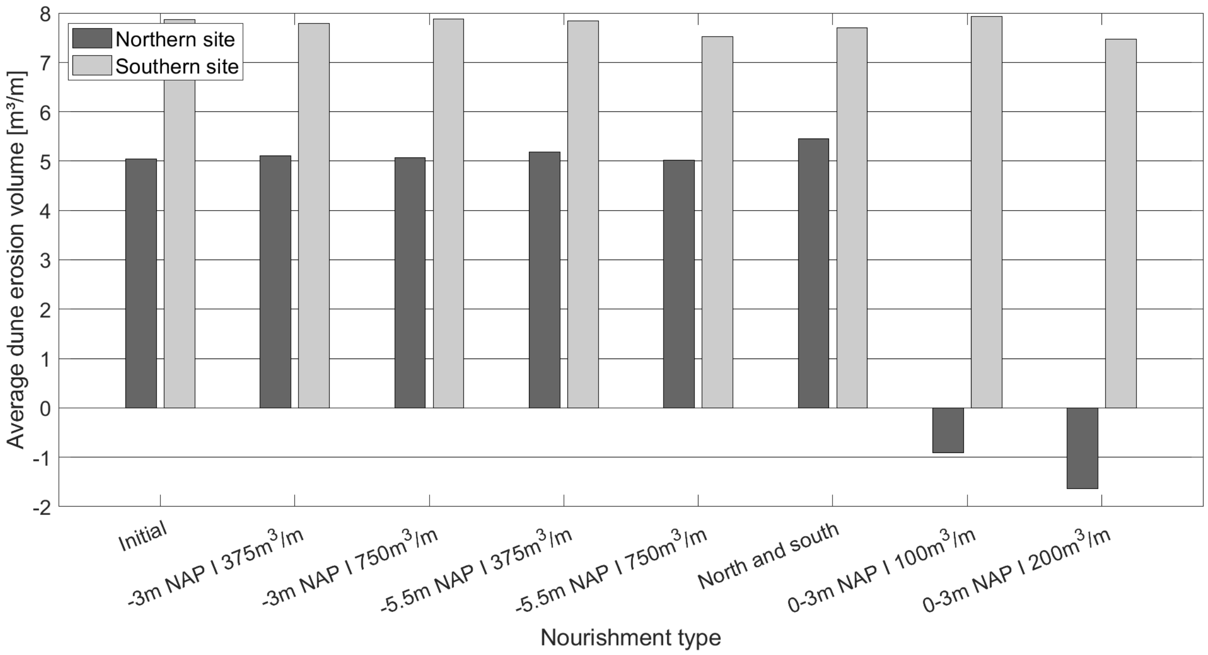

**Figure 5.19:** Average dune erosion volume for the northern and southern site and different nourishment designs.

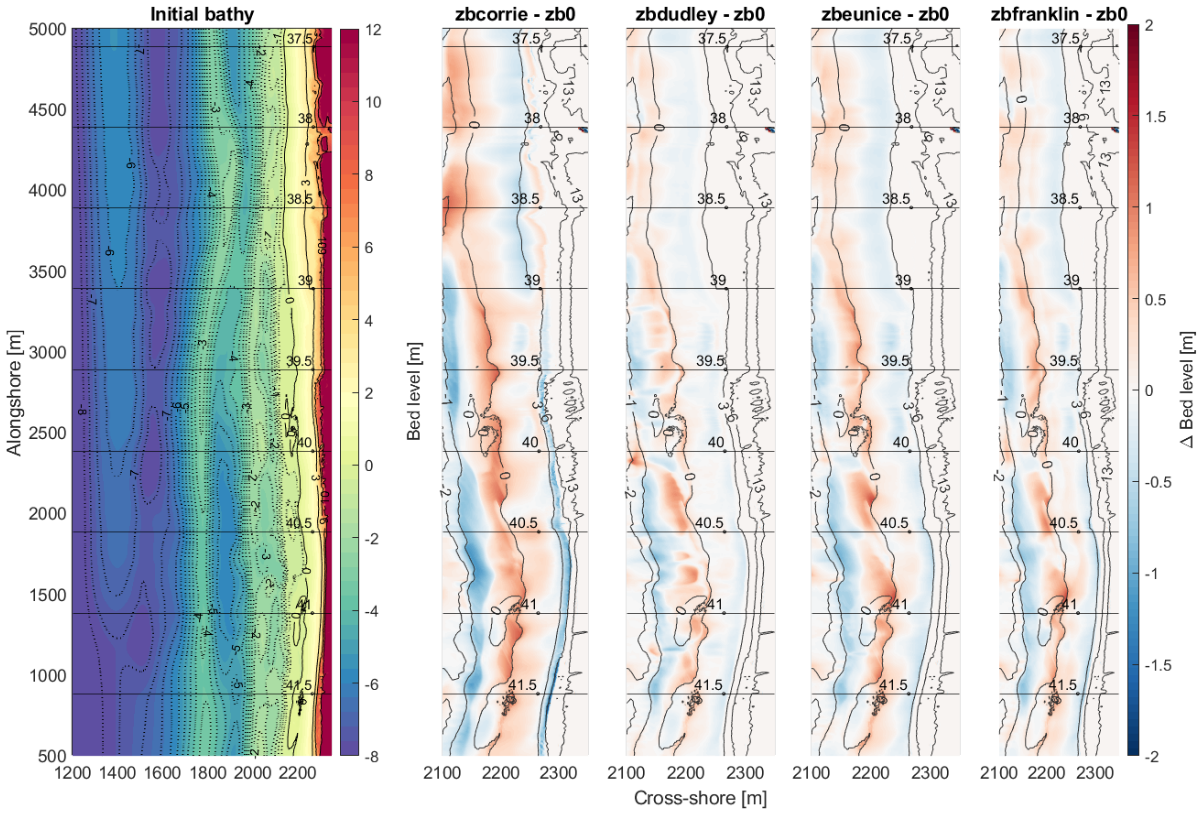

**Figure 5.20:** Initial bathymetry and modelled bed level difference per storm for March 2023 + beach nourishment between 0 - 3m NAP with a volume of 100m$^3$/m. For the second subplot, zbcorrie - zb0, the landward movement of the beach nourishment is observed.

### 5.4.2 Hydrodynamics

The hydrodynamics during shoreface nourishment in the north, the shoreface nourishment in the north/south and beach nourishment are displayed below to give an overview of the relevant hydrodynamics processes taking place. Generally, the shoreface nourishment mainly affects the wave breaking point, which has little effect on dune erosion (Figure 5.19). First, the short and infragravity wave height at the peak of the storms for March 2023 is shown to compare these maps with the nourishment maps (Figure 5.21 and 5.22).

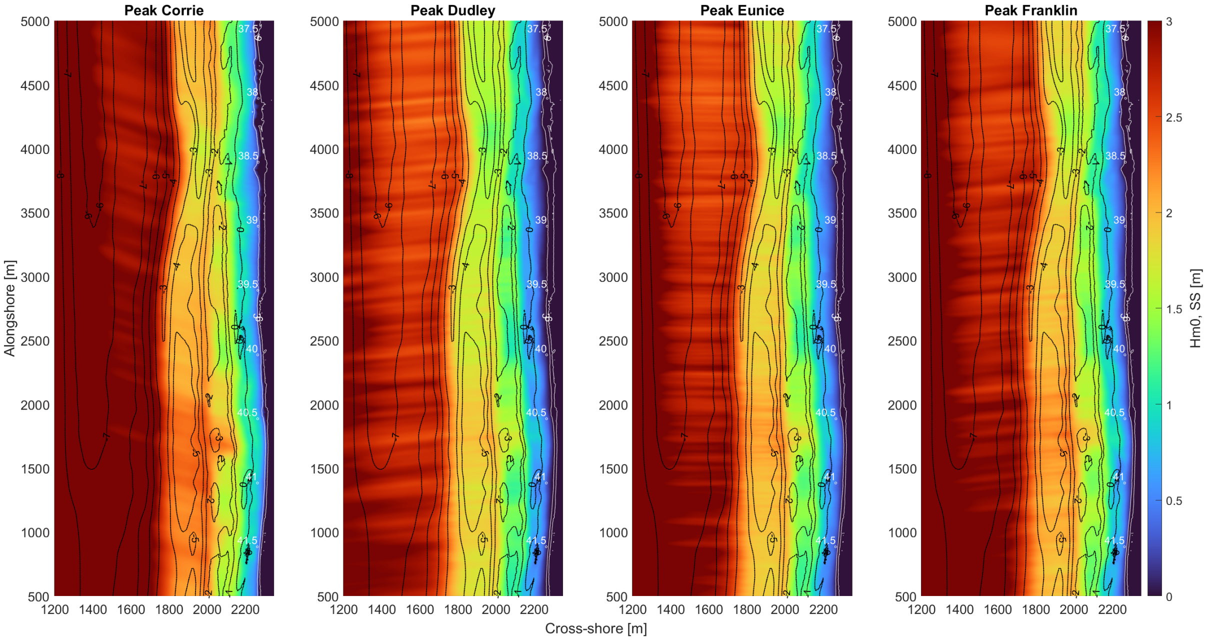

**Figure 5.21:** Short wave height at the peak of the storms for March 2023 without nourishment design.

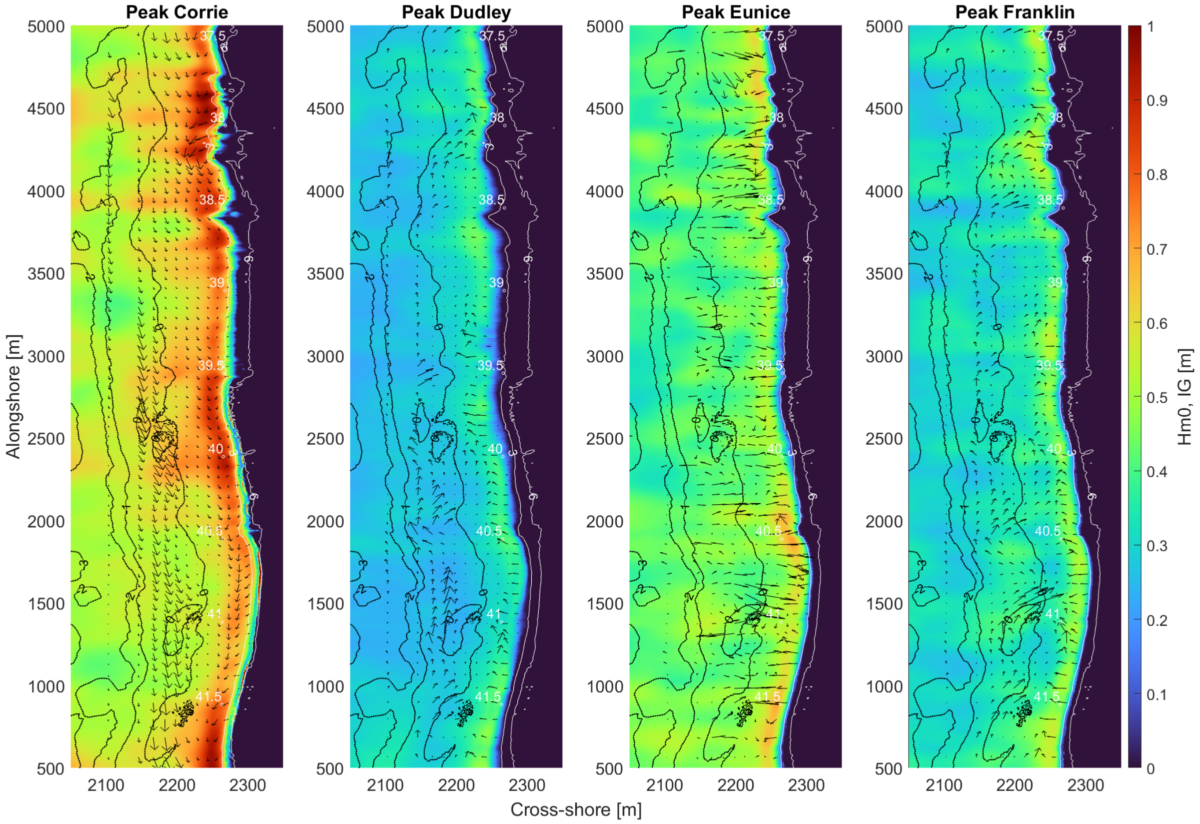

**Figure 5.22:** Infragravity wave height at the peak of the storms for March 2023 without nourishment design. The black arrows indicate the sediment transport.

Figure 5.23 shows an overview of the short wave height at the peak of the storms for March 2023 with shoreface nourishment in the northern site at NAP -3m with a volume of 375m$^3$/m. Compared to Figure 5.21, it is observable that the waves break more offshore due to the shallow area created by the shoreface nourishment. Moreover, the differences are minimal.

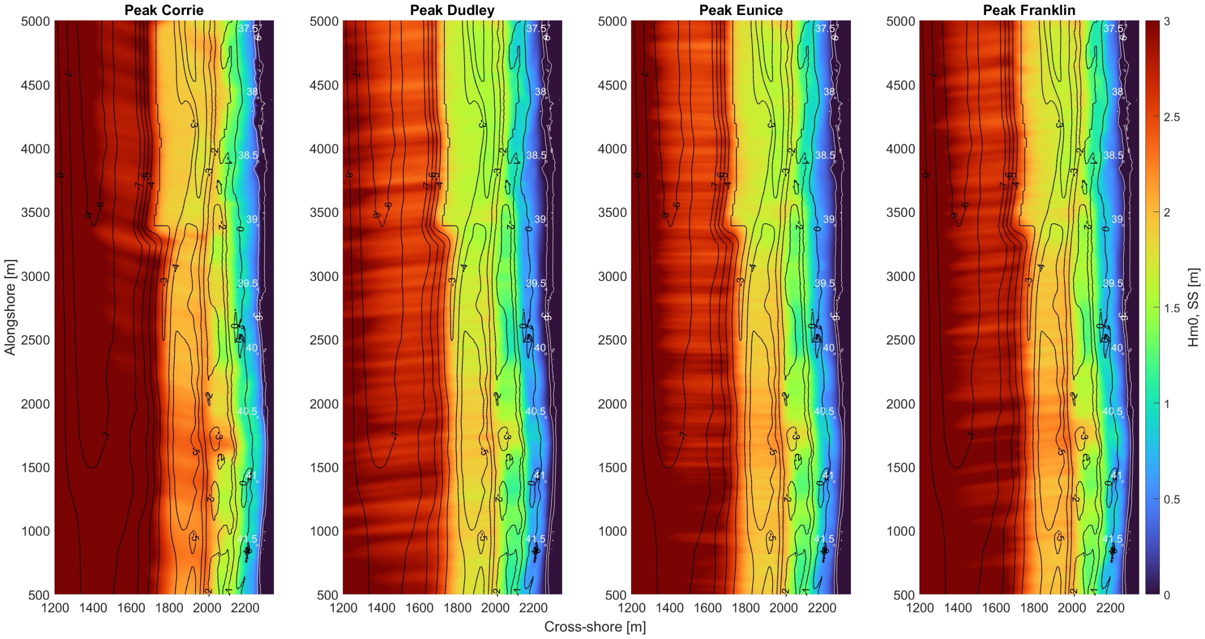

**Figure 5.23:** Short wave height at the peak of the storms for March 2023 with shoreface nourishment in the northern site at -3m NAP with a volume of 375m$^3$/m.

Figure 5.24 shows an overview of the short wave height at the peak of the storms for March 2023 with shoreface nourishment in the northern and southern site at NAP -5.5m with a volume of 375m$^3$/m. Compared to Figure 5.21, the waves are breaking more offshore in the northern and southern site because the width of the outer subtidal bar in the north is increased and the shoreface nourishment in the south is acting like a breaker bar. An important observation is that the short wave height in the southern deeper area (between x = 1750 and 2000) is higher when there is a breaker bar in the south compared to when there is not. Conversely, the short wave height more landwards of this deeper area is lower (along the -2m contour line).

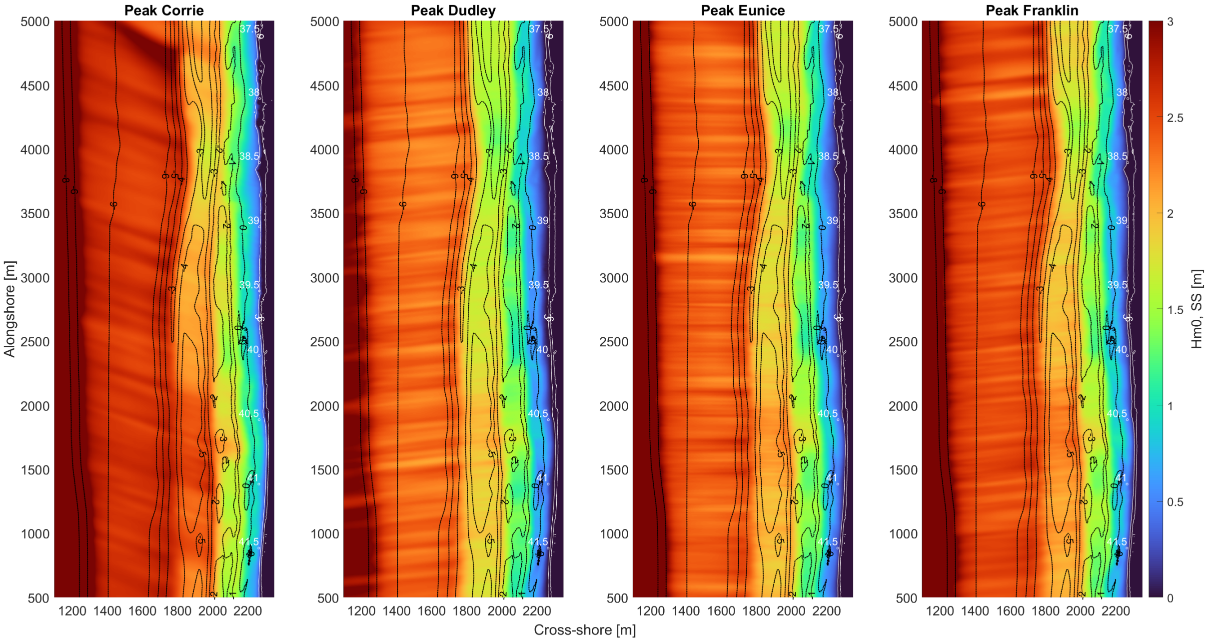

**Figure 5.24:** Short wave height at the peak of the storms for March 2023 with shoreface nourishment in the northern site and southern site at -5.5m NAP with a volume of 375m$^3$/m.

Figure 5.25 shows an overview of the infragravity wave height at the peak of the storms for March 2023 with beach nourishment in the northern site between NAP +0 - 3m with a volume of 100m$^3$/m. Compared to Figure 5.22, the infragravity wave height in the northern site is reduced in height during the peak of the storm. In addition, the magnitude of the arrows is lower at the higher part of the beach nourishment but greater at the lower part, indicating less sediment transport at the dune front but more sediment transport in the lower part.

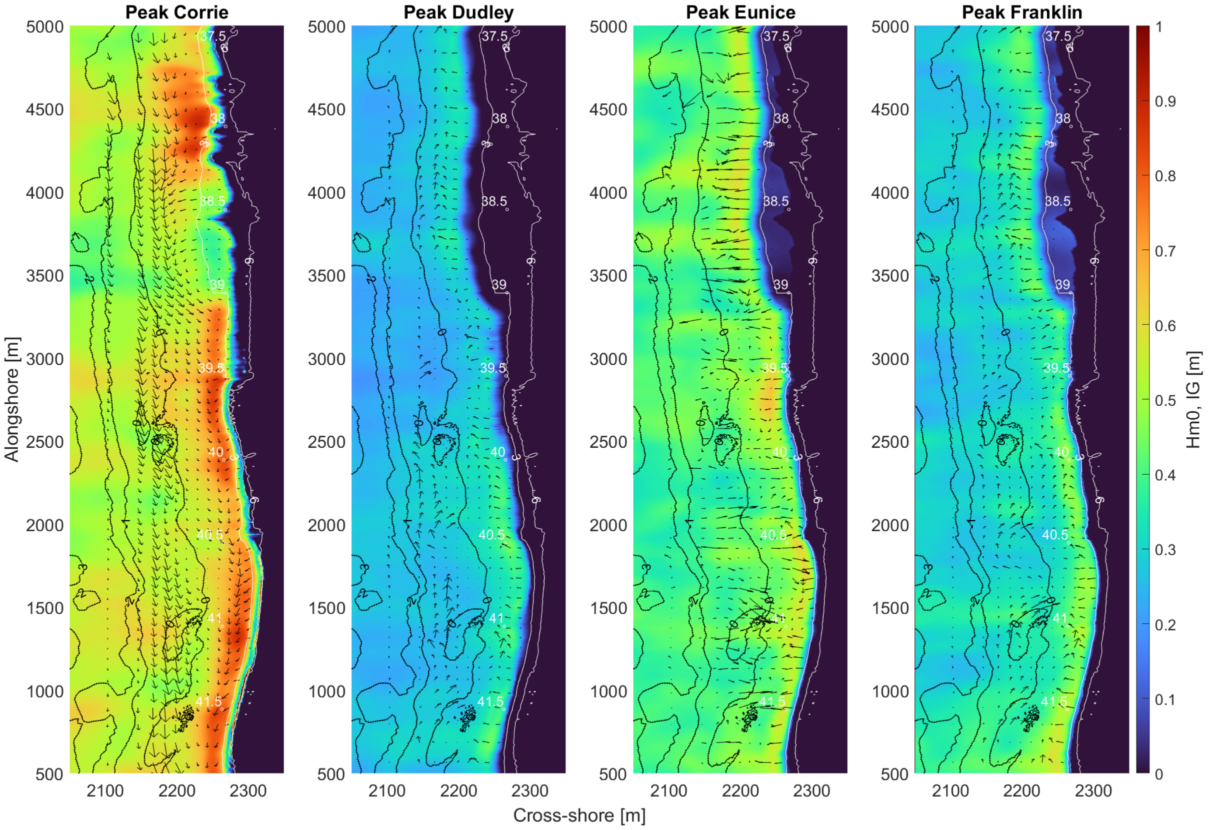

**Figure 5.25:** Infragravity wave height at the peak of the storms for March 2023 with beach nourishment in the northern site.

# Chapter 6

# Discussion

Beach-dune erosion is studied extensively but in relation to single storm events, calling for further research to improve the knowledge of coastal areas affected by storm sequences. In addition, nourishment may act as a buffer for incoming waves during a storm sequence. This study illustrates the effect of nourishments on dune erosion during a storm sequence. This is done by comparing the results of a nourished coast with an adjacent non-nourished coast. In addition, various nourishment designs have been added to investigate the effect of coastal protection. Morphological changes like dune erosion and hydrodynamic changes in the nearshore zone were discussed. This chapter summarizes the key findings of the study in Section 6.1. Section 6.2 interprets the key findings and relates them to literature. The limitations of the XBeach model are discussed as well in Section 6.3 as the implications for future research. Finally, Section 6.4 ends with several recommendations for further research.

## 6.1 Key findings

### 6.1.1 Modeling storm sequences with XBeach

Two methods were used to simulate a storm sequence with XBeach: the continuous method and the cumulative method. Compared to the observed data, both methods predicted the location and magnitude of dune erosion reasonably well but failed to properly predict the evolution of the bars and beach (Figure 4.4 and 4.7). Observations showed that bars mainly migrated offshore during storm events, contrary to the model's prediction of mainly onshore movement and flattening of the bar. The onshore bar movement caused excessive deposition on the beach, thereby adding volume to the beach. This phenomenon contradicted the observed data. Hence, the focus was on the evolution of the dune. The cumulative method was chosen as the preferred approach for simulating a storm sequence due to its better fit with the data. While the cumulative method felt unnatural, it still showed good results. In addition, this method reduced simulation time, as storms ran simultaneously, and their outcomes could be summed up.

### 6.1.2 Morphology

The analysis between the nourished (northern) and non-nourished (southern) sites of Egmond underscored the consistent presence of more significant dune erosion in the non-nourished region (Figure 5.10 and 5.11). Notable variations existed in the magnitude of dune erosion for different dates. March 2020, 2021, and 2022, along with October 2020, stood out with substantial dune erosion for the non-nourished site. However, a significant shift occurred in October 2022 and 2023, with dune erosion nearly halved compared to other dates, emphasizing the temporal variability in erosion patterns (Figure 5.11). In addition, variations in erosion intensity occurred with different storms where Storm Corrie had the biggest impact on dune erosion followed by Franklin, Eunice, and Dudley (Figure 5.12).

Variations in alongshore dune erosion volume provided a comprehensive perspective on erosion dynamics (Figure 5.10). A persistent erosion hotspot was identified in the non-nourished site, between beach poles 40.5 and 41.5. While this area consistently experienced erosion, the exact location and intensity exhibited annual variations. Notably, March 2020 witnessed substantial erosion extending northwards from the hotspot, and in March 2022, a significant erosion event occurred southwards of the identified hotspot. The nourished site exhibited a relatively constant pattern of dune erosion across the analyzed periods.

The driver's analysis revealed relationships between dune erosion and the slope of the nearshore zone (Table 5.1). The slopes of the surf zone and inner surf zone showed minimal impact, whereas the slope of the beach had a significant effect. Higher beach slopes correlated positively with increased dune erosion. In general, 2022 and 2023 stood out with lower correlations, suggesting potential anomalies during these periods. Furthermore, March 2020 and 2022 revealed a noteworthy correlation between dune slope and dune erosion.

Examining the influence of the outer subtidal bar on dune erosion, the study provided insight into the effect of the outer subtidal bar. The presence of the outer subtidal bar appeared to mitigate dune erosion, as evidenced by smaller average dune erosion volumes in designs with the outer subtidal bar compared to those without (Figure 5.14).

Transitioning to the nourishment designs, shoreface nourishments showed limited impact. The extension of shoreface nourishment to the south exhibited a subtle yet notable effect on dune erosion. On the other hand, the impact of beach nourishment stood out, significantly reducing dune erosion, where XBeach even predicted accretion of the foredune (Figure 5.19).

### 6.1.3 Hydrodynamics

The water level at fixed points revealed notable variations during storm events (Figure 5.6). During storm Corrie, water levels at seaward points (fixed points on NAP 0m at the cross-shore height of the beach poles) peaked at approximately 3 - 4m NAP. Other storms resulted in slightly lower heights, ranging from 2 - 3m NAP. Landward points (fixed points on NAP +3m at the cross-shore height of the beach poles) exhibited dry gaps during low water elevations because the result included only 15-minute bursts when the point was continuously submerged, leading to these dry gaps. Model output per second revealed higher water level heights at landward points than previously estimated. During storm Corrie, heights reached up to 4.8m NAP, while storms Eunice and Franklin saw peaks at 3.5m NAP. Storm Dudley's impact was negligible. Spatial variability in water level heights was observed, with points located in the non-nourished site experiencing longer durations of submersion compared to points located in the nourished site.

The height of short waves decreased as they travelled towards the shore, associated with breaking waves (Figure 5.4). Offshore, these waves reached an approximate height of 3.5m, gradually diminishing to a range of 1.5 to 2m in the inner surf zone. The spatial distribution of wave breaking was not uniform, indicating variations between the nourished an non-nourished sites. The waves broke more offshore in the nourished site due to the presence of the outer subtidal bar. In contrast, the non-nourished site exhibited differences in wave breaking due to a deeper area. This depth allowed the short waves to persist for a longer duration before breaking. A notable finding was the variability in short wave heights among different storms. Storm Corrie registered the highest short wave height, while storm Dudley recorded the lowest. Transitioning to the fixed points, the short wave height at the seaward located points was up to 1.5m during peak Corrie and roughly 1m during the other storms, whereas the wave heights at the landward located points did not exceed 0.5m during storm Corrie (Figure 5.7). This meant that the short wave was dissipating at the beach. The cross-shore wave evolution results of the four alongshore located fixed points showed the same behaviour as the short waves as mentioned before (Figure 5.9). Short wave heights decreased as waves moved towards the shore, breaking repeatedly on subtidal bars. Short wave heights were lower offshore in the nourished site compared to the non-nourished site due to the presence of the outer subtidal bar. Waves in the non-nourished site broke earlier in the cross-shore direction due to the presence of a middle subtidal bar but remained higher for longer durations compared to waves in the nourished site due to the deeper area in the non-nourished site and the seaward extension of the shoreline in the nourished site.

Turning attention to infragravity waves, infragravity waves exhibited an increase in height within the beach zone, with variations noted along the shore (Figure 5.5). During the peak of storm Corrie, the infragravity wave height reached a substantial 1m, while during other storms, the heights fluctuated between 0.5 to 0.8m at specific locations. Sediment transport was closely linked to infragravity waves. The analysis identified regions of significant sediment transport, notably in the southern hotspot. During storm Corrie, sediment was transported southwards, while during other storms, a reverse pattern was observed, with sediment moving northwards. Transitioning to the fixed points, the seaward located points exhibited notable differences in infragravity wave heights, particularly during storm Corrie, where heights ranged between 0.5 to 1m (Figure 5.8). In contrast, other storms yielded lower heights, ranging from 0.25 to 0.5m. The landward located points showed infragravity wave heights of 0.5 to 1m during storm Corrie. The infragravity wave height during the other storms was not noticeable. The cross-shore wave evolution results of the four alongshore located fixed points showed the evolution of the infragravity wave in more detail (Figure 5.9). The infragravity wave height increased as waves reached shallow water. Infragravity wave heights exceeded those of short waves in the beach zone. The highest values of infragravity wave height were observed in the non-nourished site, corresponding to the southern erosion hotspot. Specifically, the infragravity wave height reached approximately 1m at the beach in the most southern point, while ranging between 0.5m to 0.7m at other points during storm Corrie. At the most northern points and the second southern point, the infragravity wave height reached roughly 0.75m. Overall, the infragravity wave height exhibited consistent patterns across different storms, with higher values observed in the non-nourished site and a gradual decrease towards the nourished site. Furthermore, the infragravity wave height exhibited a consistent trend of higher magnitude in the non-nourished site (Figure 5.13).

Moving on to the effect of nourishments on nearshore hydrodynamics. Overall, the absence of the outer subtidal bar, created and maintained by shoreface nourishments, significantly influenced both short and infragravity wave heights (Figure 5.15 and 5.17). Removal of the outer subtidal bar resulted in short waves breaking at the middle subtidal bar instead of the outer subtidal bar. In the absence of the outer subtidal bar, short wave heights increased by 10 to 20cm in some shallow areas and up to 10cm in some spots at the beach compared to short wave heights when there is an outer subtidal bar. Conversely, short wave heights decreased up to 10cm in some sections in the deeper areas. Infragravity wave heights experienced an increase of up to 15cm at erosion hotspots when the outer subtidal bar was removed.

Shoreface nourishment designs mainly affected the wave breaking point, with minimal impact on dune erosion (Figure 5.23). Differences in wave height were minimal compared to results without nourishment (Figure 5.21). Shoreface nourishment in both northern and southern sites caused waves to break more offshore in both sites (Figure 5.24). The formation of a breaker bar in the south resulted in an increase in wave height in the southern deeper area, while a reduction in wave height at the landward side of this deeper area was observed. Beach nourishment in the northern site reduced infragravity wave height during peak storms (Figure 5.25).

## 6.2 Interpretation

### 6.2.1 Nourished vs non-nourished

The difference in nearshore hydrodynamics and morphological changes between the nourished and non-nourished sites of Egmond can be attributed to several factors. This section will list the factors. The first paragraph provides a general description of the effect of shoreface nourishments on the nearshore zone and dune erosion. The second paragraph discusses alongshore variations in more detail.

**Shoreface nourishments**

The shoreface nourishments at Egmond created and maintained the outer subtidal bar. The outer subtidal bar acts like a breaker bar affecting the wave field as it propagates towards the shore. The incoming short waves break more offshore in the nourished area due to the presence of the outer subtidal bar. As a result, the wave energy decreases and short wave height reduces when they move onshore. This supports shoreface nourishment observations at Egmond done by van Duin et al. (2004). Additionally, the simulation without the outer subtidal bar provides extra insight into how the bar affects hydrodynamics. The simulation indicates that in the absence of an outer subtidal bar, shorter waves exhibit increased heights upon reaching shallower regions. This phenomenon arises due to larger incoming waves maintaining elevated levels for longer durations. Furthermore, a decrease in short wave height is observed at certain deeper areas, attributed to larger waves reaching the bed more rapidly, resulting in wave transformation and breaking.

Cohen and Brière (2007) found landward migration of the middle subtidal bars after shoreface nourishment. This is also visible in this study (Appendix B). The middle subtidal bar in the nourished site is pushed more landward than the middle subtidal bar in the non-nourished site, with as a result the smaller deeper areas in the nourished site (between x = 1750 and 2000m) compared to the bigger deeper area in the non-nourished site (between x = 1800 and 2000m) affecting wave transformation. Overall, the beach width is also larger in the nourished site compared to the non-nourished site (Figure 3.4), contributing to the assumption that the coastline position is linked to the location of the bars (Mastbergen et al., 2017). A wider beach can act as a buffer, dissipating wave energy before it reaches the dunes, and reducing dune erosion. This is consistent with the observation of Itzkin et al. (2021), who found a strong inverse relationship between beach width and dune erosion. The increased width of the beach can also be related to recreation at the nourished site (Section 3.2).

### Alongshore variability

Visually, a relationship between nearshore bathymetry and erosional hotspots at the dune is found (Appendix H). This is also the cause of temporal and spatial variability for alongshore dune erosion. As Castelle et al. (2015) and Hanley et al. (2014) stated, the waves break repeatedly at the subtidal bars, acting as a filter for the incoming waves which cause less dune erosion behind these shallow areas. Similarly, the deeper alongshore areas in the nourished and non-nourished sites (between x = 1750 and 2000m) allow the wave to persist for a longer duration before breaking, and as a result, the breakpoint is located more landwards. Particularly in the deeper area at the non-nourished site, the short waves persist at elevated heights for an extended duration before breaking near the shore. Breaking waves cause rising of the water level which creates radiation stress gradients along the coast. These gradients drive nearshore currents and sediment transport.

Infragravity wave height exhibits higher levels near the dune than short wave height. This is because on gently sloping beaches like Egmond, the bound and bore mechanism dominates, which causes infragravity waves to become relatively large compared to short waves, leading to higher harmonics and wave steepening, as also found by de Bakker et al. (2016). The infragravity waves contribute to run-up and therefore promote dune erosion. This relationship is also found between the locations where high infragravity wave heights occur and the erosion hotspots. In addition, the consistent trend of higher magnitude of infragravity wave height at the locations of the fixed points in the non-nourished site compared to the nourished site might be explained by the presence of steeper slopes in certain areas of the non-nourished site. On steep beach slopes, energy is spread to a large range of higher (short-wave) frequencies, but overall less energy is removed from the infragravity band than on more gentle slopes (de Bakker et al., 2016). Furthermore, the more landward-located breakpoint of the short waves and the higher short wave height in the non-nourished site might also influence the height of the infragravity wave height, which is in line with the linear dependency of these short and infragravity wave heights found by Oh et al. (2023).

Less erosion is observed at the location where mega cusp horns are present (Appendix H). It is not as significant as the relationship found by Castelle et al. (2015), but still relatively visible that it should be noted. At the location of these horns, the beach is relatively wide. The moderate to strong correlation between dune erosion and beach slope underscores this, also stated by Cohn et al. (2021). The location of the inner subtidal bars is in line with the megacusp horns, which have a buffer effect on dune erosion. Especially for the bathymetry of March 2022, just after the storm, this is visible. This is in line with Castelle et al. (2015), which shows the coupling mechanism between bars and horns during storms.

The weak relationship between the slope of the (inner) surf zone and dune erosion contradicts the coupling mechanism between bars and horns since horns act as a buffer for incoming waves limiting dune erosion (Table 5.1). The surf zone slope shows a very weak relationship. The inner surf zone slope does too, however, the results show the same pattern only shifted. Where dune erosion increases, the inner surf zone slope also increases, but more shifted to the north (Figure 5.3b; the red line follows the same pattern but is located more to the right). This could be the result of obliquely incoming waves. The study of Cohn et al. (2021) found a weak correlation between surf zone slope and dune erosion but a higher correlation between inner surf zone slope and dune erosion relative to beach slope and dune slope. This study found also a weak correlation between surf zone slope and dune erosion but a higher correlation between beach/dune slope and dune erosion relative to (inner) surf zone slope. The differences in beach states could explain this, as Cohn et al. (2021) study takes place on an intermediate beach in the USA, while this study focuses on the dissipative beach of Egmond. In addition, the waves in Cohn et al. (2021) study approach the coast almost perpendicular, which likely yields better results regarding inner surf zone slope and dune erosion.

The relationship between nearshore bathymetry and erosional hotspots at the dune may also be an explanation for the significant temporal shift in dune erosion volume for October 2022 and 2023, with dune erosion nearly halved compared to other dates. The longshore morphology in the bathymetries dated after February 2022 is more uniform (bar straightening) due to the simulated storms which took place in January and February 2022. This is also highlighted by the reduced temporal variability in erosion, where the magnitudes of dune erosion volume decreased. This does not explain why March 2022 showed relatively high dune erosion volume while this bathymetry was measured just after the storms. Instead, this has to do with dune slope since March 2022 shows a strong correlation with dune erosion. The front dune is taken away due to storm waves in winter 2021/2022, leaving a steep dune scarp which is prone to wave attack. This observation is also stated by de Winter et al. (2015), who found that dune erosion is influenced by the steepness of the dune front.

### 6.2.2 Nourishment designs

The shoreface nourishment designs have a limited impact on dune erosion. This makes sense since shoreface nourishment is primarily meant to feed the coast gradually over a longer period and the simulation in this study lasts only a few hours. In addition, it is questionable if XBeach can model such a long-term simulation. So the main purpose of the shoreface nourishment design in this study is to serve as a breaker bar. The different shoreface nourishment design in the northern nearshore zone does not affect the amount of dune erosion. The shoreface nourishment at depths of NAP -5.5 and -3m increases the width of the outer and middle subtidal bar, thereby affecting the breakpoint of the short waves, causing it to shift further offshore. However, the impact of the infragravity wave height on the beach is negligible. When the shoreface nourishment at NAP -5.5m is extended towards the south, creating a breaker bar, it does affect the amount of dune erosion. An important observation is that the short wave height in the southern deeper area (between x = 1750 and 2000m) becomes higher. This is because the offshore wave height is significantly diminished by the formation of the breaker bar in the south, thereby impeding their rapid attainment of the critical depth necessary for breaking, especially when compared to larger waves. Since the short wave height is larger in the southern deeper area, they are also breaking faster causing a reduction of the short wave and infragravity wave height near the beach. This is also visible in the reduction of dune erosion at the southern site. Compared to shoreface nourishment designs, the beach nourishment designs have a larger impact on dune erosion, since the entire beach and the height of the dune toe is raised. The dune is less prone to wave attacks during storms. Accretion of the foredune is observed as XBeach pushed the top of the beach nourishment landward, thereby adding volume to the foredune.

## 6.3 Limitations

The BOI-version of XBeach was derived for 1D simulations. This study uses the BOI-version for 2D simulations. The consistency between the XBeach 1D and 2D results is unknown. This will not disadvantage the outcome of the study since the objective was to observe a trend between a nourished and non-nourished coast, for which XBeach performs well. No exact magnitudes were needed.

Due to the lack of observed data, the XBeach validation is limited. The only available data to compare the XBeach results is the observed difference between March 2021 and 2022. As mentioned before, this will not disadvantage the outcome of the study since the objective was to observe a trend.

Investigation of bar and beach evolution during a storm sequence is not possible. XBeach predicts flattening and onshore movement of the bars. In addition, the intertidal bar is pushed to the beach causing a lot of deposition. This does not match the observed data where offshore movement is visible. The bar and beach evolution has a limited impact on dune evolution in the model. In addition, the modeled dune performs quite well compared to the observed data so the objective of this study is not harmed.

The reliability of the infragravity wave height for the 2D maps is impacted by using the calculation $8 * \sqrt{\text{zvar}}$. In this case, the infragravity wave height is based on the entire frequency domain present in the water level. It hence includes very low-frequency waves, instead of only the infragravity wave domain (0.005-0.05 Hz). This results in higher wave heights (Coumou et al., 2022). This has little impact on the objective of this study since these 2D maps are meant to provide an overview of the relative infragravity wave height and location.

## 6.4 Recommendations

Based on the discussion of the results, recommendations for practical implementation and further research are listed below. It is divided into coastal management, model setup, and suggestions for follow-up research.

Based on this study, it is encouraged to continue nourishment as it has a positive effect on coastal protection during a storm sequence; the non-nourished site exhibits more dune erosion than the nourished site during a storm sequence. This is primarily because nourishments influence nearshore morphology and act as a buffer for incoming waves, consequently leading to variations in alongshore dune erosion.

Regarding the XBeach model, further research is needed for fine-tuning (recalibration) the results. First, more measurements are recommended to improve the validation of the XBeach results regarding storm sequences. This also provides opportunities for calibration of the BOI version for transitioning XBeach from 1D to 2D. Second, optimizing parameter settings enhances the accuracy of predicting bar movements. It is advisable to conduct testing to mitigate onshore bar displacement during storm sequences. Sediment transport and wave-breaking parameters present an opportunity for enhancement in this regard (Rafati et al., 2021). In addition, Roelvink and Costas (2019) developed a new approach to simulate the coupled beach-berm-dune system forced by waves wind, and tides. It can be applied at scales from a single event to decades. If feasible, it would be possible to more accurately simulate the evolution of the bar and beach during a storm sequence.

Various suggestions for further research can be made. First, this study utilized offshore data from storms Corrie, Dudley, Eunice, and Franklin to simulate storm sequences. However, numerous other combinations and variations within a cluster can be explored to investigate how the cumulative storm sequence simulation method works concerning more extreme wave data and how the nourishments affect dune erosion during different magnitudes of storm sequence. Here, it is recommended to use more intense storms since the level of dune erosion observed in this study is minimal. In addition, since only the offshore data of the storm waves is joined together, the beach/dune recovery after these storms is excluded. Second, in this study, the shoreface nourishment designs function as a breaker bar due to the limited simulation time. To effectively simulate the effect of nourishments during a storm sequence, a long-term model must be established to observe also the feeding function of the shoreface nourishment. The study by Roelvink and Costas (2019) may also offer a solution for this. Third, conducting further research on the effect of beach slopes on infragravity waves may provide additional insights into their impacts on dune erosion at Egmond. This is relevant as only eight fixed points were utilized in this study to investigate the alongshore hydrodynamic variation. Finally, this study did not focus on the role of vegetation, despite its significant impact on morphological changes.

# Chapter 7

# Conclusion

The current study aims to make the effect of nourishments on dune erosion during a storm sequence insightful. The central questions for this study were as follows:

- What is the difference between a nourished and adjacent non-nourished coast during a storm sequence?
- What is the protective effect of different nourishment designs during a storm sequence?

To answer these questions, a numerical model, offshore wave and tidal data and several bathymetries of the partially nourished Egmond coast were used to investigate the persistent effects of nourishments on dune erosion during a storm sequence. This involved examining the differences in morphology between a nourished and non-nourished coast and several simulations examining the buffering effect of nourishment on dune erosion.

Bathymetric data collected at various dates from 2020 onwards for Egmond (beach pole 37 - 42) reveal differences in nearshore morphology between nourished (37 - 39.5) and non-nourished (39.5 - 42) sites. The bathymetry indicates the presence of 2 - 3 subtidal bars and an intertidal bar. Shoreface nourishment appears to stop natural bar dynamics, while cyclic dynamics are observed at the non-nourished site. Previous shoreface nourishments have created and sustained the outer subtidal bar, functioning as a breaker and feeder bar. Additionally, the middle subtidal bar in the nourished site is shallower and closer to the shore compared to the non-nourished site. This middle subtidal bar either remains stable or migrates landwards. The bathymetric data also reveals the presence of two deeper areas between the middle and inner subtidal bars in the nourished site, while only one deep area is observed in the non-nourished site. This deep area in the non-nourished site is deeper and located closer to the shore. Furthermore, the beach and dune exhibit a steeper profile in the non-nourished site.

The numerical model XBeach was utilized to compute the hydrodynamic and morphodynamic response of the Egmond coast during a storm sequence. Offshore waves measured during storms Corrie, Dudley, Eunice, and Franklin in winter 2021/2022 were combined to simulate a storm sequence. Two methods were employed to simulate a storm sequence with XBeach: the continuous method and the cumulative method. During both methods, XBeach predicts onshore movement and flattening of the bar, causing deposition on the beach. However, this phenomenon contradicts observed data. Therefore, the focus of the study shifts to the evolution of the dune. Finally, the cumulative method was chosen as the preferred approach due to the better fit with the data and the ability to reduce simulation time by running storms simultaneously and summing up their outcomes.

The results indicate a consistent pattern of increased dune erosion in the non-nourished site. However, a significant shift occurred after March 2022, with dune erosion nearly halved compared to other dates, which can be attributed to the changes in nearshore morphology (bar-straightening). Across the simulations with the six bathymetries, a persistent erosion hotspot was identified between beach poles 40.5 and 41.5. Notably, there exists a pronounced correlation between the presence of steep beaches and the erosion of dunes. Among the various storms examined, it was found that Corrie exerted the most significant influence on dune erosion. Transitioning to hydrodynamics, the waves break repeatedly at the subtidal bars, acting as a filter for the incoming waves. The incoming short waves break more offshore in the nourished area due to the presence of the outer subtidal bar. The deeper alongshore areas between the middle and inner subtidal bar allow the wave to persist for a longer duration before breaking, as a result, the breakpoint is located more landwards. Especially in the deeper area at the non-nourished site, the short wave remains high for a longer duration. Infragravity wave height exhibits higher levels near the dune than short wave height. Furthermore, the infragravity wave height exhibits a consistent trend of higher magnitude along the coastline in the non-nourished site compared to the nourished site. This phenomenon is attributed to the breakpoint of the short waves and the slope of the beach. The location of high infragravity waves is related to erosion hotspots.

Different variations of the nourishment design implemented in 2023/2024 were incorporated into the bathymetry to assess their effects on hydrodynamics and morphodynamics. The shoreface nourishment designs have a limited impact on dune erosion. This makes sense since shoreface nourishment is primarily meant to feed the coast gradually over a longer period and the simulation in this study lasts only a few hours. In addition, it is questionable if XBeach can model such a long-term simulation. The main purpose of the shoreface nourishment design in this study is to serve as a breaker bar. The shoreface nourishment designs implemented in the nourished site aim to increase the width of the outer and middle subtidal bars, thereby affecting the breakpoint of the short waves and causing them to shift further offshore. However, the impact of the infragravity wave height on the beach is negligible. When the shoreface nourishment design is extended towards the south to create a breaker bar, it has a small effect on the magnitude of dune erosion. Compared to shoreface nourishment designs, beach nourishment designs have a larger impact on dune erosion. This is because beach nourishment raises the entire beach and increases the height of the dune toe. XBeach predicts foredune accretion as the beach nourishment pushes the top of the beach landward, adding volume to the foredune.

This study demonstrates that nourishments have a positive effect on coastal protection during a storm sequence. Primarily, nourishments influence nearshore morphology, acting as a buffer for incoming waves and consequently leading to a reduction in dune erosion. Additionally, different scenarios and designs illustrate the protective effect of a nourishment on dune erosion during storms. The study findings contribute to encouraging nourishment in the context of coastal safety.

# Bibliography

R. Almar, B. Castelle, B. Ruessink, N. Sénéchal, P. Bonneton, and V. Marieu. Two- and three-dimensional double-sandbar system behaviour under intense wave forcing and a meso–macro tidal range. *Continental Shelf Research*, 30(7):781–792, 2010. ISSN 0278-4343. doi:10.1016/j.csr.2010.02.001. URL `https://www.sciencedirect.com/science/article/pii/S0278434310000348`.

J. Aucan and F. Ardhuin. Infragravity waves in the deep ocean: An upward revision. *Geophysical Research Letters*, 40:1–5, 07 2013. doi:10.1002/grl.50321.

T. Baldock, U. Gravois, D. Callaghan, G. Davies, and S. Nichol. Methodology for estimating return intervals for storm demand and dune recession by clustered and non-clustered morphological events. *Coastal Engineering*, 168:103924, 2021. ISSN 0378-3839. doi:https://doi.org/10.1016/j.coastaleng.2021.103924. URL `https://www.sciencedirect.com/science/article/pii/S0378383921000843`.

M. A. Bender, T. R. Knutson, R. E. Tuleya, J. J. Sirutis, G. A. Vecchi, S. T. Garner, and I. M. Held. Modeled impact of anthropogenic warming on the frequency of intense atlantic hurricanes. *Science*, 327(5964):454–458, 2010. doi:10.1126/science.1180568.

X. Bertin, A. de Bakker, A. van Dongeren, G. Coco, G. André, F. Ardhuin, P. Bonneton, F. Bouchette, B. Castelle, W. C. Crawford, M. Davidson, M. Deen, G. Dodet, T. Guérin, K. Inch, F. Leckler, R. McCall, H. Muller, M. Olabarrieta, D. Roelvink, G. Ruessink, D. Sous, Éléonore Stutzmann, and M. Tissier. Infragravity waves: From driving mechanisms to impacts. *Earth-Science Reviews*, 177:774–799, 2018. ISSN 0012-8252. doi:https://doi.org/10.1016/j.earscirev.2018.01.002. URL `https://www.sciencedirect.com/science/article/pii/S0012825217303239?via%3Dihub`.

J. Bosboom and M. J. Stive. Coastal dynamics. 2021. doi:https://doi.org/10.5074/T.2021.001.

Boskalis/Flying Focus. URL `https://www.schuttevaer.nl/nieuws/offshore/2021/09/08/vooroeversuppleties-bij-texel-gaan-laatste-fase-in/`. Accessed January 29, 2024.

E. Brand, G. Ramaekers, and Q. Lodder. Dutch experience with sand nourishments for dynamic coastline conservation–an operational overview. *Ocean & Coastal Management*, 217:106008, 2022. doi:https://doi.org/10.1016/j.ocecoaman.2021.106008.

K. Bryan, P. Howd, and A. Bowen. Field observations of bar-trapped edge waves. *Journal of Geophysical Research: Oceans*, 103(C1):1285–1305, 1998. doi:https://doi.org/10.1029/97JC02938.

B. Castelle and G. Masselink. Morphodynamics of wave-dominated beaches. *Cambridge Prisms: Coastal Futures*, 1:1–32, 2023. doi:10.1017/cft.2022.2.

B. Castelle, V. Marieu, S. Bujan, K. D. Splinter, A. Robinet, N. Sénéchal, and S. Ferreira. Impact of the winter 2013–2014 series of severe western europe storms on a double-barred sandy coast: Beach and dune erosion and megacusp embayments. *Geomorphology*, 238:135–148, 2015. ISSN 0169-555X. doi:https://doi.org/10.1016/j.geomorph.2015.03.006.

A. Cohen and C. Brière. Evaluatie van de uitgevoerde suppleties bij egmond op basis van argus video waarnemingen. 2007. URL `http://resolver.tudelft.nl/uuid:008d440d-6535-4bd9-b100-00206bce3881`.

N. Cohn, K. L. Brodie, B. Johnson, and M. L. Palmsten. Hotspot dune erosion on an intermediate beach. *Coastal Engineering*, 170:103998, 2021. ISSN 0378-3839. doi:https://doi.org/10.1016/j.coastaleng.2021.103998. URL `https://www.sciencedirect.com/science/article/pii/S0378383921001502`.

M. P. Conlin, N. Cohn, and P. N. Adams. Total water level controls on the trajectory of dune toe retreat. *Geomorphology*, 438:108826, 2023. ISSN 0169-555X. doi:https://doi.org/10.1016/j.geomorph.2023.108826. URL `https://www.sciencedirect.com/science/article/pii/S0169555X23002465`.

L. Coumou, R. van Santen, J. van der Baan, R. McCall, A. de Bakker, E. Quataert, and R. de Goede. Validation of dune erosion model xbeach: Development of 'boi sandy coasts'. Technical report, Arcadis and Deltares, 2022.

A. T. M. de Bakker, M. F. S. Tissier, and B. G. Ruessink. Beach steepness effects on nonlinear infragravity-wave interactions: A numerical study. *Journal of Geophysical Research: Oceans*, 121(1):554–570, 2016. doi:https://doi.org/10.1002/2015JC011268. URL `https://agupubs.onlinelibrary.wiley.com/doi/abs/10.1002/2015JC011268`.

S. De Keijzer. De invloed van stormcondities op het bankengedrag bij egmond en bergen vóór en na een onderwatersuppletie. *RIKZ/OS/2004/123 W*, 2004.

M. A. de Schipper, S. de Vries, G. Ruessink, R. C. de Zeeuw, J. Rutten, C. van Gelder-Maas, and M. J. Stive. Initial spreading of a mega feeder nourishment: Observations of the sand engine pilot project. *Coastal Engineering*, 111:23–38, 2016. ISSN 0378-3839. doi:https://doi.org/10.1016/j.coastaleng.2015.10.011.

R. De Winter and B. Ruessink. Sensitivity analysis of climate change impacts on dune erosion: case study for the dutch holland coast. *Climatic Change*, 141(4):685–701, 2017. doi:https://doi-org.proxy.library.uu.nl/10.1007/s10584-017-1922-3.

R. de Winter, F. Gongriep, and B. Ruessink. Observations and modeling of alongshore variability in dune erosion at egmond aan zee, the netherlands. *Coastal Engineering*, 99:167–175, 2015. ISSN 0378-3839. doi:https://doi.org/10.1016/j.coastaleng.2015.02.005. URL `https://www.sciencedirect.com/science/article/pii/S0378383915000307`.

S. Eichentopf, H. Karunarathna, and J. M. Alsina. Morphodynamics of sandy beaches under the influence of storm sequences: Current research status and future needs. *Water Science and Engineering*, 12(3):221–234, 2019. ISSN 1674-2370. doi:https://doi.org/10.1016/j.wse.2019.09.007.

Ó. Ferreira. Storm groups versus extreme single storms: predicted erosion and management consequences. *Journal of Coastal Research*, pages 221–227, 2005.

F. Feser, M. Barcikowska, O. Krueger, F. Schenk, R. Weisse, and L. Xia. Storminess over the north atlantic and northwestern europe—a review. *Quarterly Journal of the Royal Meteorological Society*, 141(687):350–382, 2015. doi:https://doi.org/10.1002/qj.2364.

P. Galiatsatou and P. Prinos. Joint probability analysis of extreme wave heights and storm surges in the aegean sea in a changing climate. *E3S Web of Conferences*, 7:02002, 01 2016. doi:10.1051/e3sconf/20160702002.

B. Grasmeijer, J. van Nieuwkoop, T. Price, M. van Eck, F. Buschman, and M. Doeleman. Eindrapport quick reaction force 2022. 2023.

N. M. Grunnet and B. Ruessink. Morphodynamic response of nearshore bars to a shoreface nourishment. *Coastal Engineering*, 52(2):119–137, 2005. ISSN 0378-3839. doi:https://doi.org/10.1016/j.coastaleng.2004.09.006.

N. M. Grunnet, D.-J. R. Walstra, and B. Ruessink. Process-based modelling of a shoreface nourishment. *Coastal Engineering*, 51(7):581–607, 2004. ISSN 0378-3839. doi:https://doi.org/10.1016/j.coastaleng.2004.07.016.

M. Hanley, S. Hoggart, D. Simmonds, A. Bichot, M. Colangelo, F. Bozzeda, H. Heurtefeux, B. Ondiviela, R. Ostrowski, M. Recio, R. Trude, E. Zawadzka-Kahlau, and R. Thompson. Shifting sands? coastal protection by sand banks, beaches and dunes. *Coastal Engineering*, 87:136–146, 2014. ISSN 0378-3839. doi:https://doi.org/10.1016/j.coastaleng.2013.10.020. URL `https://www.sciencedirect.com/science/article/pii/S0378383913001762`. Coasts@Risks: THESEUS, a new wave in coastal protection.

B. J. A. Huisman, D.-J. R. Walstra, M. Radermacher, M. A. de Schipper, and B. G. Ruessink. Observations and modelling of shoreface nourishment behaviour. *Journal of Marine Science and Engineering*, 7(3), 2019. ISSN 2077-1312. doi:https://doi.org/10.3390/jmse7030059.

M. Itzkin, L. J. Moore, P. Ruggiero, S. D. Hacker, and R. G. Biel. The relative influence of dune aspect ratio and beach width on dune erosion as a function of storm duration and surge level. *Earth Surface Dynamics*, 9(5):1223–1237, 2021. doi:10.5194/esurf-9-1223-2021. URL `https://esurf.copernicus.org/articles/9/1223/2021/`.

L. J. Jenkins, I. D. Haigh, P. Camus, D. Pender, J. Sansom, R. Lamb, and H. Kassem. The temporal clustering of storm surge, wave height, and high sea level exceedances around the uk coastline. *Natural Hazards*, 115(2):1761–1797, 2023. doi:https://doi-org.proxy.library.uu.nl/10.1007/s11069-022-05617-z.

H. Karunarathna, D. Pender, R. Ranasinghe, A. D. Short, and D. E. Reeve. The effects of storm clustering on beach profile variability. *Marine Geology*, 348:103–112, 2014. ISSN 0025-3227. doi:https://doi.org/10.1016/j.margeo.2013.12.007.

Kustviewer. `https://www.openearth.nl/coastviewer-static/`, 2024. Accessed 26-01-2024.

G. Masselink and S. Heteren. Response of wave-dominated and mixed-energy barriers to storms. *Marine Geology*, 352:321–347, 06 2014. doi:10.1016/j.margeo.2013.11.004.

G. Masselink, B. Castelle, T. Scott, G. Dodet, S. Suanez, D. Jackson, and F. Floc'h. Extreme wave activity during 2013/2014 winter and morphological impacts along the atlantic coast of europe. *Geophysical Research Letters*, 43(5):2135–2143, 2016. doi:https://doi.org/10.1002/2015GL067492.

D. Mastbergen, K. Nederhoff, B. van der Valk, and M. Maarse. Beheerbibliotheek noord-holland: Beschrijvingen van het kustvak ter ondersteuning van het beheer en onderhoud van de kust. 2017.

Ministerie van Verkeer en Waterstaat. Kustverdediging na 1990: Beleidskeuze voor de kustlijnzorg. *Kamerstuk 21.136 nr 5 (2e kamer) vergaderjaar 98-90.*, 1990. URL `http://resolver.tudelft.nl/uuid:a4c7d579-d528-4f26-9364-1346817230ba`.

J.-E. Oh, Y. Chang, K. Ryu, and W. Jeong. Infragravity wave height dependency on short wave parameters – observations on the east coast of south korea. *Frontiers in Marine Science*, 10, 05 2023. doi:10.3389/fmars.2023.1194472.

C. A. Pinto, R. Taborda, C. Andrade, P. Baptista, P. A. Silva, D. Mendes, and J. Pais-Barbosa. Morphological development and behaviour of a shoreface nourishment in the portuguese western coast. *Journal of Marine Science and Engineering*, 10(2), 2022. ISSN 2077-1312. doi:https://doi.org/10.3390/jmse10020146.

S. Quartel and B. Grasmeijer. Dynamiek van het strand bij noordwijk aan zee en egmond aan zee en het effect van suppleties. *Rijksinstituut voor Kust en Zee (RIKZ). Opdracht RKZ-1667*, 2007.

M. Radermacher, M. de Schipper, T. Price, B. Huisman, S. Aarninkhof, and A. Reniers. Behaviour of subtidal sandbars in response to nourishments. *Geomorphology*, 313:1–12, 2018. ISSN 0169-555X. doi:https://doi.org/10.1016/j.geomorph.2018.04.005.

Y. Rafati, T.-J. Hsu, S. Elgar, B. Raubenheimer, E. Quataert, and A. van Dongeren. Modeling the hydrodynamics and morphodynamics of sandbar migration events. *Coastal Engineering*, 166:103885, 2021. ISSN 0378-3839. doi:https://doi.org/10.1016/j.coastaleng.2021.103885. URL `https://www.sciencedirect.com/science/article/pii/S0378383921000454`.

Rijkswaterstaat. Kustlijnkaarten 2022. 2021.

H. Ritzema and J. van Loon-Steensma. Coping with climate change in a densely populated delta: A paradigm shift in flood and water management in the netherlands. *Irrigation and Drainage*, 67(S1):52–65, 2018. doi:https://doi.org/10.1002/ird.2128.

D. J. Roelvink and S. Costas. Coupling nearshore and aeolian processes: Xbeach and duna process-based models. *Environmental Modelling Software*, 115, 02 2019. doi:10.1016/j.envsoft.2019.02.010.

D. J. Roelvink, A. Reniers, A. van Dongeren, J. Thiel de Vries, R. McCall, and J. Lescinski.

Modelling storm impacts on beaches, dunes and barrier islands. *Coastal Engineering*, 56: 1133–1152, 11 2009. doi:10.1016/j.coastaleng.2009.08.006.

D. J. Roelvink, A. van Dongeren, R. McCall, B. Hoonhout, A. van Rooijen, P. van Geer, L. de Vet, K. Nederhoff, and E. Quataert. Xbeach technical reference: Kingsday release. 04 2015. doi:10.13140/RG.2.1.4025.6244.

G. Ruessink. Bound and free infragravity waves in the nearshore zone under breaking and nonbreaking conditions. *Journal of Geophysical Research: Oceans*, 103(C6):12795–12805, 1998. doi:https://doi.org/10.1029/98JC00893.

G. Ruessink, R. Grinten, L. Vonhögen-Peeters, G. Ramaekers, and Q. Lodder. Nearshore evolution at noordwijk (nl) in response to nourishments, as inferred from argus video imagery. 01 2012. doi:10.3990/2.194.

G. Ruessink, C. Schwarz, T. Price, and J. Donker. A multi-year data set of beach-foredune topography and environmental forcing conditions at egmond aan zee, the netherlands. *Data*, 4:73, 05 2019. doi:10.3390/data4020073.

R. Schrijvershof, L. Brakenhoff, and B. Grasmeijer. Hydrodynamics and bedforms at the dutch lower shoreface. analysis of adcp, adv and sonar observations. Technical report, Report 1220339-007-ZKS-0009,. Deltares, Delft, 2019.

C. Sherwood, A. van Dongeren, J. Doyle, C. Hegermiller, T.-J. Hsu, T. Kalra, M. Olabarrieta, A. Penko, Y. Rafati, D. J. Roelvink, M. van der Lugt, J. Veeramony, and J. Warner. Modeling the morphodynamics of coastal responses to extreme events: What shape are we in? *Annual Review of Marine Science*, 14, 07 2021. doi:10.1146/annurev-marine-032221-090215.

R. Spanhoff, S. De Keijzer, A. Walburg, and E. Biegel. Evaluatie onderwatersuppleties egmond en bergen. *RIKZ/OS/2004/112W*, 2004. URL `http://resolver.tudelft.nl/uuid:c17162db-fa79-440f-bb3d-fc5f778c865b`.

A. Spek and Q. Lodder. A new sediment budget for the netherlands; the effects of 15 years of nourishing (1991-2005). 2015. doi:https://doi-org.proxy.library.uu.nl/10.1142/9789814689977_0074.

K. D. Splinter, J. T. Carley, A. Golshani, and R. Tomlinson. A relationship to describe the cumulative impact of storm clusters on beach erosion. *Coastal Engineering*, 83:49–55, 2014. ISSN 0378-3839. doi:https://doi.org/10.1016/j.coastaleng.2013.10.001.

M. Stive, M. De Schipper, A. Luijendijk, R. Ranasinghe, J. Thiel de Vries, S. Aarminkhof, C. Gelder-Maas, S. Vries, M. Henriquez, and S. Marx. The sand engine: A solution for vulnerable deltas in the 21st century? 06 2013.

G. Symonds, D. Huntley, and A. Bowen. Two-dimensional surf beat: Long wave generation by a time-varying breakpoint. *Journal of Geophysical Research*, 87:492–498, 01 1982. doi:10.1029/JC087iC01p00492.

N. Sénéchal, B. Castelle, and K. R. Bryan. *Storm Clustering and Beach Response*, chapter 8, pages 151–174. John Wiley Sons, Ltd, 2017. ISBN 9781118937099. doi:https://doi.org/10.1002/9781118937099.ch8.

M. J. van der Meulen, A. J. van der Spek, G. de Lange, S. H. Gruijters, S. F. van Gessel, B.-L. Nguyen, D. Maljers, J. Schokker, J. P. Mulder, and R. A. van der Krogt. Regional sediment deficits in the dutch lowlands: Implications for long-term land-use options (8 pp). *Journal of Soils and Sediments*, 7:9–16, 2007. doi:https://doi-org.proxy.library.uu.nl/10.1065/jss2006.12.199.

A. van der Spek, A. d. Kruif, and R. Spanhoff. Richtlijnen onderwatersuppleties. Technical report, Rijkswaterstaat, RIKZ, 2007.

J. van der Zanden. Sand transport processes in the surf and swash zones. 2016. doi:10.3990/1.9789036542456.

M. van Duin, N. Wiersma, D. Walstra, L. van Rijn, and M. Stive. Nourishing the shoreface: observations and hindcasting of the egmond case, the netherlands. *Coastal Engineering*, 51(8): 813–837, 2004. ISSN 0378-3839. doi:https://doi.org/10.1016/j.coastaleng.2004.07.011. Coastal Morphodynamic Modeling.

P. van Geer. Kustonderhoud en duinveiligheid. 2012. URL `https://publications.deltares.nl/1206189_000.pdf`.

M. van Gent, J. van Thiel de Vries, E. Coeveld, J. de Vroeg, and J. van de Graaff. Large-scale dune erosion tests to study the influence of wave periods. *Coastal Engineering*, 55(12): 1041–1051, 2008. ISSN 0378-3839. doi:https://doi.org/10.1016/j.coastaleng.2008.04.003. URL `https://www.sciencedirect.com/science/article/pii/S0378383908000835`.

T. Vermaas, S. Boersen, R. Wilmink, and Q. Lodder. National analysis of nourishments; coastal state indicators and driving forces for bergen-egmond, the netherlands. 2021. URL `https://northsearegion.eu/media/18020/national-analysis_bergen_rws-deltares_20210713-final.pdf`.

V. Vuik and W. van Balen. Overstromingskansen voor de nederlandse kust. Technical report, HKV, 2012.

L. Wright and A. Short. Morphodynamic variability of surf zones and beaches: A synthesis. *Marine Geology*, 56(1):93–118, 1984. ISSN 0025-3227. doi:https://doi.org/10.1016/0025-3227(84)90008-2.

# Appendix A

# XBeach parameter settings

```
%%%%%%%%%%%%%%%%%%%%%%%%%%%%%%%%%%%%%%%%%%%%%%%%%%%%%%%%%%%%%%%%%%%%%%%%%%%%%%%%
%%% XBeach parameter settings input file                                     %%%
%%%                                                                          %%%
%%% date:     04-Jul-2018 17:53:28                                           %%%
%%% function: xb_write_params                                                %%%
%%%%%%%%%%%%%%%%%%%%%%%%%%%%%%%%%%%%%%%%%%%%%%%%%%%%%%%%%%%%%%%%%%%%%%%%%%%%%%%%

%%% Flow boundary condition parameters %%%%%%%%%%%%%%%%%%%%%%%%%%%%%%%%%%%%%%%%%

front        = abs_2d
left         = neumann
right        = neumann
back         = abs_2d
single_dir   = 1
cyclic       = 1
epsi         = -1
tidetype     = hybrid

%%% Flow parameters %%%%%%%%%%%%%%%%%%%%%%%%%%%%%%%%%%%%%%%%%%%%%%%%%%%%%%%%%%%%

bedfriction   = manning
nuhfac        = 0

%%% General %%%%%%%%%%%%%%%%%%%%%%%%%%%%%%%%%%%%%%%%%%%%%%%%%%%%%%%%%%%%%%%%%%%%

wavemodel    = surfbeat
bedfriccoef = 0.02
deltahmin     = 0.100000
fixedavaltime = 0
oldTsmin      = 0
oldhmin       = 0

D50          = 0.000250
D90          = 0.000300

%%% Grid parameters %%%%%%%%%%%%%%%%%%%%%%%%%%%%%%%%%%%%%%%%%%%%%%%%%%%%%%%%%%%%
```

```
depfile      = bed.dep
posdwn       = -1
nx           = 377
ny           = 738
vardx        = 1
xfile        = x.grd
yfile        = y.grd
thetamin     = -90
thetamax     = 90
thetanaut    = 0
dtheta_s     = 5

%%% Model time %%%%%%%%%%%%%%%%%%%%%%%%%%%%%%%%%%%%%%%%%%%%%%%%%%%%%%%%%%%%%%%%%

tstop        = 82800

%%% Physical processes %%%%%%%%%%%%%%%%%%%%%%%%%%%%%%%%%%%%%%%%%%%%%%%%%%%%%%%%%

sedtrans     = 1
morphology   = 1

%%% Morphology parameters %%%%%%%%%%%%%%%%%%%%%%%%%%%%%%%%%%%%%%%%%%%%%%%%%%%%%%

morstart     = 1800
wetslp       = 0.18
morfac = 4
struct = 1
ne_layer = ne_layer.dep

%%% Sediment transport parameters %%%%%%%%%%%%%%%%%%%%%%%%%%%%%%%%%%%%%%%%%%%%%%

facSk        = 0.15
facAs        = 0.25

%%% MPI parameters %%%%%%%%%%%%%%%%%%%%%%%%%%%%%%%%%%%%%%%%%%%%%%%%%%%%%%%%%%%%%

mpiboundary = x

%%% Tide boundary conditions %%%%%%%%%%%%%%%%%%%%%%%%%%%%%%%%%%%%%%%%%%%%%%%%%%%

zs0file      = tide_Corrie_hourly.txt
```

```
tideloc      = 1

%%% Wave boundary condition parameters %%%%%%%%%%%%%%%%%%%%%%%%%%%%%%%%%%%%%%%%%

wbctype       = jonstable

%%% Wave-spectrum boundary condition parameters %%%%%%%%%%%%%%%%%%%%%%%%%%%%%%%%

bcfile       = jonswap_Corrie_hourly.txt
random       = 1

%%% Discharge boundary conditions %%%%%%%%%%%%%%%%%%%%%%%%%%%%%%%%%%%%%%%%%%%%%%

beta         = 0.08

%%% Wave breaking parameters %%%%%%%%%%%%%%%%%%%%%%%%%%%%%%%%%%%%%%%%%%%%%%%%%%%

break        = roelvink_daly
alpha        = 1.38
gamma        = 0.46
gamma2       = 0.34

%%% Output variables %%%%%%%%%%%%%%%%%%%%%%%%%%%%%%%%%%%%%%%%%%%%%%%%%%%%%%%%%%%

outputformat = netcdf
tintm        = 3600
tint         = 1800
tintp        = 1
tstart       = 0

nglobalvar   = 6
zs
zb
H
u
v
thetamean

nmeanvar     = 10
hh
zs1
ue
```

```
ve
uu
vv
H
zs
Sutot
Svtot

npointvar   = 5
zs
zb
H
uu
vv

npoints      = 18
2157.8284 4889.41020280401
2148.8529 4392.86999741868
2167.4606 3893.35649279124
2161.9204 3391.86078866907
2166.4231 2891.22306295574
2191.9798 2385.62983850558
2229.9798 1886.11633387815
2226.9798 1383.49640867008
2179.9301 883.982904042648
2240.9798 4889.41020280401
2245.9798 4392.86999741868
2254.9798 3893.35649279124
2272.9798 3391.86078866907
2275.9798 2891.22306295574
2284.9798 2385.62983850558
2297.9798 1886.11633387815
2302.9798 1383.49640867008
2272.9798 883.982904042648
```

# Appendix B

# Bathymetries

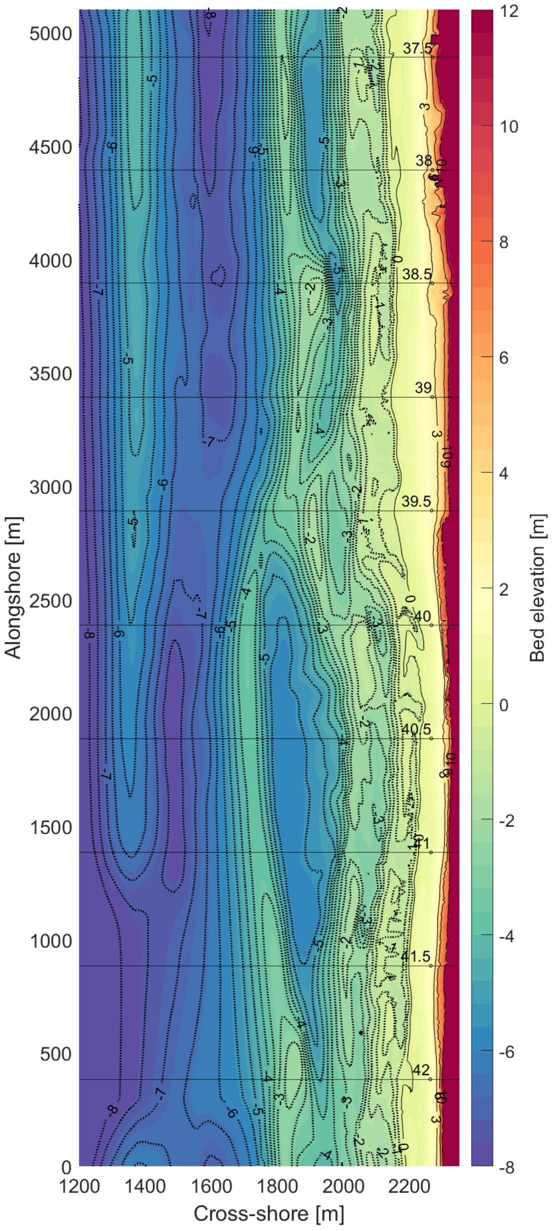

**(a)** March 2020

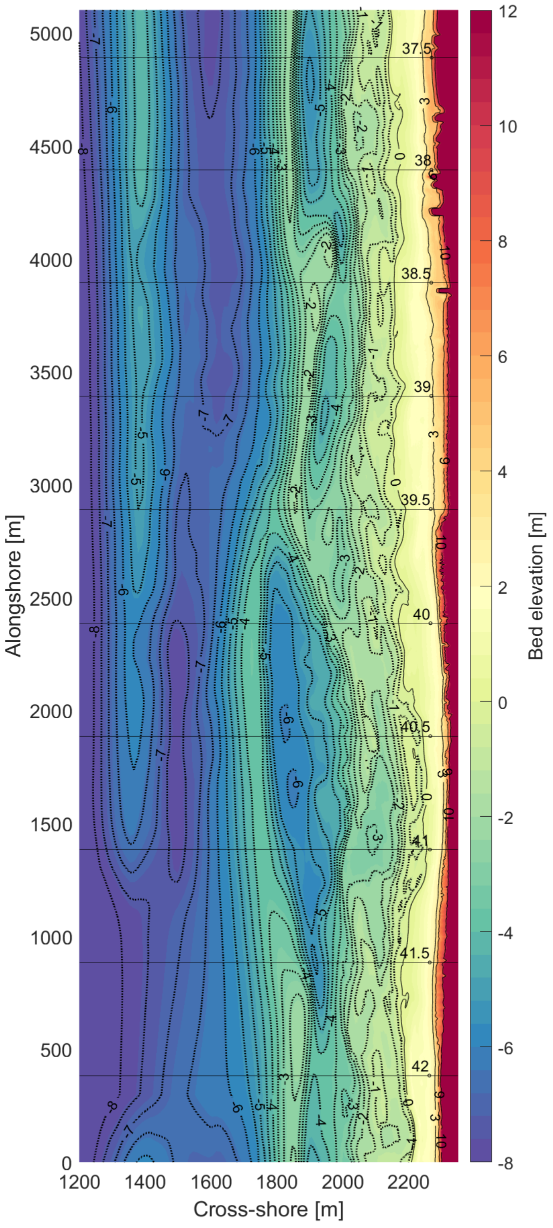

**(b)** October 2020

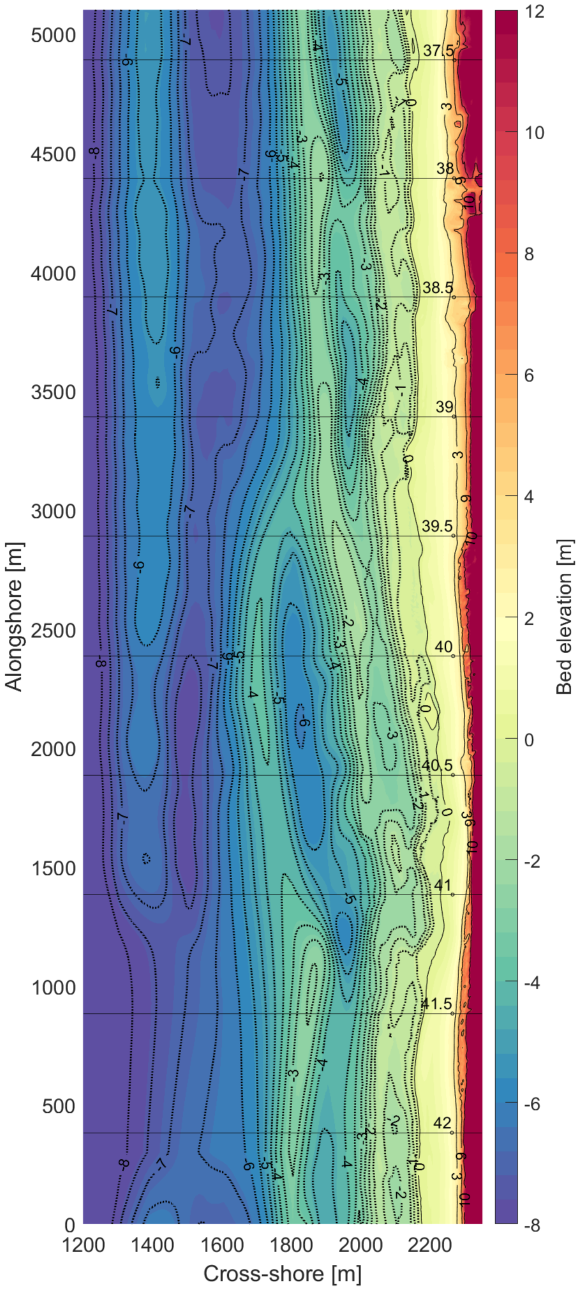

**(c)** March 2021

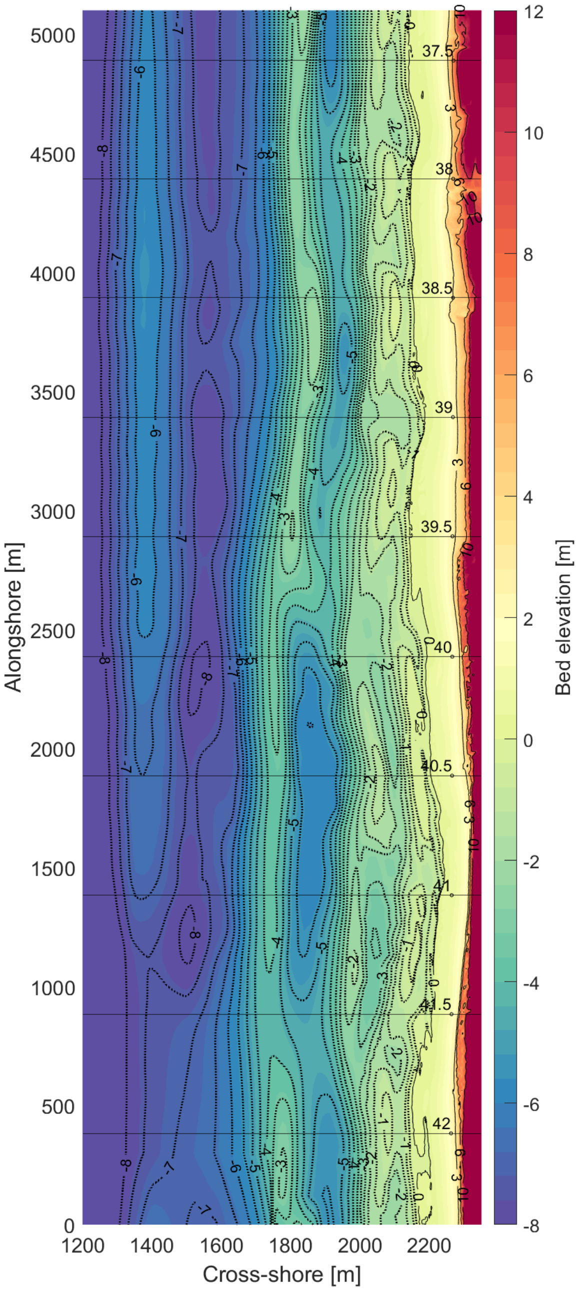

**(d)** March 2022

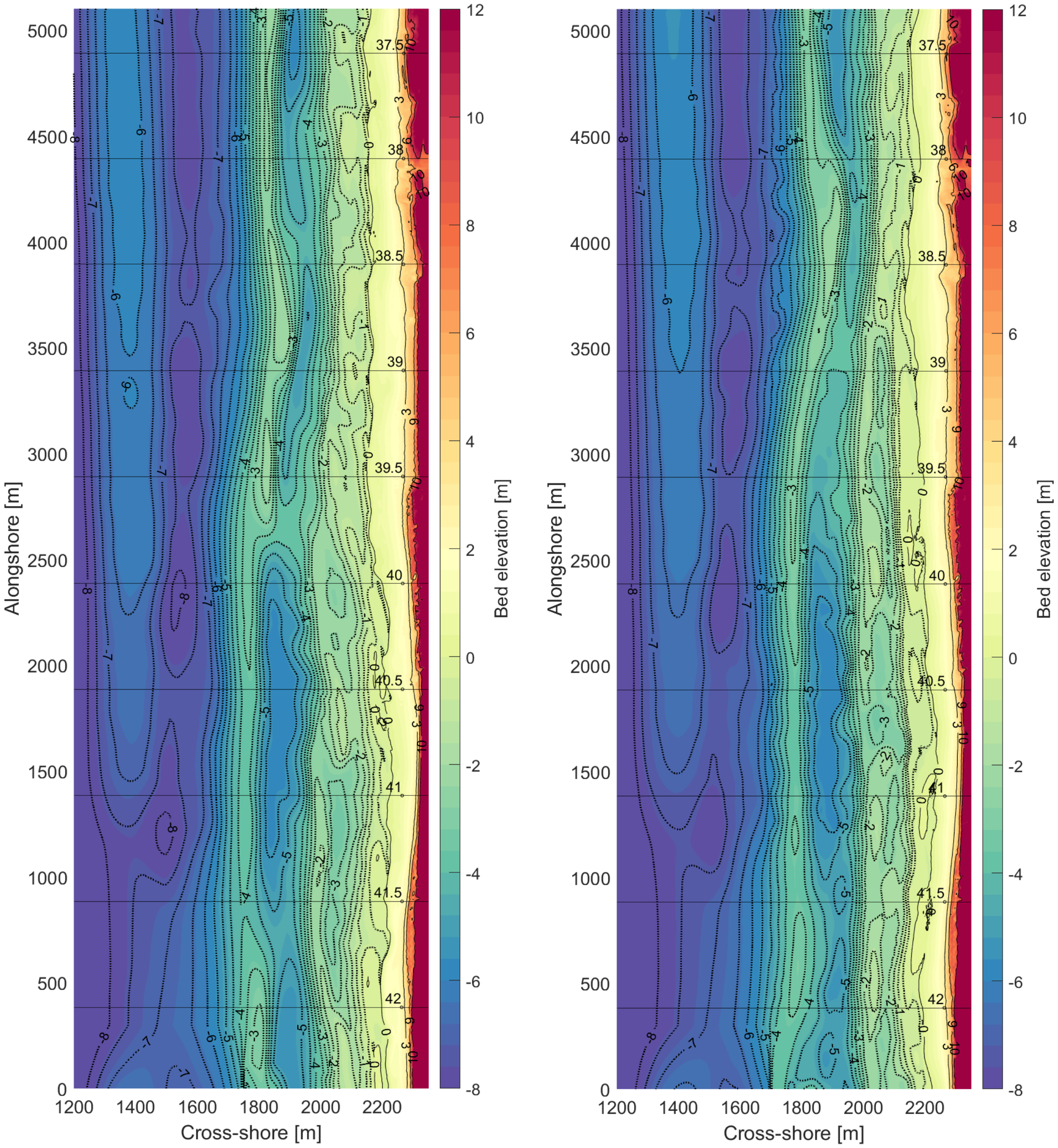

**(e)** October 2022 **(f)** October 2023

**Figure B.1:** Bathymetric data for various dates.

# Appendix C

# Cross sections

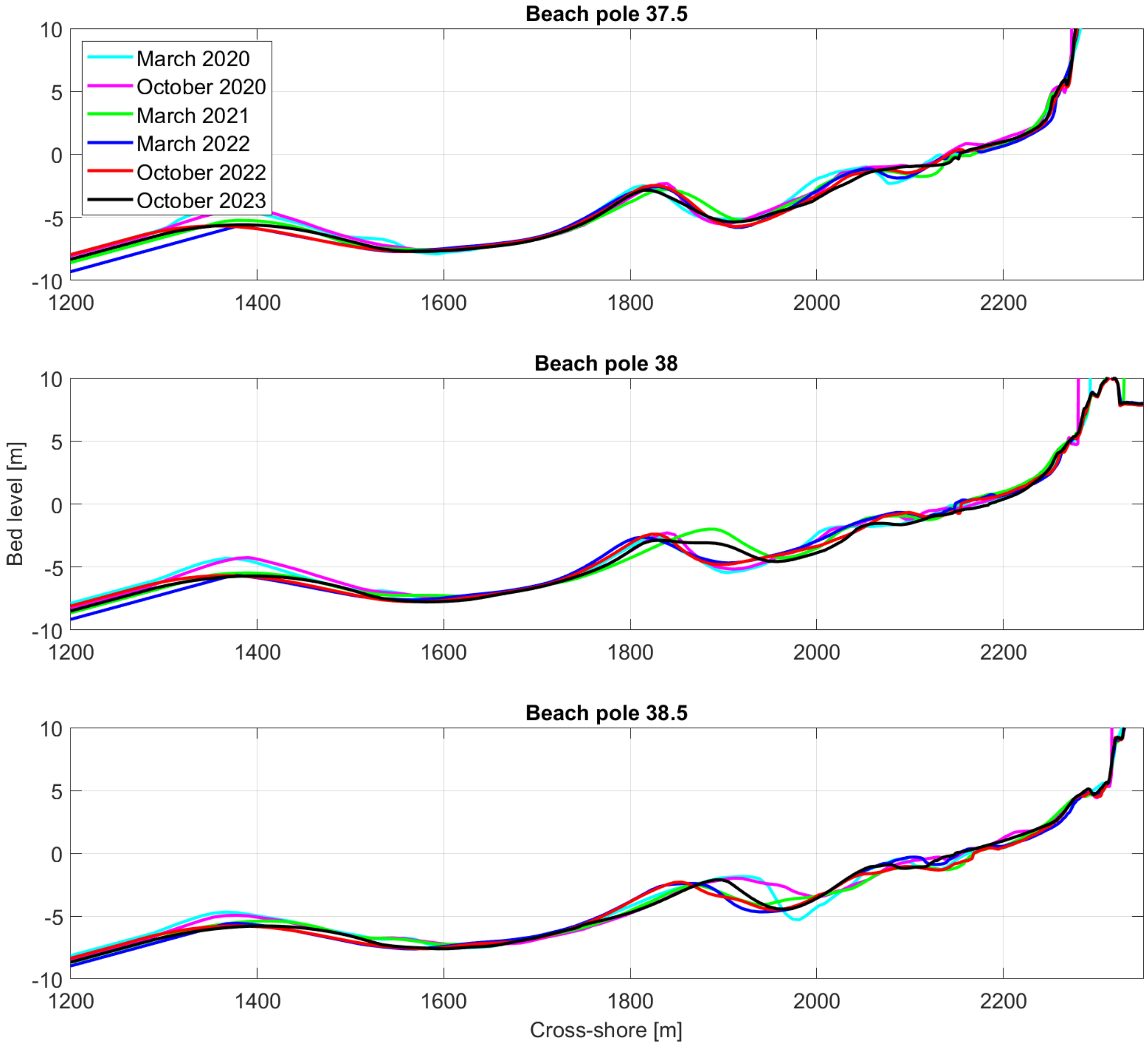

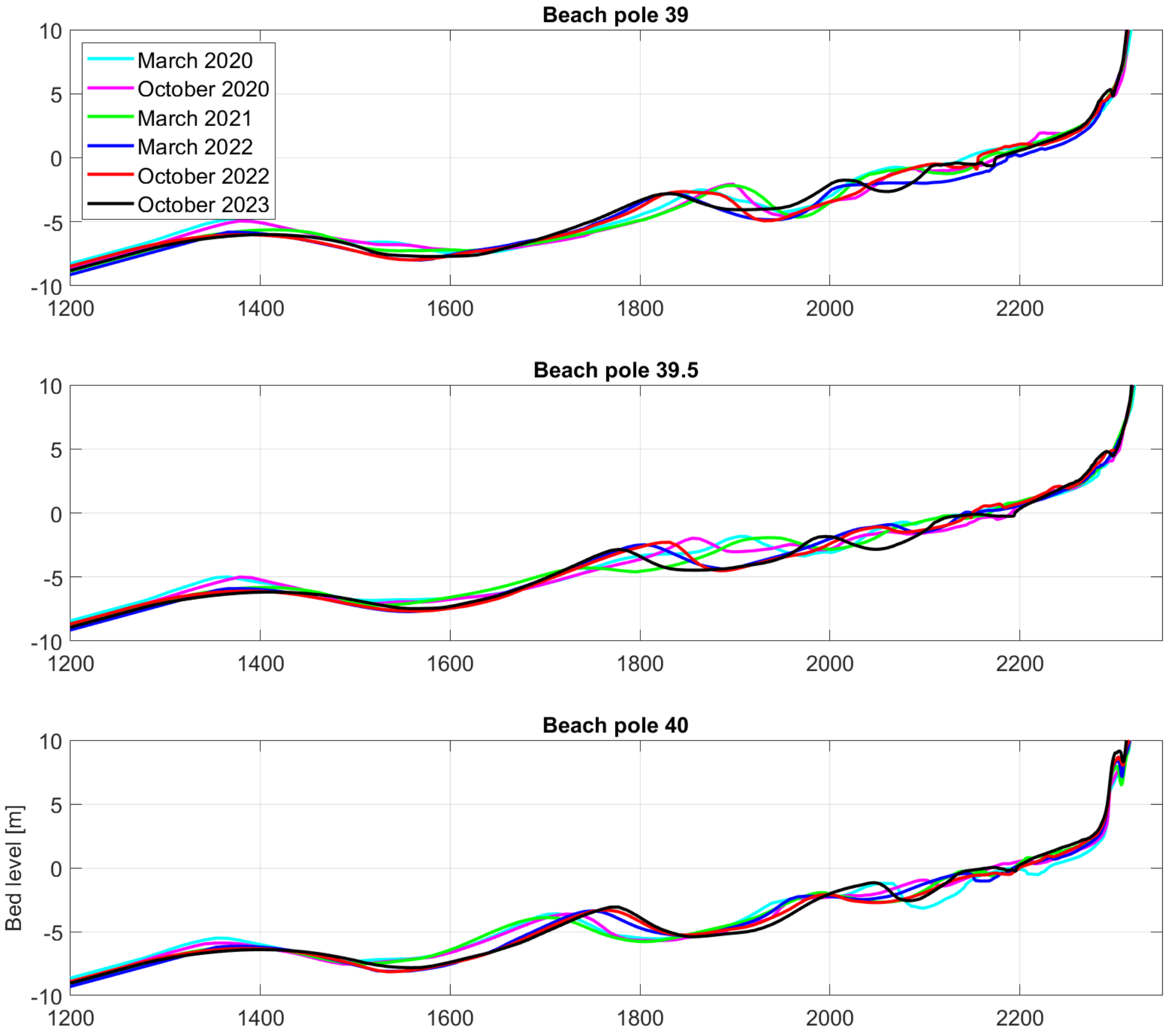
Beach pole 39
March 2020
October 2020
March 2021
March 2022
October 2022
October 2023
Beach pole 39.5
Beach pole 40
Bed level [m]
10
5
0
-5
-10
1200
1400
1600
1800
2000
2200

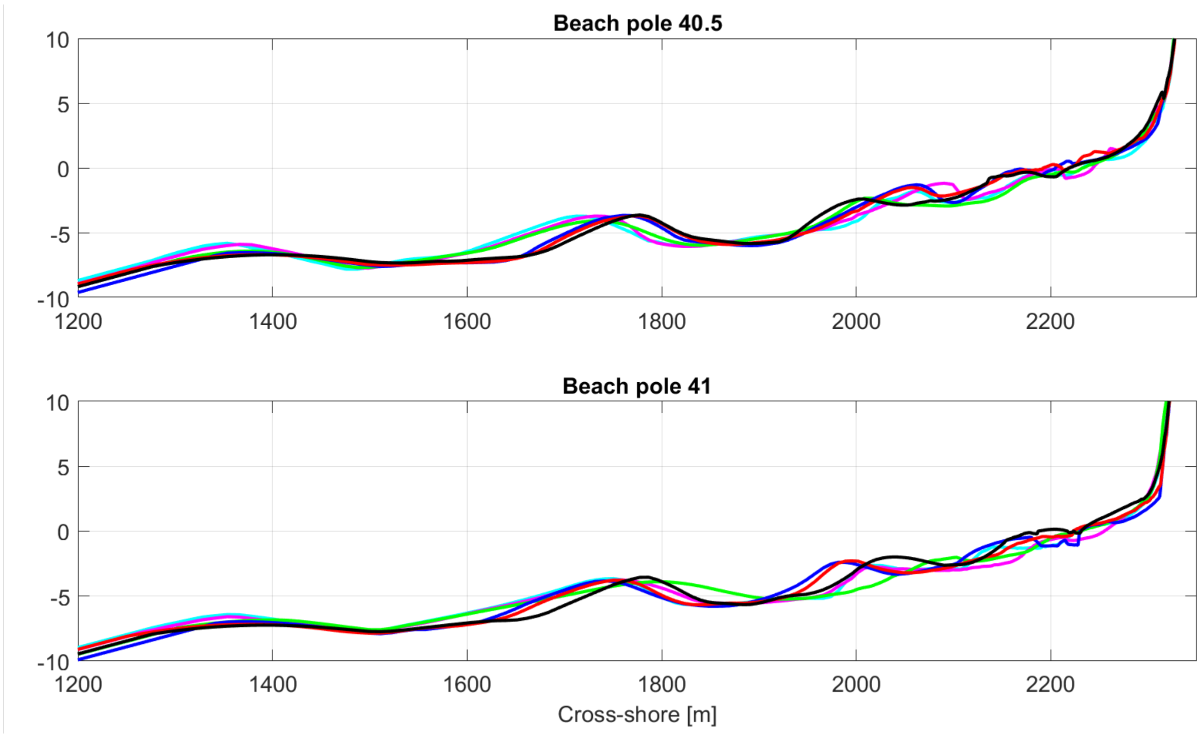
Beach pole 40.5
Beach pole 41
10
5
0
-5
-10
1200
1400
1600
1800
2000
2200
Cross-shore [m]

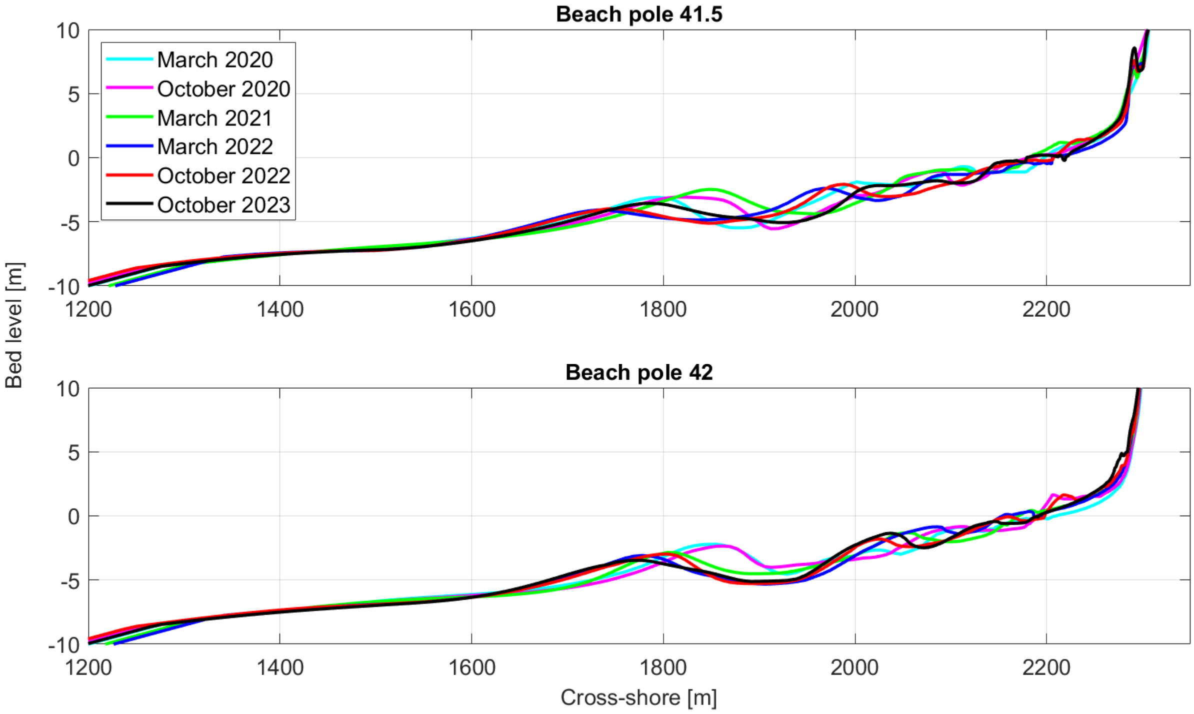

**Figure C.1:** Cross-sections at the beach poles for different dates.

# Appendix D

# Bed level differences between bathymetries

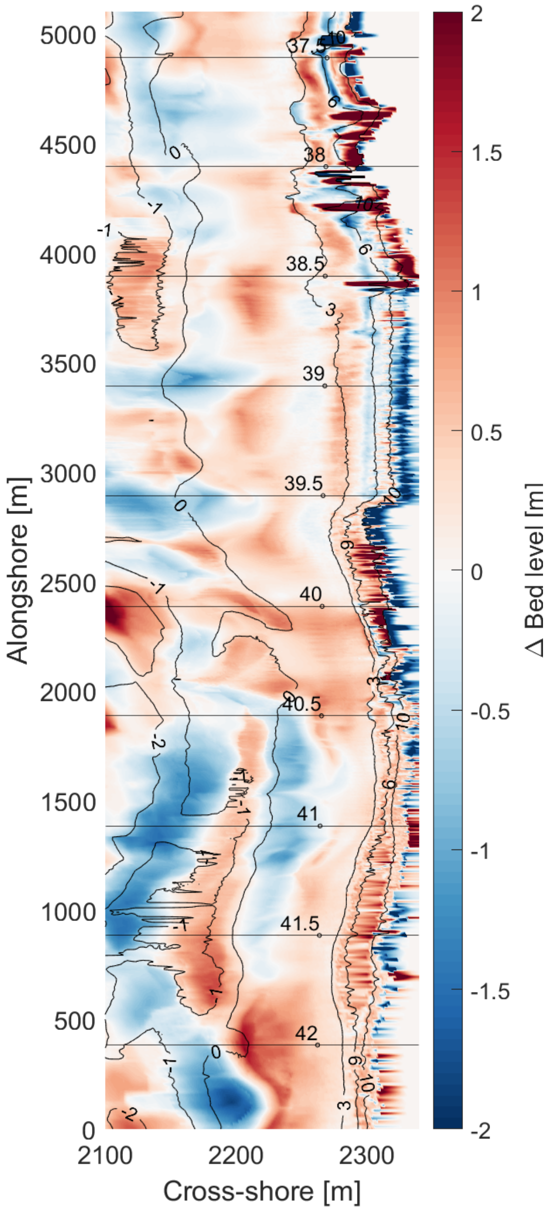

**(a)** March 2020 and October 2020

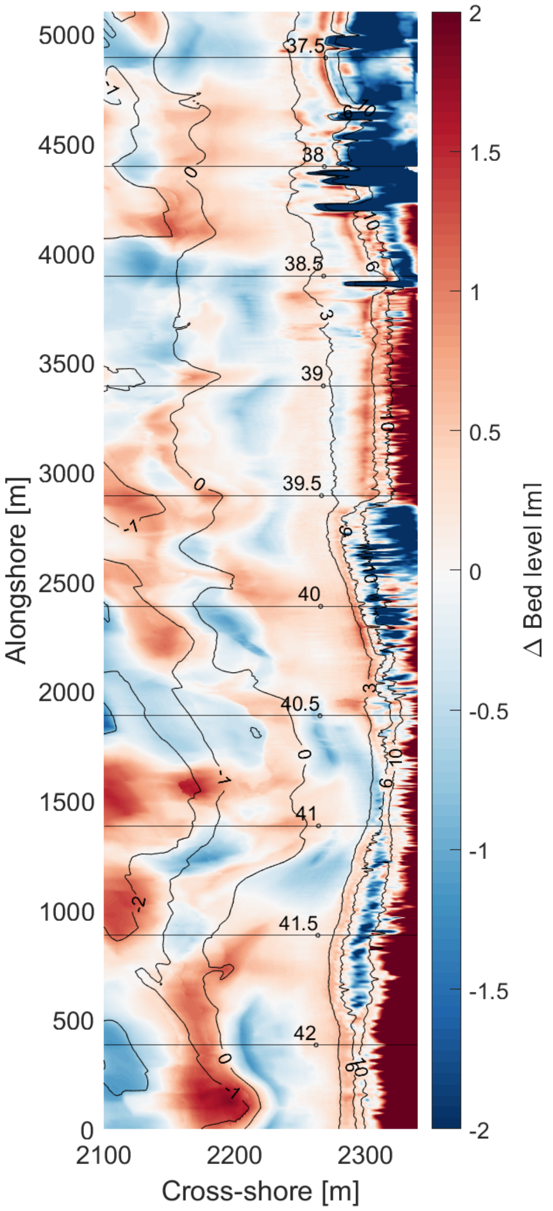

**(b)** October 2020 and March 2021

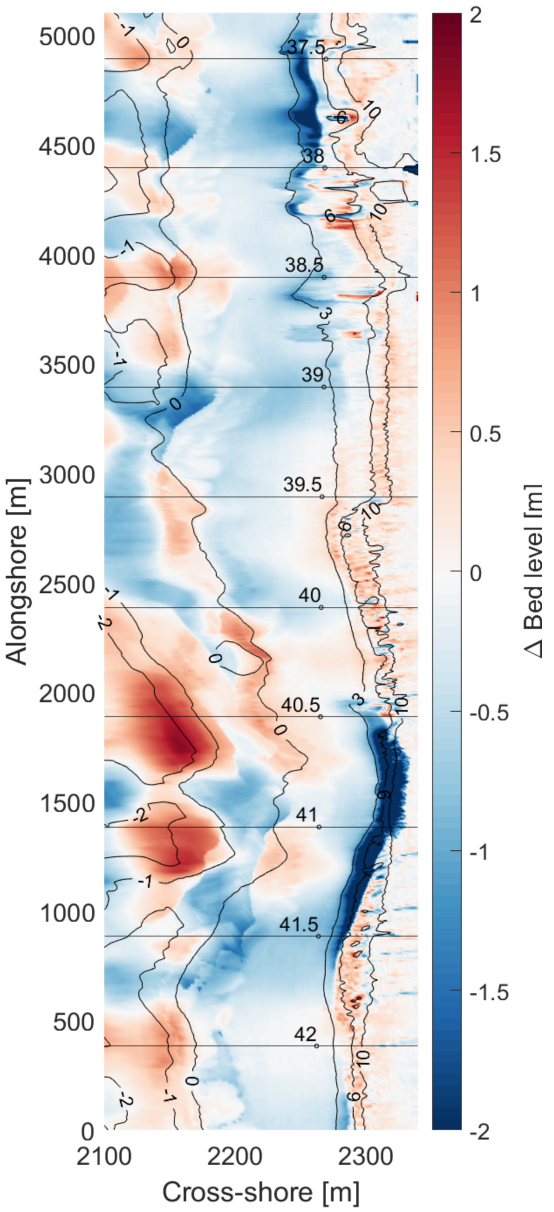

(c) March 2021 and March 2022

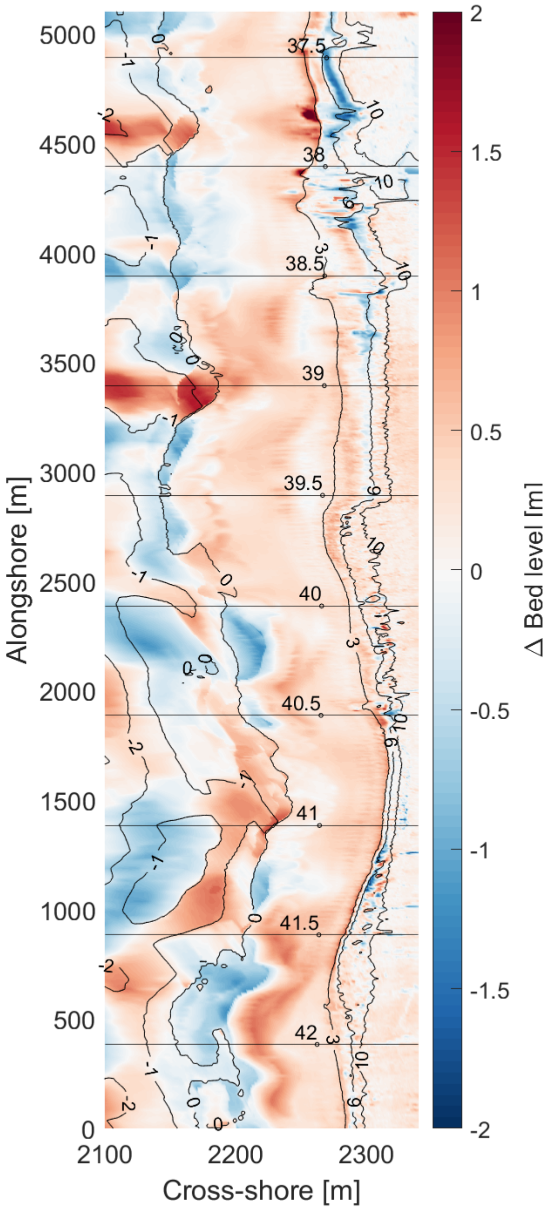

(d) March 2022 and October 2022

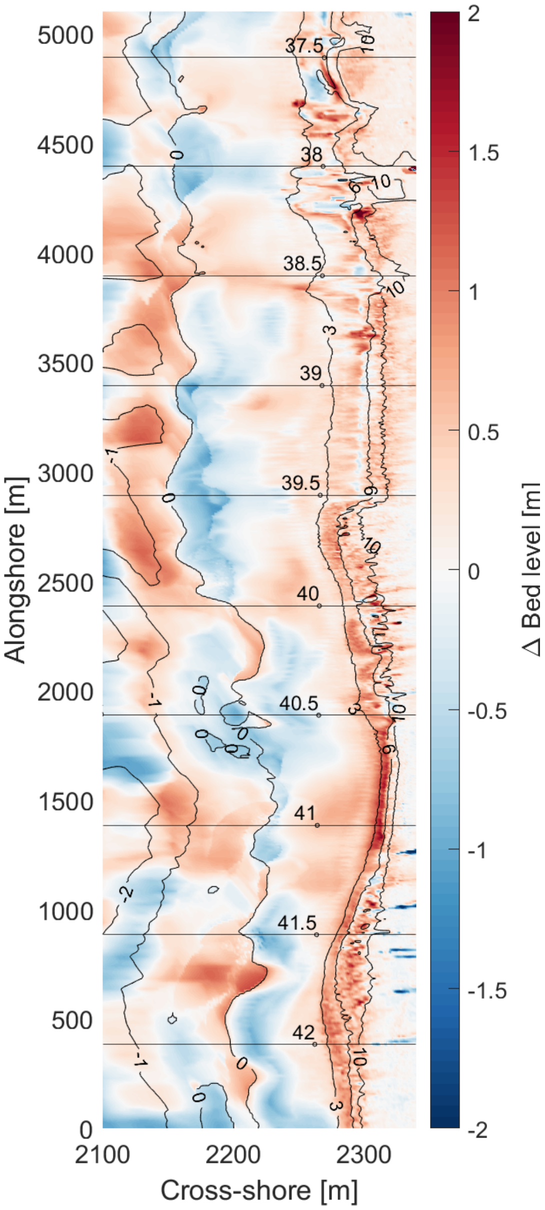

**(e)** October 2022 and October 2023

**Figure D.1:** Observed bed level difference beach and dune. The black solid lines are contour lines with 0 - 3m as beach and 3 - 10m as dune.

# Appendix E

# Nourishment designs

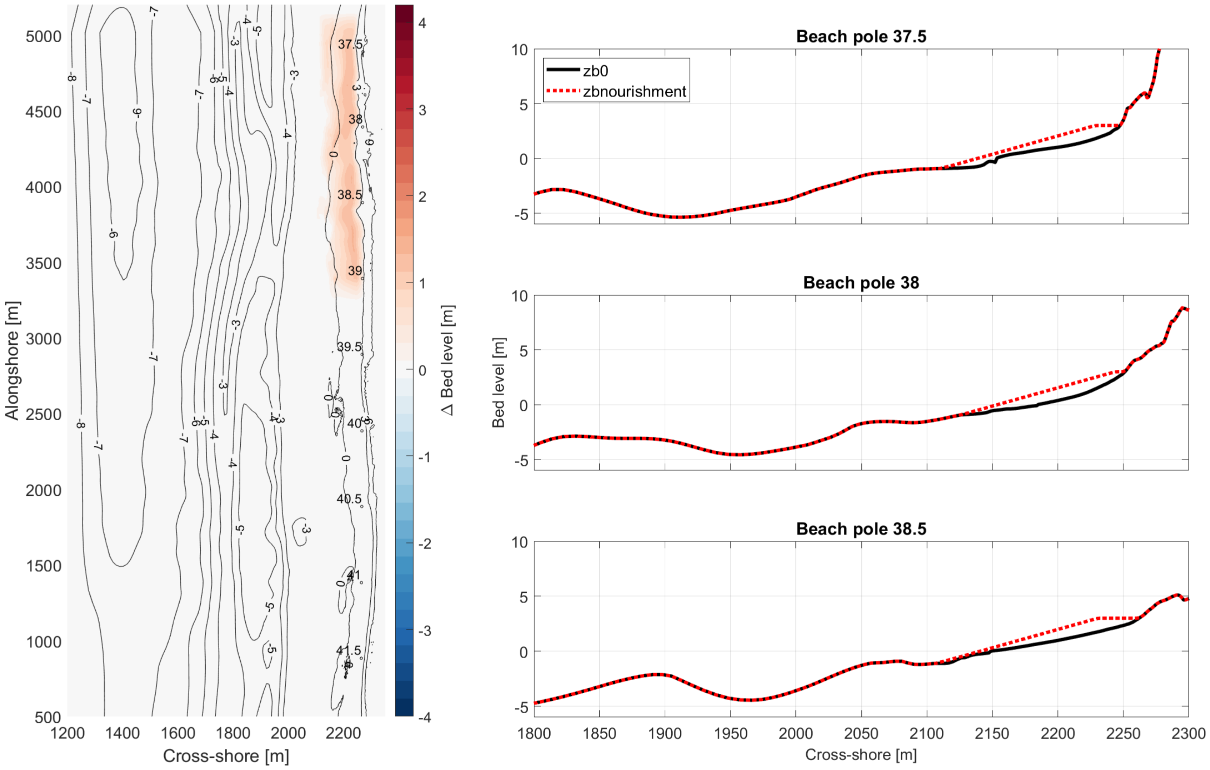

**(a)** Nourishment location

**(b)** Cross-sections

**Figure E.1:** Beach nourishment at 0 - 3m NAP with a volume of $100\text{m}^3/\text{m}$.

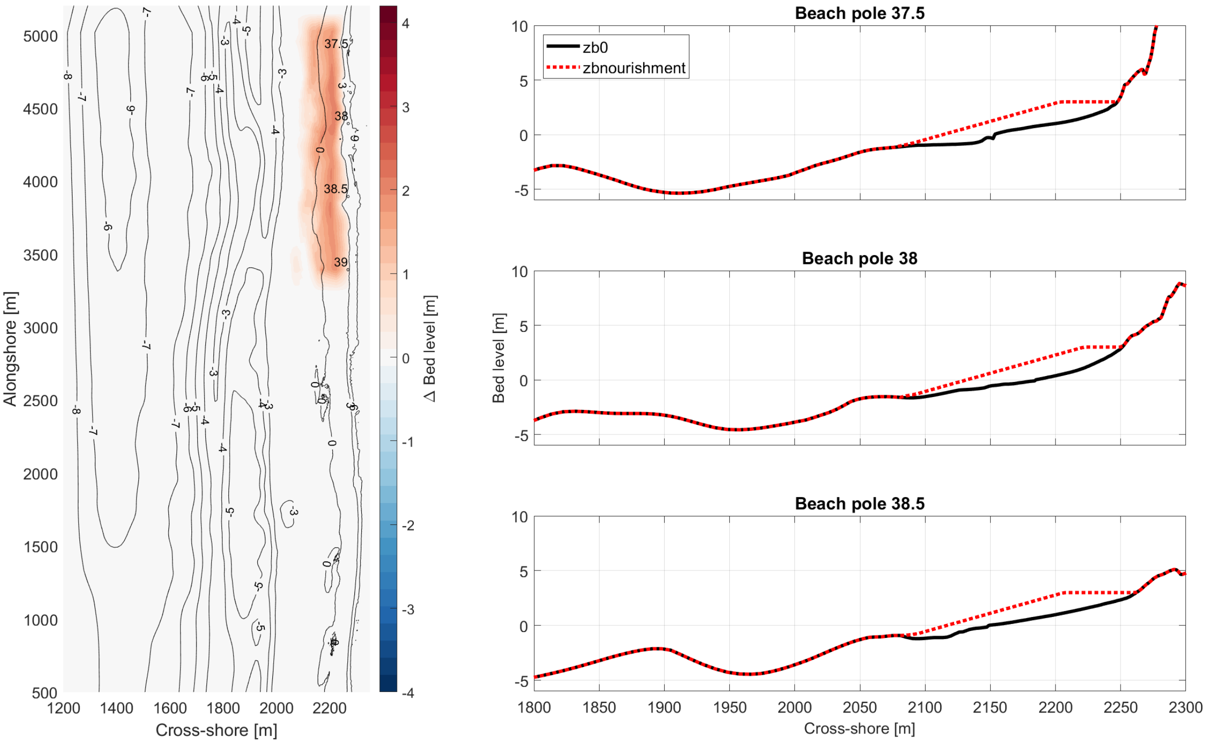

**(a)** Nourishment location

**(b)** Cross-sections

**Figure E.2:** Beach nourishment at 0 - 3m NAP with a volume of 200m$^3$/m.

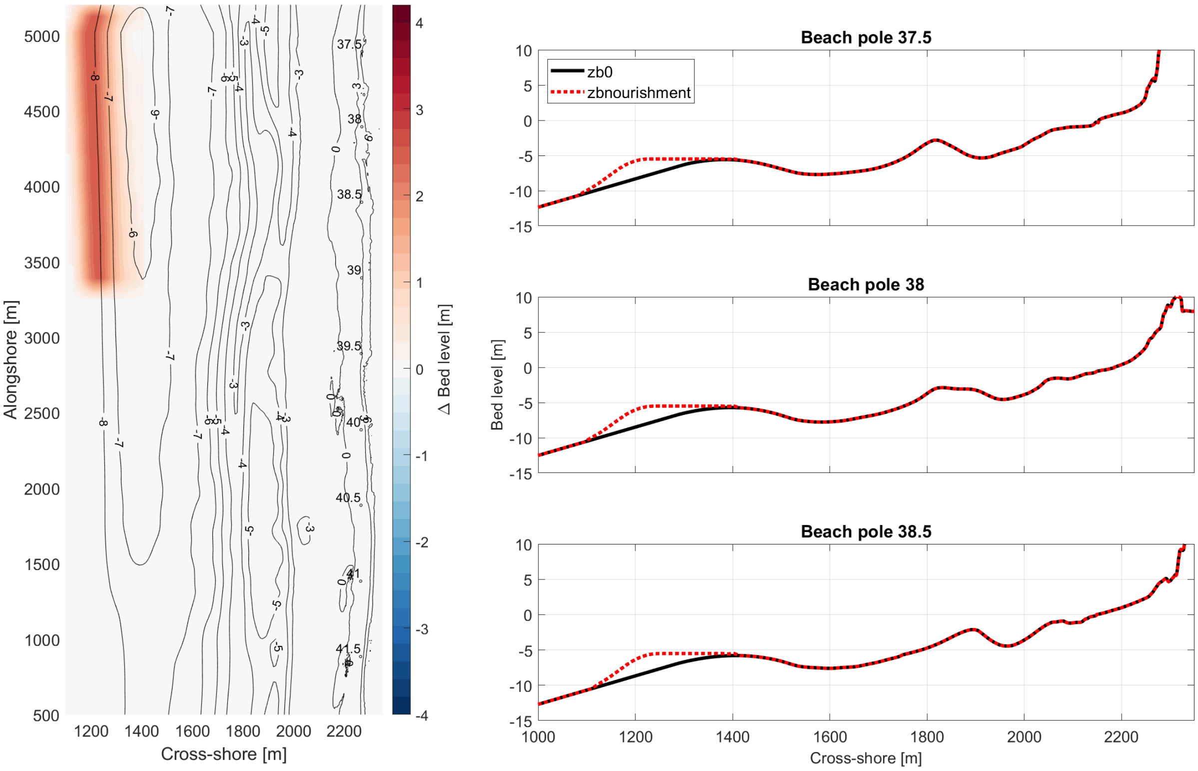

**(a)** Nourishment location

**(b)** Cross-sections

**Figure E.3:** Shoreface nourishment at -5.5m NAP with a volume of 375m$^3$/m.

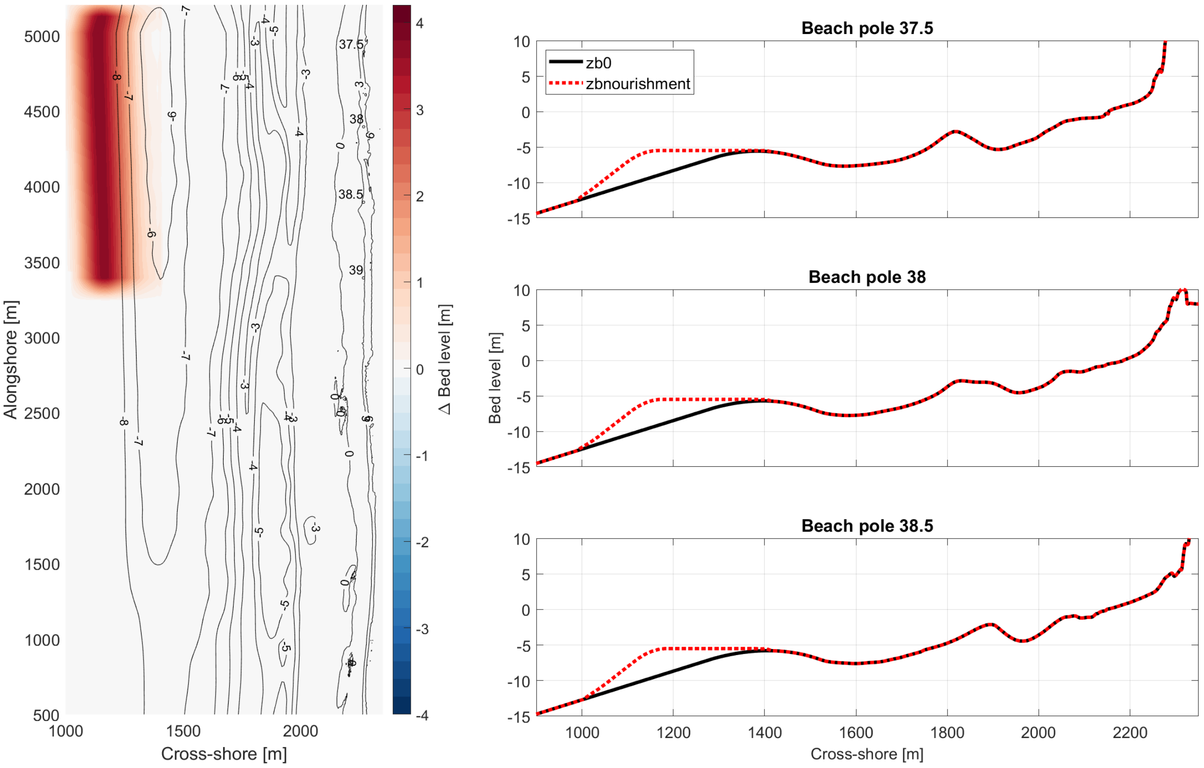

**(a)** Nourishment location

**(b)** Cross-sections

**Figure E.4:** Shoreface nourishment at -5.5m NAP with a volume of 750m$^3$/m.

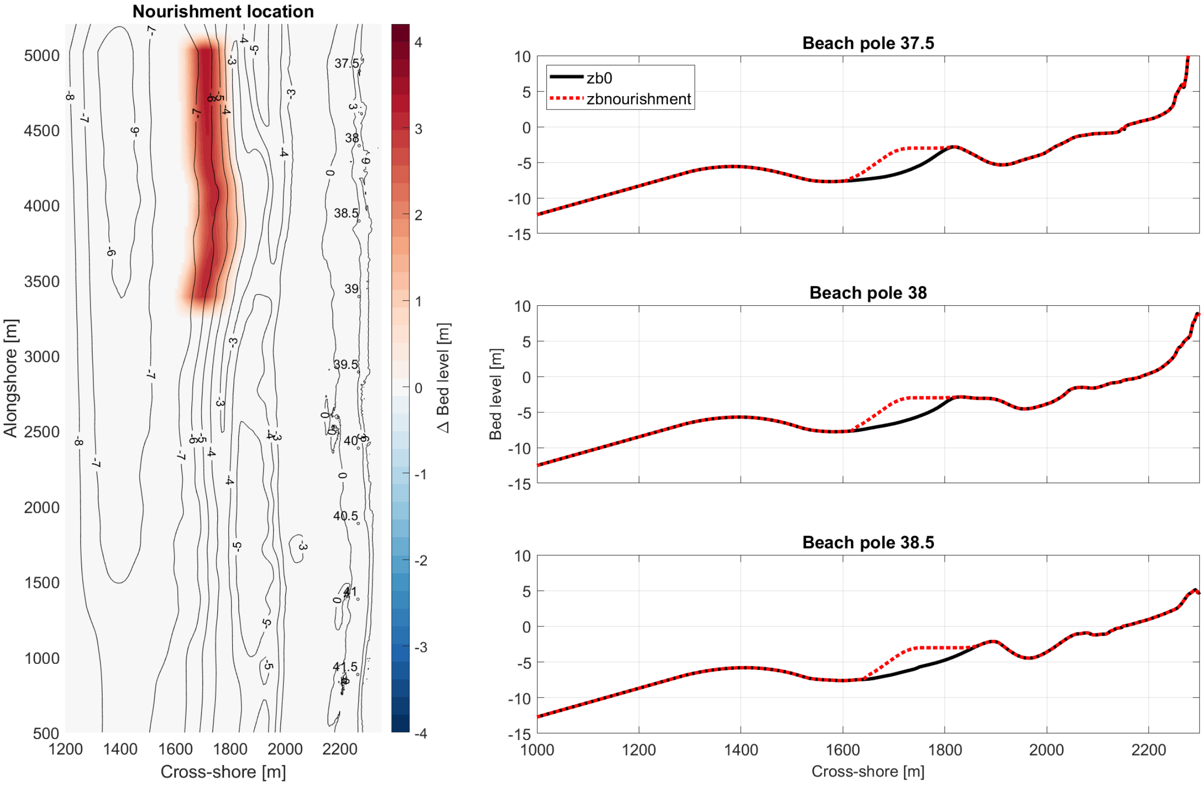

**(a)** Nourishment location

**(b)** Cross-sections

**Figure E.5:** Shoreface nourishment at -3m NAP with a volume of 375m$^3$/m.

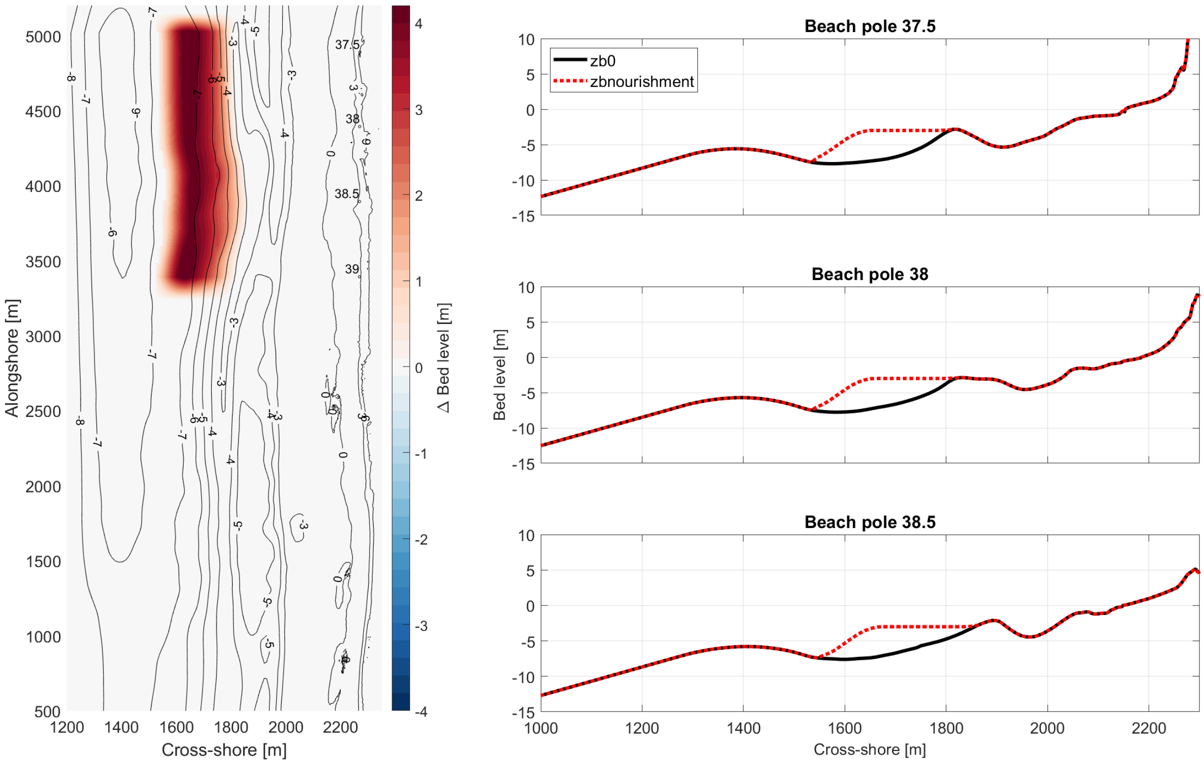

**(a)** Nourishment location

**(b)** Cross-sections

**Figure E.6:** Shoreface nourishment at -3m NAP with a volume of 750m$^3$/m.

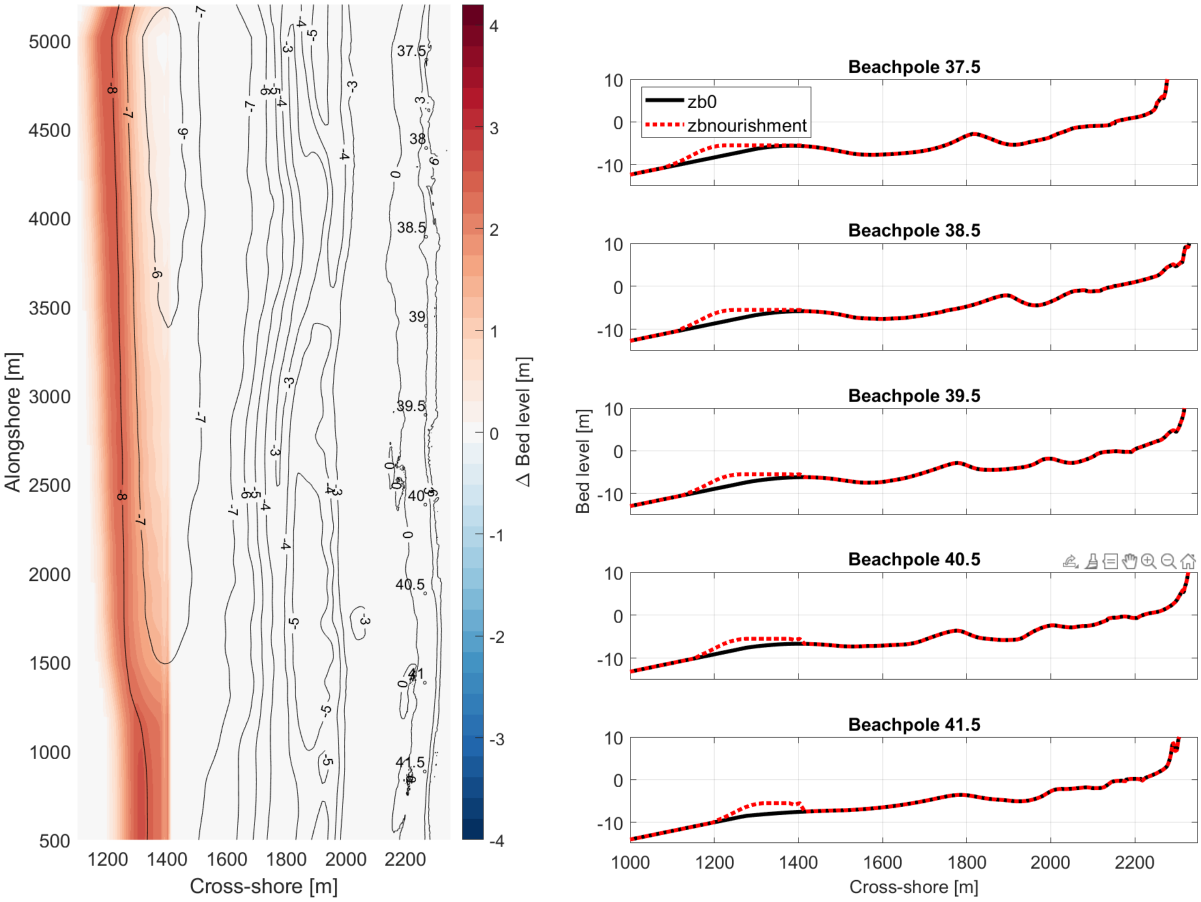

**(a)** Nourishment location

**(b)** Cross-sections

**Figure E.7:** Shoreface nourishment at -5.5m NAP with a volume of 375m$^3$/m over the entire length of the coast.

# Appendix F

# XBeach validation

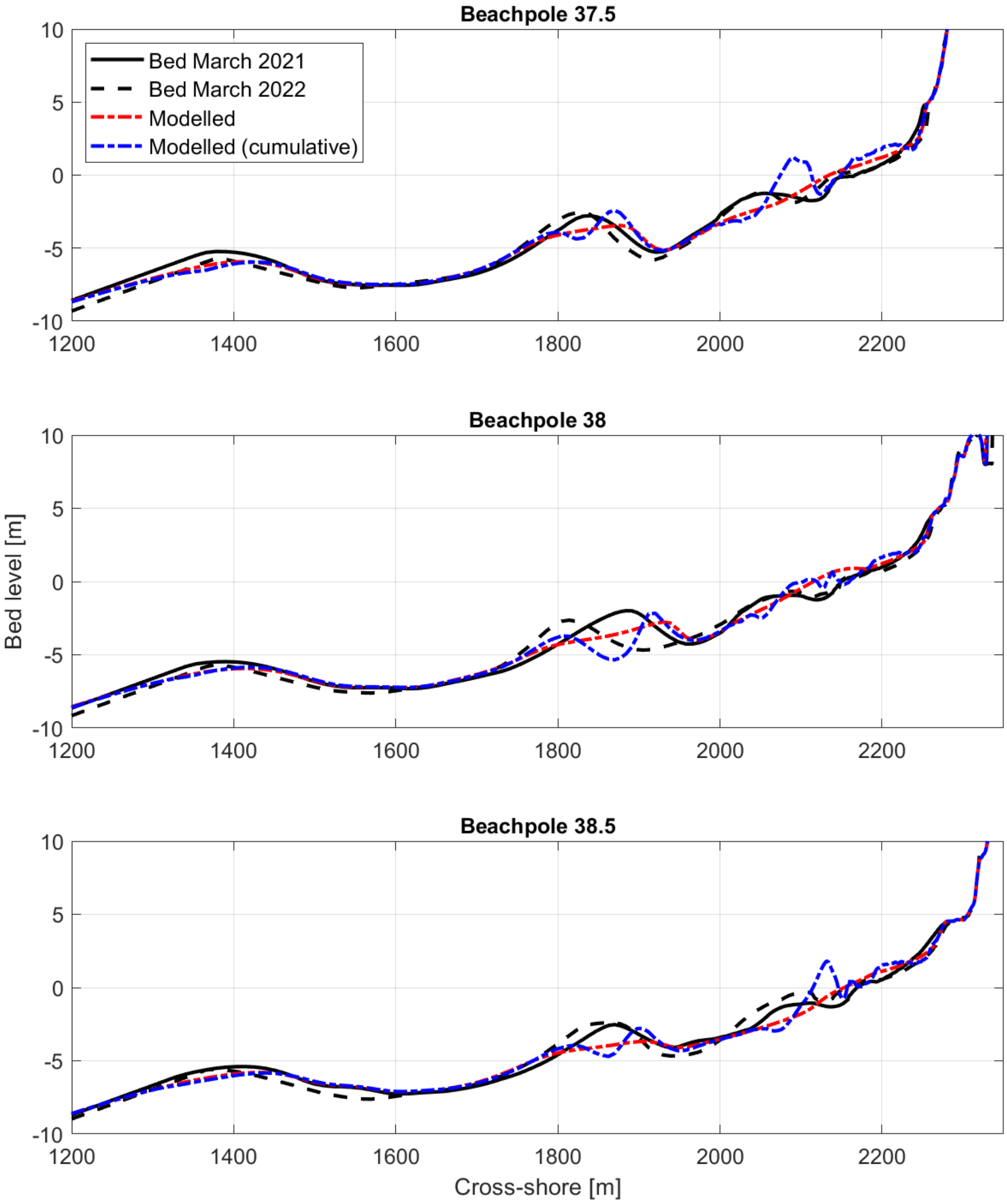

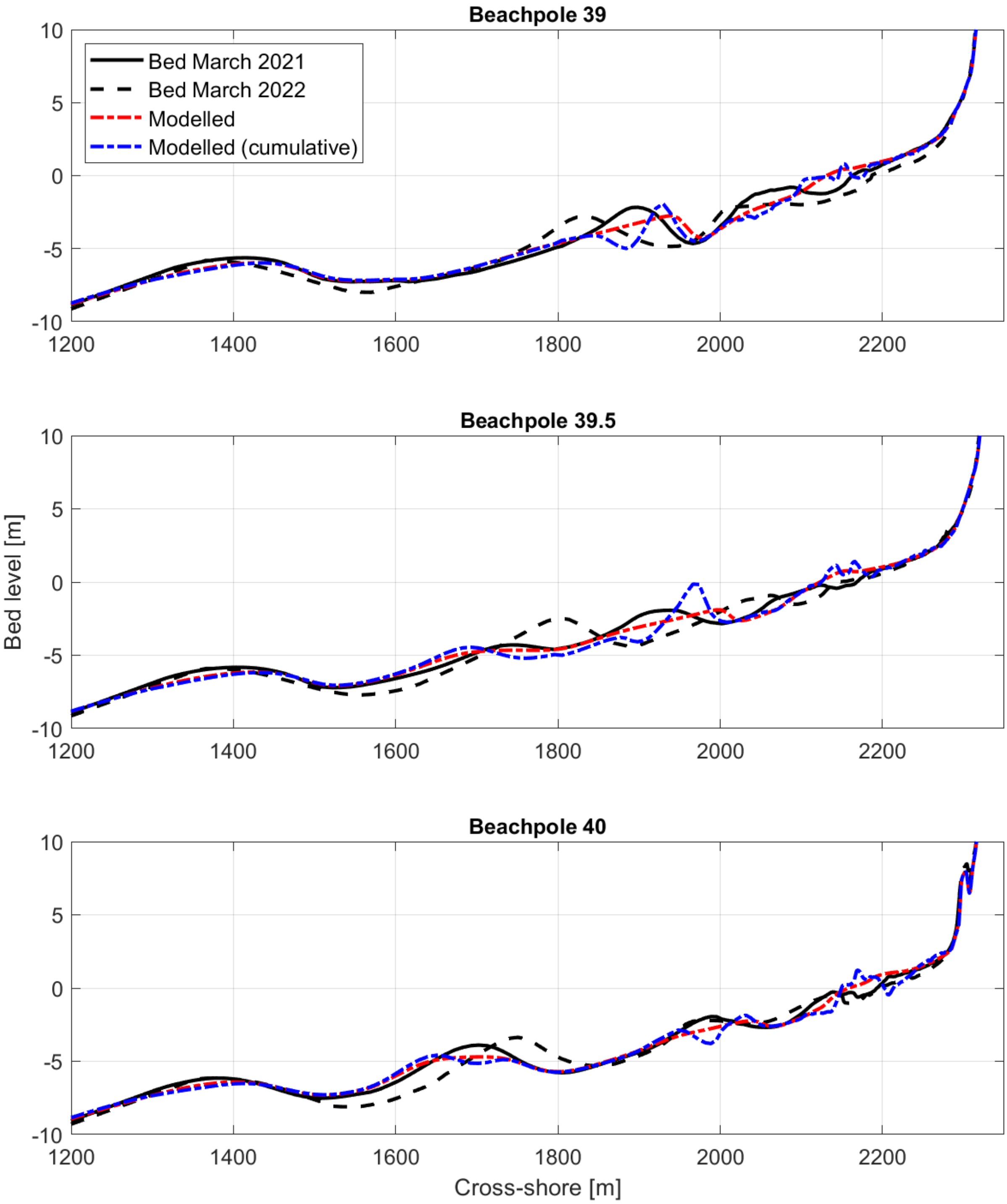
Beachpole 39
Bed March 2021
Bed March 2022
Modelled
Modelled (cumulative)
Beachpole 39.5
Beachpole 40
Bed level [m]
Cross-shore [m]
10
5
0
-5
-10
1200
1400
1600
1800
2000
2200

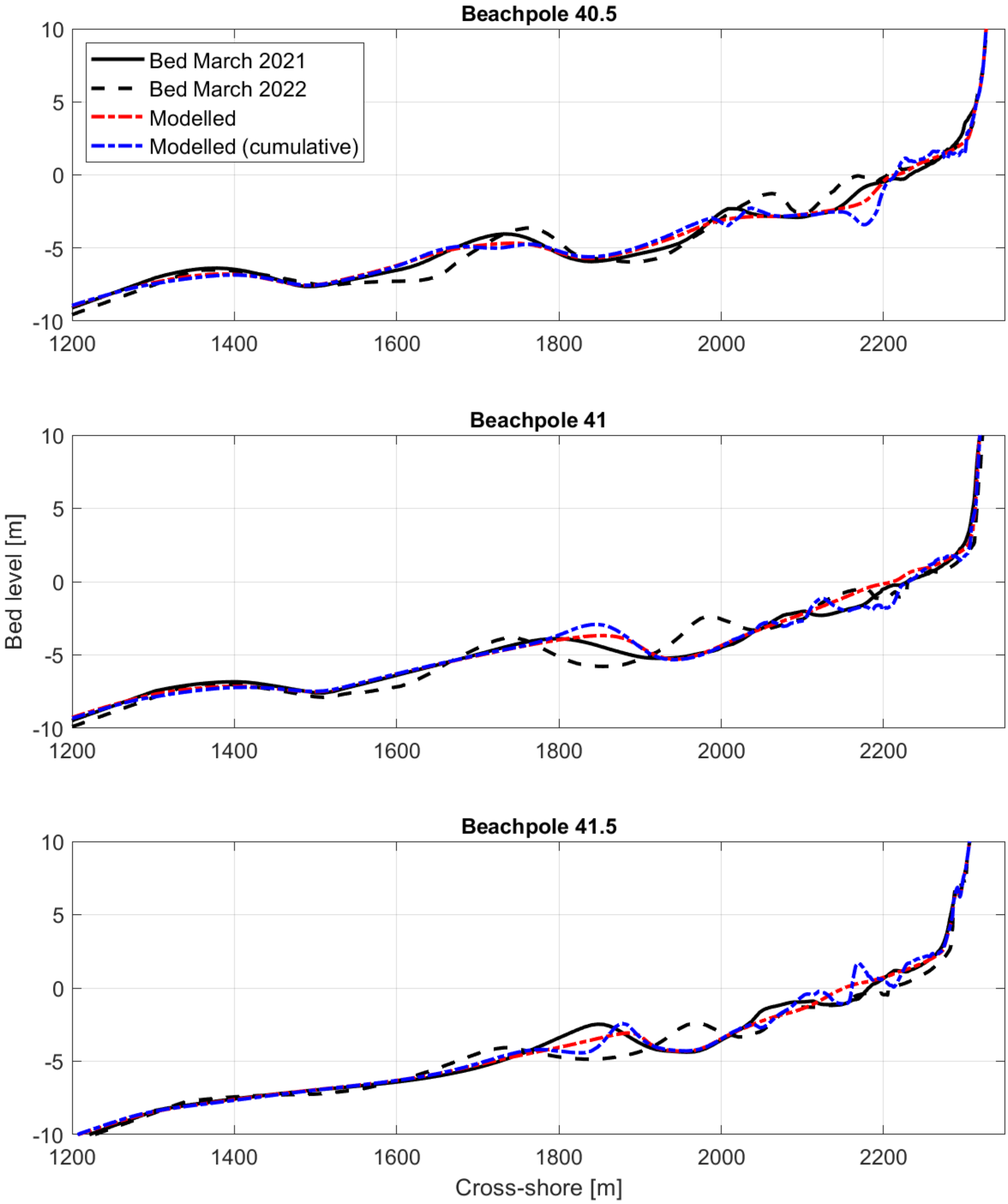

**Figure F.1:** Cross-sections at the beach poles for observed and modelled results.

# Appendix G

# 1D test runs

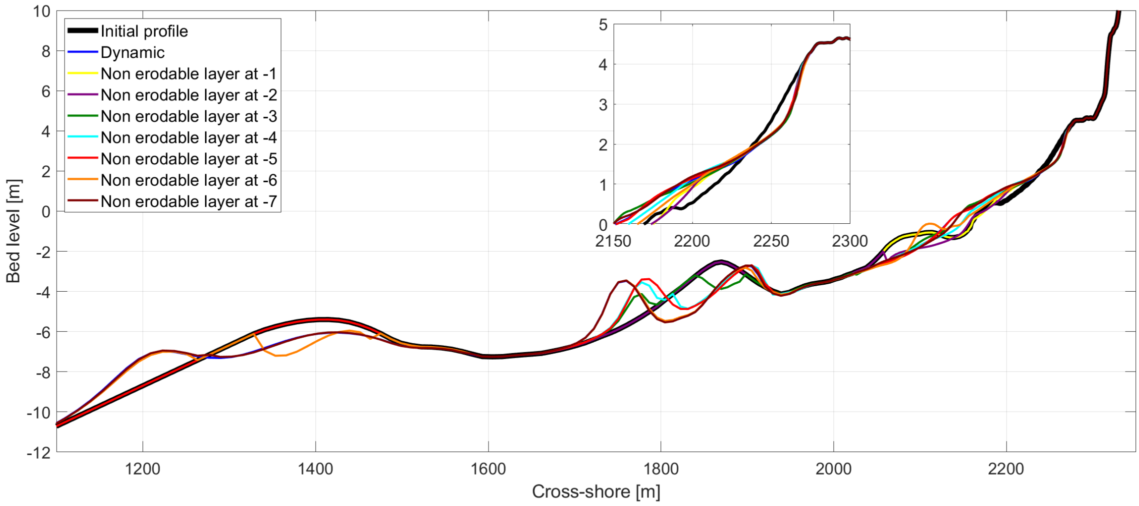

**(a)** Run with the bathymetry of March 2021 and simulated sequence 3.7. The plot shows the bed level at the end of the simulation for different positions of height for the non-erodible layer (below this height the bed is fixed.

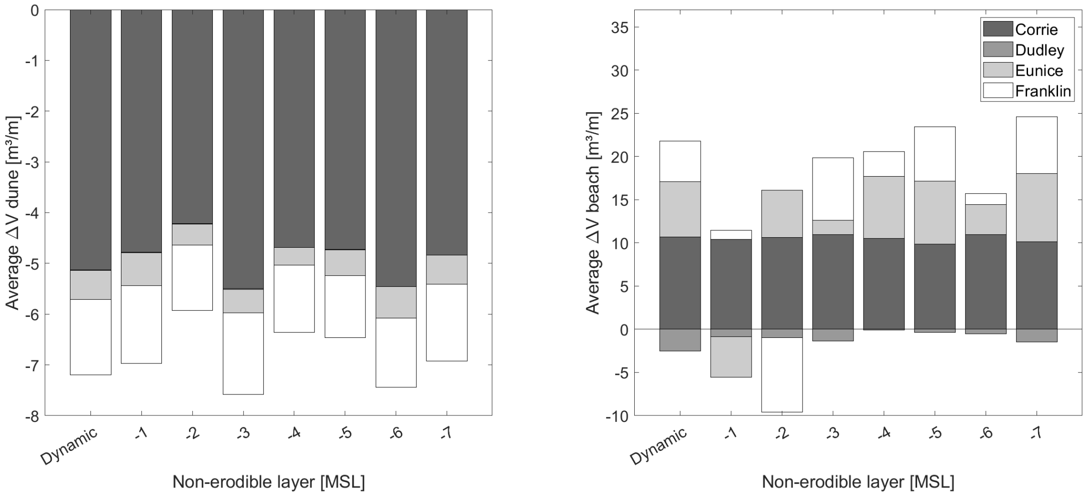

**(b)** Dune and beach volume change for the simulation with different levels of non-erodible layers.

**Figure G.1:** Results 1D run beach at pole 38.5.

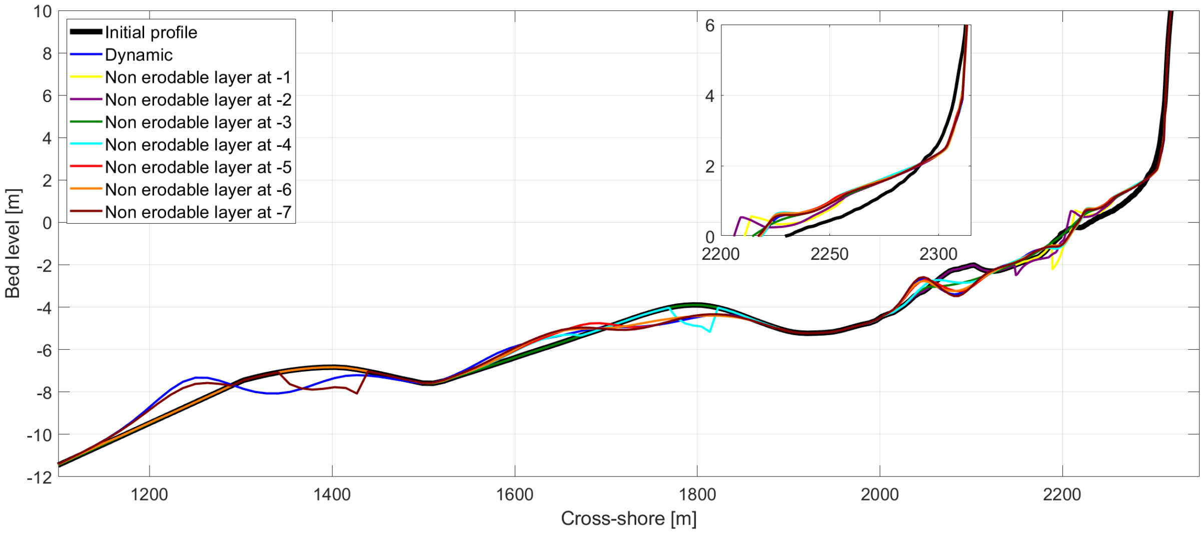

**(a)** Run with the bathymetry of March 2021 and simulated sequence 3.7. The plot shows the bed level at the end of the simulation for different positions of height for the non-erodible layer (below this height the bed is fixed.

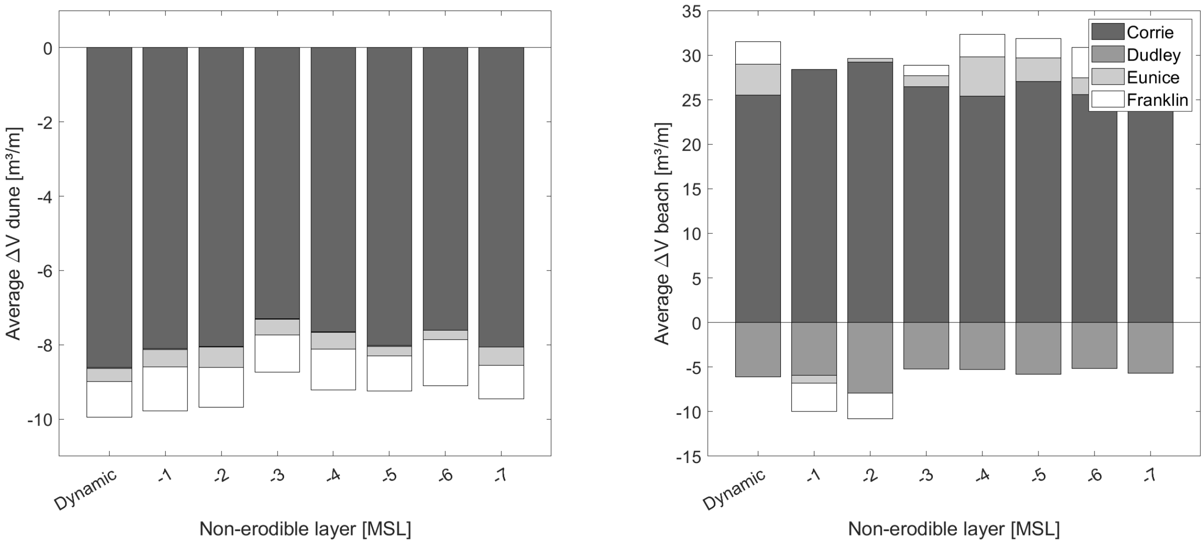

**(b)** Dune and beach volume change for the simulation with different levels of non-erodible layers.

**Figure G.2:** Results 1D run beach at pole 41.

# Appendix H

# XBeach output

### Bed level difference

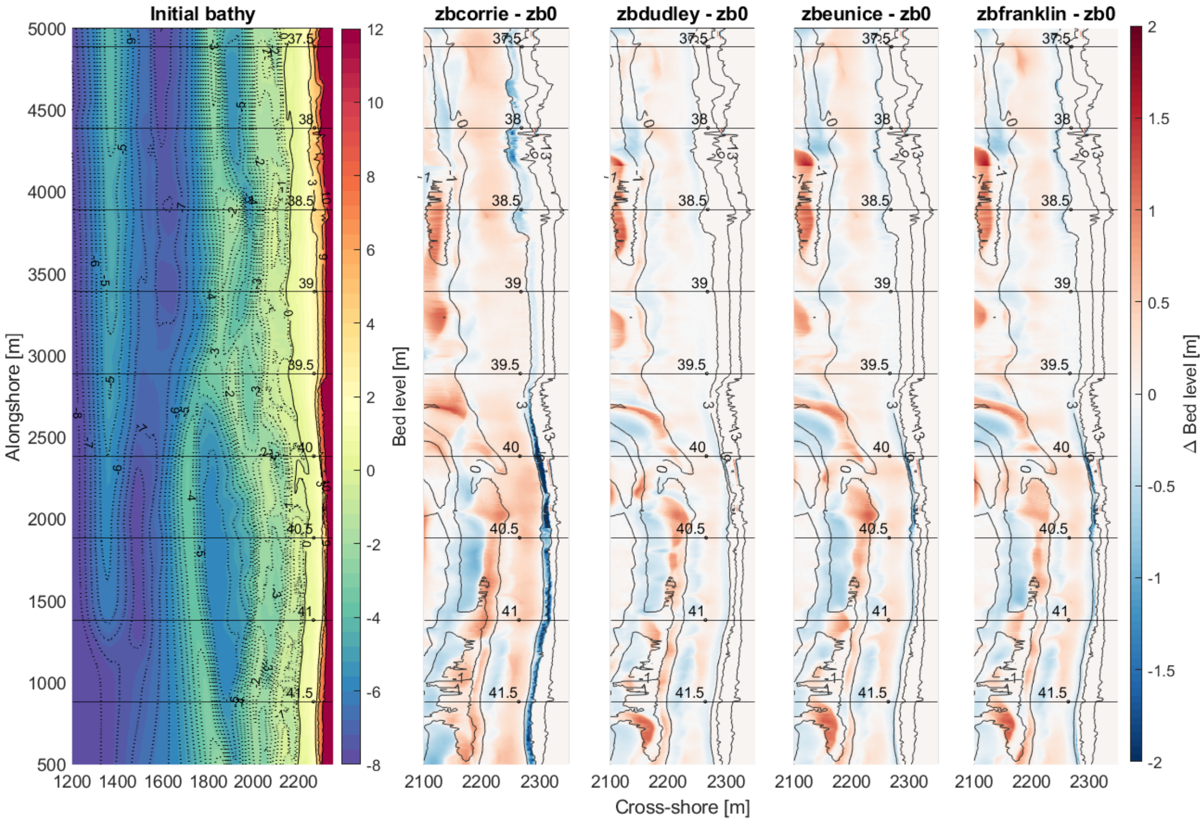

**Figure H.1:** March 2020

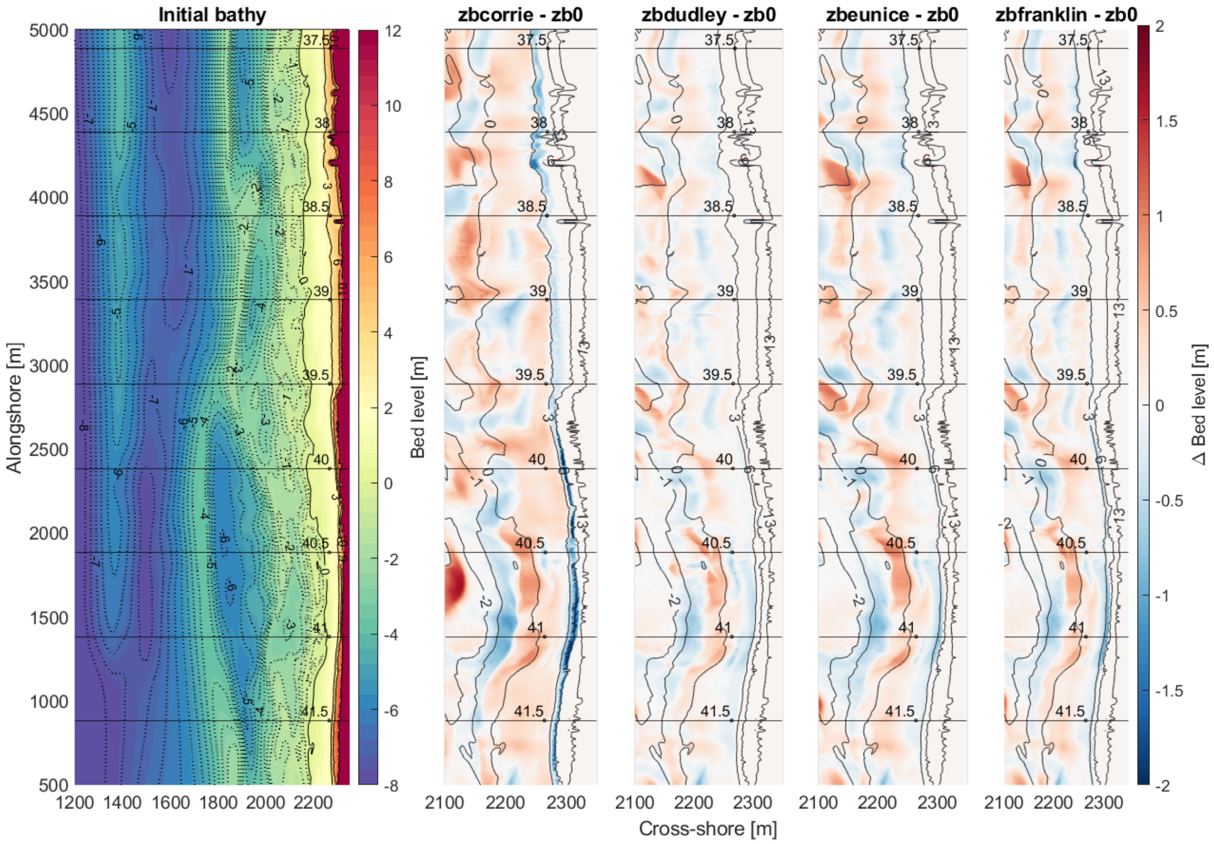

**Figure H.2:** October 2020

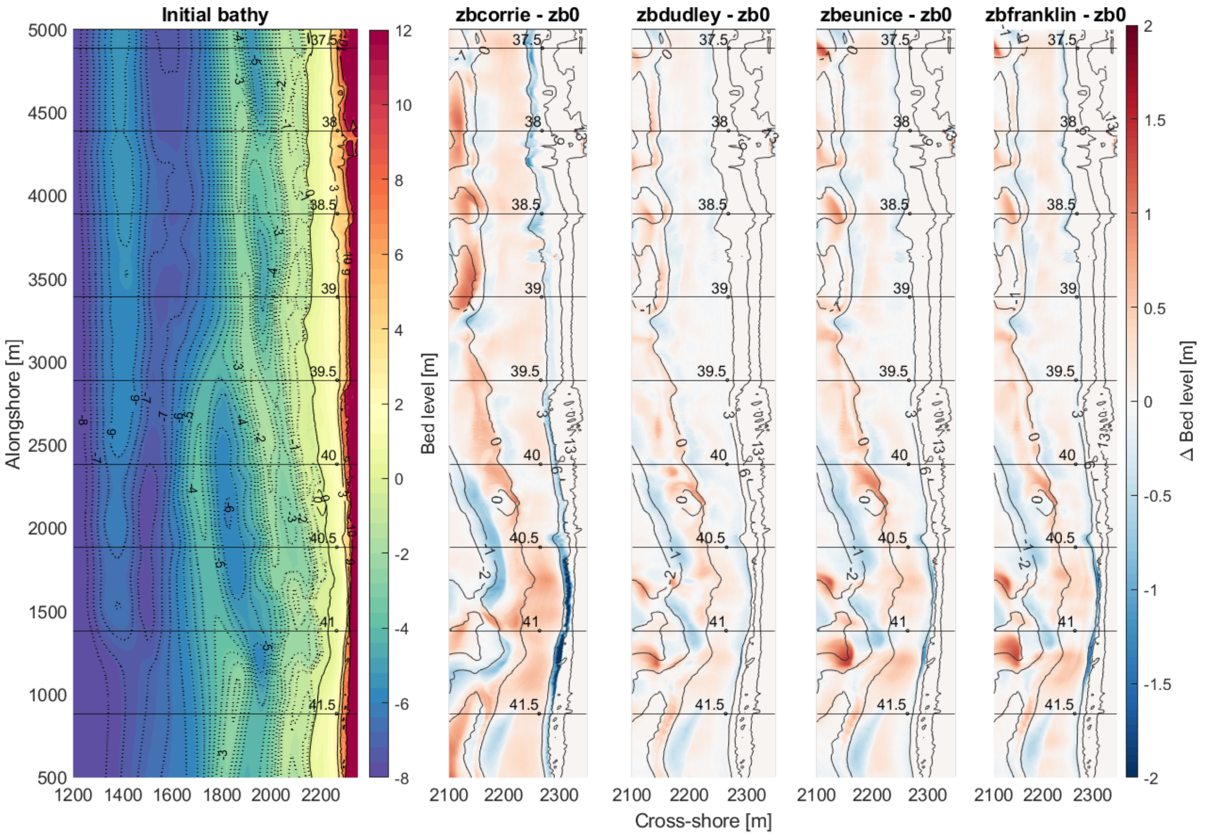

**Figure H.3:** March 2021

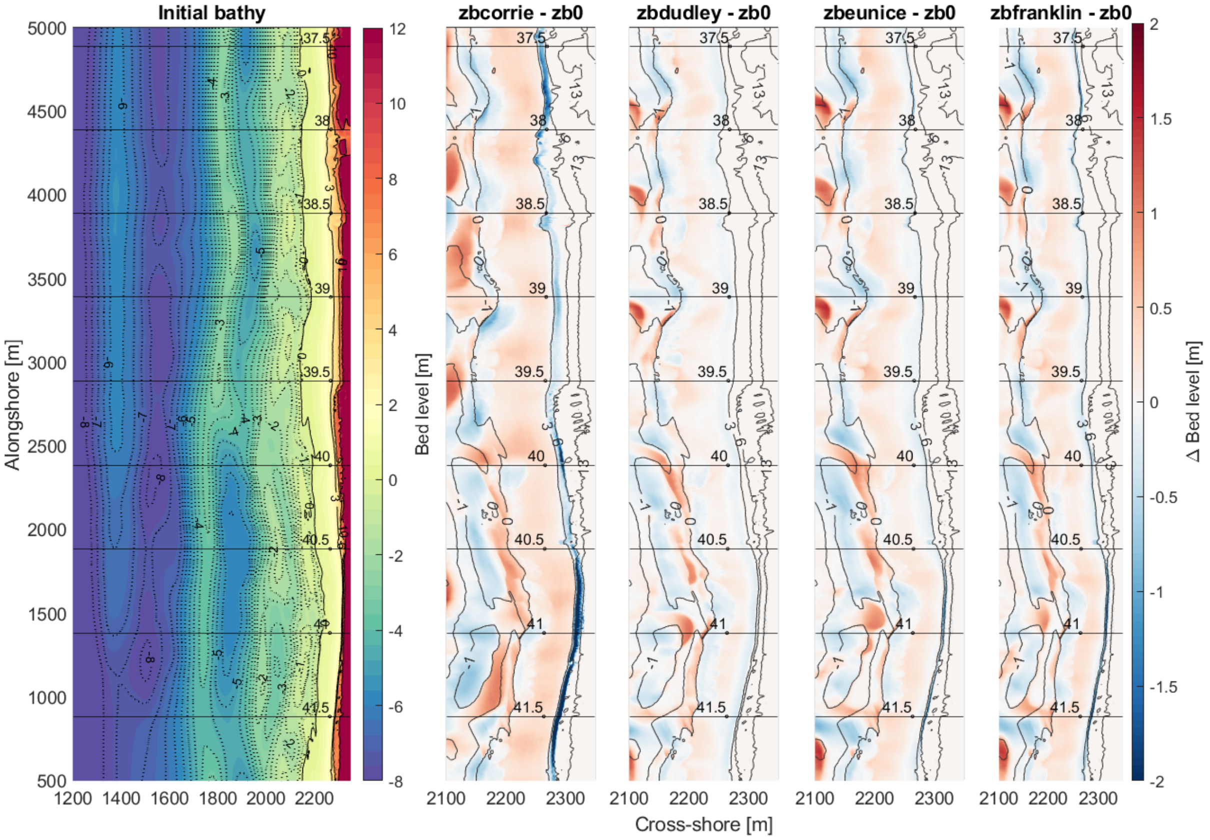

**Figure H.4:** March 2022

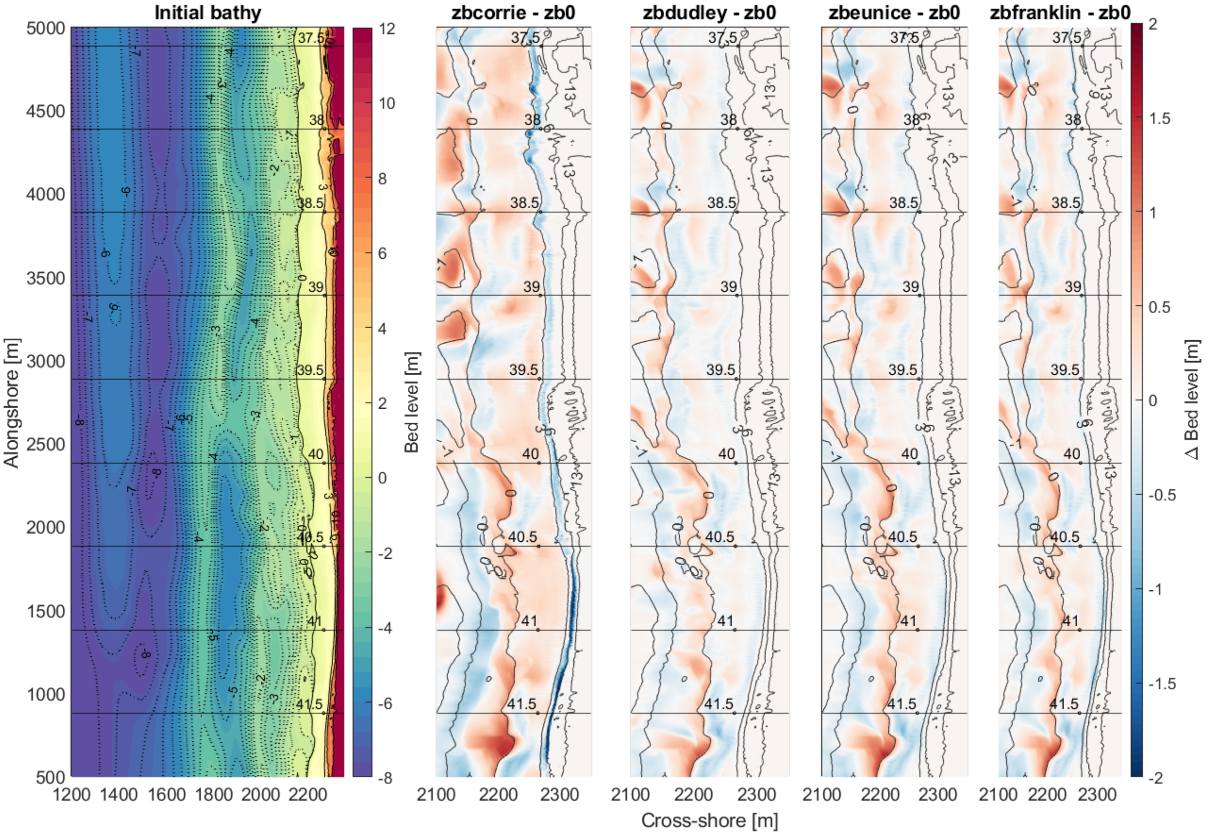

**Figure H.5:** October 2022

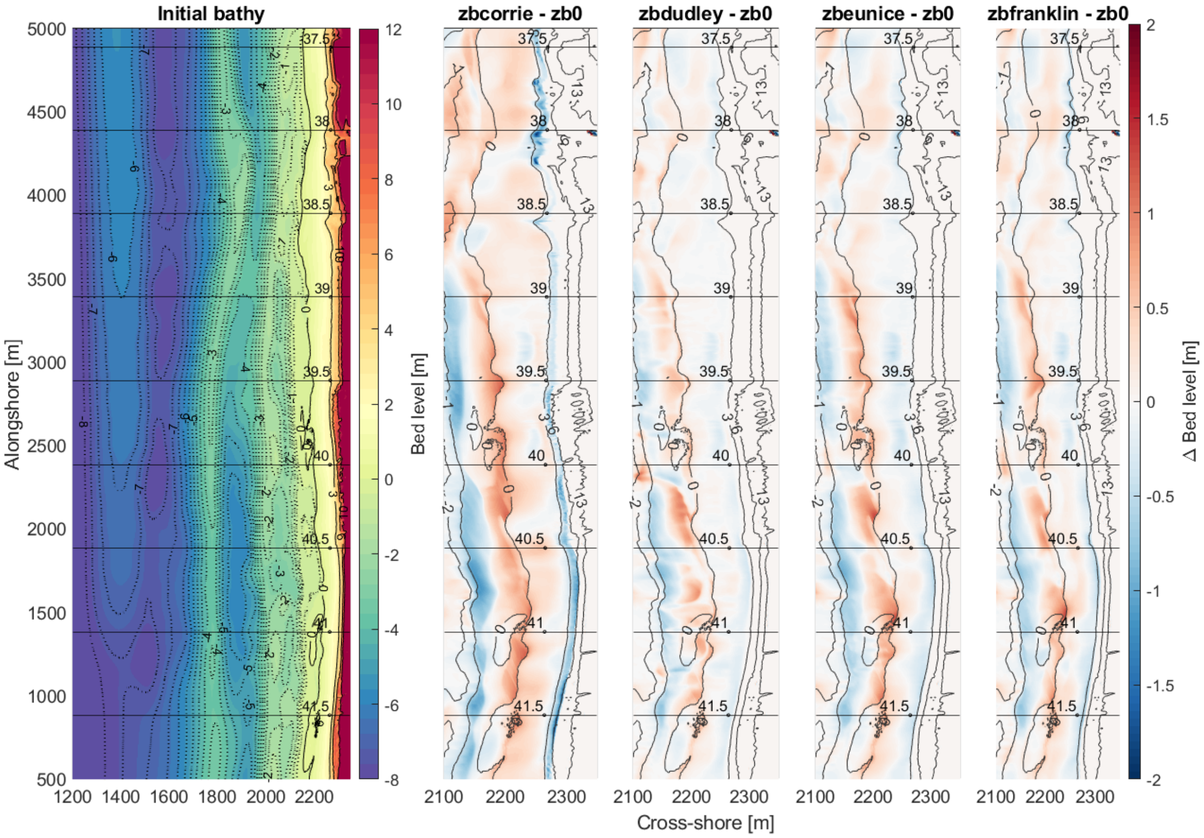

**Figure H.6:** October 2023